Université catholique de Louvain
Ecole Polytechnique de Louvain

Information and Communication Technologies,
Electronics and Applied Mathematics (ICTEAM)
division of Electrical Engineering
(EPL/ICTEAM/ELEN)

Body-Area-Network Antennas: Green's Functions, Numerical Analysis and Design

Farshad Keshmiri
Thesis presented for the Ph.D. degree
in Applied Science

Examining Committee:

Christophe CRAEYE	UCL - Supervisor
Claude OESTGES	UCL
Yang HAO	Queen Mary, University of London
Jon WALLACE	Jacobs University Bremen
Danielle VANHOENACKER-JANVIER	UCL - Chairman

Private defense: 21 December 2011
Final manuscript: February 2012, Louvain-la-Neuve, Belgium

To My Parents,
For their love, dream, and sacrifice throughout my life

Acknowledgements

It is a pleasure to thank the many people who made this thesis possible. First of all, I would like to express my deepest gratitude to my advisor, Christophe Craeye, for his support, patience, and encouragement from the very early stage of this research as well as giving me extraordinary supervision throughout the whole thesis.

I would like to thank my parents and my brothers for the support they provided me through my entire life. I must specially acknowledge my wife and best friend, Saloomeh Shariati, without whose love and positive encouragement I would not have achieved the work described in this thesis. I thank my little boy Soren who has let me work in all the joy of being a father. I should also thank my wife's parents and sisters who always give me positive spirit that make me feel loved and welcomed.

Special thanks to the members of my jury committee, Jon Wallace, Yang Hao, Claude Oestges, and Danielle Vanhoenacker-Janvier for the assistance they provided and their useful comments. Another persons to whom I owe my gratitude are my previous supervisors, Majid Tayarani and Abbas Pirhadi, who guided me through the basic knowledge in electromagnetics during my Master in Iran University of Science and Technology (IUST). I also acknowledge the ESoA (European School of Antennas) for the very high quality courses from which I learned a lot.

My time in Louvain-la-Neuve was made enjoyable mainly due to the many friends and groups that became a part of my life. Among all, I have to name some special ones to show my gratitude; Safa Jamali, Mamali Shirvani, Reza Shirazi, Adel Hatami, Shaghayegh Khani, Maryam Tahan, Masoud Jenabi, Katayoon Saeedi, Onur Oguz, Ilke Bayram, Remi Sarkis, Suzanne kieffer, Lyazid Aberbour, Hadi Goldansaz, Vaibhav Bhatnagar, Mostafa Emam, Dina

Kamel, David Gonzalez Ovejero, Adriana Gonzalez, and Mostafa Ahmadi. I should also thank my current and past lab mates for the stimulating discussions and the nice moments we spent together. Thank all of you for being there and making my PhD life in Belgium.

Abstract

With the rapid expansion of wireless technologies such as wireless on-body sensors, mobile devices, and wireless implants, there is a growing need to investigate the effect of human presence on the wireless communication channel. There have been numerous studies to model on-body propagation. However few of them describe on-body antennas analytically. Our main contribution is to use a simplified geometry model for the body to optimize the configuration of on-body links by means of analytical modeling.

In this thesis we use electromagnetics fundamentals to model the interaction between antennas located very close to the human body, represented as a simplified cylindrical model. For different antenna locations and polarizations, we try to obtain physical insights about the communications between on-body antennas, and to see how body tissues can alter the antenna characteristics. We provide most examples for 0.915 GHz and 2.45 GHz frequencies, since they represent unlicensed ISM (Industrial, Scientific and Medical) bands available internationally, and resulted in widespread narrowband standards, like Zigbee and Bluetooth.

We exploit experimental results obtained in an anechoic chamber and also results from commercially-available elecromagnetic simulators, like *CST Microwave Studio*®, EMPIRE, and NEC, to validate our model, derived directly from Maxwell's equations. As a first step, the propagation trends due to an infinitesimal current source (point source) with arbitrary polarization are studied inside, away, along and around a homogenous lossy cylinder. To do that, we use a Fourier Transform technique to find the Green's function in the presence of a cylinder. In fact, we integrate the fields radiated from the line sources over their wavenumbers to find the fields radiated from the point source. For point sources with tangential-to-cylinder polarization, cylindrical

wave decompositions can provide the harmonics of incident fields. In the case of a source with normal-to-cylinder polarization, the related boundary conditions cannot be satisfied in the same way and we derive the cylindrical wave decomposition of fields from a *modified addition theorem*.

In the second part, an in-house MoM (Method of Moment) code is developed to find the excited and coupled current distributions on two dipole antennas located very close to the cylinder. Their transmittance (S_{21}) for different relative positions around the cylinder shows a very good agreement with the results from experiments and simulations, including interference effects attributed to the cylinder-attached waves. Afterwards, a Parseval type transform is applied to cylindrical field harmonics to extract a compact expression for the power absorption, for normal, vertical, and horizontal polarizations of the source.

Finally, a compact antenna is designed; it can radiate a maximum of power along the body surface. It allows the excitation of surface waves that can carry energy on the surface of the body and maximize the coupling between antennas.

In our model we consider a homogenous lossy cylinder with permittivity of the high-water content human tissues, as an approximation of the body. Although the abdominal cross section of the body does not really have a circular shape, strong similarities have been observed between the simulation and experimental pathloss trends versus distance.

Contents

List of Figures

Notations and Acronyms

Mathematical notations

j	imaginary unit: $j = \sqrt{-1}$
x	a scalar
$\hat{x}$	a unit vector
$\mathrm{Re}(x)$	the real part of x
$\mathrm{Im}(x)$	the imaginary part of x
$\|x\|$	the absolute value of x
$\mathbf{x}$	a vector
x_m	the $(m+1)$th entry of vector $\mathbf{x}$: $\mathbf{x} = [x_0, x_1, \ldots, x_{K-1}]^T$
$\mathbf{x}^T$	the transpose of vector $\mathbf{x}$
x^*	the conjugate of x
$\mathbf{X}$	a matrix
$\cong$	is approximately equal to
$\propto$	is proportional to

Acronyms

ACK	ACKnowledgment
SNR	Signal to Noise Ration
FT	Fourier Transform
IFT	Inverse Fourier Transform
UTD	Uniform Theory of Diffraction
GTD	Geometrical Theory of Diffraction
VNA	Vector Network Analyzer
MoM	Method of Moment
BF	Basis Function
TF	Testing Function
BAN	Body Area Network
WBAN	Wireless Body Area Network
BSN	Body Sensor Network
FDTD	Finite Difference Time Domain
BALUN	BALance to UNbalance (transition)
FBW	Fractional BandWidth
MIMO	Multiple Input Multiple Output
TM	Transverse Magnetic
TE	Transverse Electric
PDA	Personal Digital Assistant
EM	Electromagnetic
PIFA	Planar Inverted F Antenna
IFA	Inverted F Antenna

Symbols

A	Magnetic vector potential
k	Wave number
k	Wave vector along $\bar{z}$
λ	Wavelength
ω	Angular frequency
μ	Material permeability
ϵ	Material permittivity
μ_0	Permeability in free space
ϵ_0	Permittivity in free space
J	Currant density
E	Electric field
H	Magnetic Field
$H_m^{(2)}$	Hankel function of the second kind with order of m
J_m	Bessel function with order of m
σ	Conductivity
λ	wavelength inside material
λ_0	Wavelength in free space
η	Wave impedance inside material
η_0	Wave impedance in free space
ν_r	Radiation efficiency of antenna
ν_t	Total efficiency of antenna
P^s	Time-average power across surface S
P^{ta}	Total available power of antenna
P^{rad}	Radiated power from antenna
δ	Dirac delta function
δ_k	Kronecker delta function

Introduction

1

Wireless body area networks (WBAN) and wireless body sensor networks (WBSN) are terms used to describe wearable communicating devices. The network enables wireless communication between several miniaturized body-sensor units and a single central unit worn on the human body. A wireless body area network is a collection of low-power, miniaturized, lightweight wireless sensors that monitor a patient's vital information such as heart rate and blood pressure. Through environmental sensors, it may also monitor external parameters such as ambient temperature [4, 5]. Each sensor measures parameters of interest and sends the data to a central device, such as a PDA, by means of dedicated wearable antennas. Examples include sensors to observe brain activity, for recording or warning against seizure events, or sensors to examine heart activity, for diagnosis and automatic emergency calls. The wide diversity and potential of these applications makes BAN an exciting research direction.

WBAN requires the development of suitable antennas that combine flexibility with robustness and reliability. The WBAN channel model can be classified as follows [6]:

- Communications from an antenna off the body to an antenna on the surface of the body: this modality will generally be termed *off-body*, where a wearable electronic device transmits the processed data from a variety of sensors to a base station. It is important to screen the antenna from the body and to prevent the body tissue from degrading the antenna efficiency. This can be achieved to a certain extent through the use of a small ground plane. The challenge for this antenna is to maintain good performance despite changes in the body posture.

- Communications within on-body networks and wearable systems, this modality will generally be termed *on-body*: The cables and connectors should be replaced by wireless networks. However, current body communication is limited because it has relatively low capacity. It is necessary to keep in mind that there are 3 primary criteria for designing the wireless modules for on-body communications: 1- High data rates expected in the future. 2-Being small and lightweight. Both of these suggest the use of high frequencies 3-Consuming a minimal power, which means highly efficient links.

- Communications with medical implants, *in-body*: There are lots of implants that can be used in the body, like cochlea implant, glaucoma sensors, retinal implant, sub-dermal sensors, and hierarchy of implants applied to head.

WBAN requires body-worn antennas, which should be modeled with respect to the mutual coupling with the human body. This coupling affects the return loss, radiation pattern, and efficiency of the BAN antennas. Here, we study different BAN modeling techniques and the model simplification methods as follows.

1.1 Electromagnetic modeling of BAN antennas

A computationally simple and generic body area propagation model is required to develop efficient low-power radio systems for use near the human body. The exact electromagnetic analysis of BAN models is possible either through measurement campaigns [6–13] or using numerical techniques. FDTD (Finite Difference Time Domain) is the dominant numerical method used to study the EM interactions with the human body. Both in-house FDTD modeling software [14, 15] and commercially available FDTD simulators [16–19] have been used to simulate different types of BAN antennas. Both measurements and FDTD simulations have successfully described very specific communication scenarios. Using measured or simulated results, complete statistical ultra-wideband and narrowband models have been developed in [20–22] and standardized by the IEEE [23]. However there are some limitations for these approaches. Numerically modeling the small wearable antennas in close vicinity of the sophisticated inhomogeneous human bodies is very time consuming [15]. Moreover, if the type or the location of the antennas change, a new set of numerical simulations is required. We should note however the much finer level of geometrical detail allowed by a FDTD approach. Measurements do not the physical propagation mechanism, forcing researchers to rely on some ad-hoc modeling approaches that are not always motivated by fundamental principles.

Reducing the complexity of this electromagnetic problem is possible by considering simple geometries such as cylinders [2,24–29] and spheres [30,31] to represent the body trunk (or the arms [28, 32]) and the head, respectively. Here, we consider a homogenous infinite lossy cylinder as an approximation of the body trunk.

When the cylinder is large enough (radius larger than about one wavelength) and the source is not too close to it, high-frequency asymptotic approximations are valid and the canonical problem of the field excitation on a circular cylinder can be solved with an asymptotic high-frequency method, such as the GTD [33] or its uniform versions, like the UTD [34–37]. UTD is an extension to ray tracing allowing the propagation channel to be described in terms of the sum of rays diffracting around and reflecting from body parts [18]. According to [38], the average waist circumferences of males and females aged more than 20 years are 101 cm and 94 cm, respectively. In the 2.45 GHz ISM band (wavelength (λ)=12.25 cm), these sizes are almost consistent with cylinders with radii of 1.3 λ and 1.2 λ, respectively. In [18], a combined Ray Tracing/UTD technique has been used to find the signal strength on the body surface. This method approximates the body with an elliptic cylinder and it provides relatively simple and reliable solutions for UWB on-body radio channels. The theory of diffraction describes the attenuation of the creeping waves along a path on a lossy dielectric surface and can be used to derive the BAN propagation model [18,39]. Nevertheless, UTD is still not really applicable for BAN at lower frequencies, e.g. 0.915 GHz, and also thinner cylinders, e.g. arms at 2.45 GHz. The desirable BAN antennas are body-worn and the very small distance between body and the low-profile antennas does not fully allow UTD approximations.

Efforts have been carried out to model on-body propagation locally through a planar model of the human body. Non-line-of-sight propagation around the body can be approximated by considering the bound waves along the planar surface, although these models follow different propagation mechanisms. In [40], Lea et al. show that a planar layered model of the human body is capable of supporting TM Zenneck waves below 3 GHz. They also present a complete comparison between the Norton waves and the available published experiments along and around the body. The measurement results in [41] show that the TM waves can be excited by a large variety of antennas, e.g. monopoles, parallel dipoles, patches, IFA (Inverted F Antenna) and PIFA (Planar Inverted F Antenna), with almost the same attenuation factor. We certainly expect the normal-to-body polarized antennas to excite the TM waves more efficiently than the tangential (horizontal and vertical) ones. In [42], Conway et al. use the homogeneous planar model to approximate the path gain around the lossy cylinders. As the frequency increases, the penetration depth inside all body tissues decreases [43] such that higher-frequency waves are significantly more attenuated and the EM waves are mostly confined to the surface rather than penetrating into body. Thereby, the homogenous approximation of the body is practically less applicable and we have to use a multi-layer tissue models. In [40] a two-layer model at the 2.4 GHz ISM band provides a good approximation for the behavior of the four-layered model.

In order to better account for curvature, Eid and Wallace in [44, 45] used a Method of Moment based on surface equivalence, such that the body can be modeled with a cylinder with arbitrary cross section. The sensitivity of the electric fields around the body to the shape of the body is also successfully studied, through a comparison between the experiments and simulations for circular, elliptical and superquadratic cross-sections.

1.2 Model Simplifications

A point source is a reasonable approximation for radiation by an antenna[1] if the antenna size is very small compared to the wavelength. This is normally the case for compact body-worn devices. In Chapter 2 we use the point source approximation of a BAN antenna to model the pathloss trends around and along the cylinder. However, this approximation is not appropriate for analyzing near-field propagation trends of realistic antennas. Nevertheless, it can be used in the form of a Green's function for the electric fields implicitly accounting for the presence of a cylinder (hereafter named "cylinder Green's function") to form the basis of an accurate model employing the Method of Moments (MoM). Exploiting this Green's function, a MoM code has been developed (Chapter 3) to calculate the excited and coupled currents of two on-body dipoles.

The second approximation, as already mentioned in Section 1.1, is using a lossy cylinder as a reasonable first-order approximation of a human body. It allows us to include the main propagation phenomena, like diffraction around a curved lossy surface and penetration into the body. Such a model also allows us to evaluate the possibility of exciting the radiating waves around the body and afterwards calculate the phase and group velocities associated to those radiating waves. The result strongly depend on the frequency and polarization of the source, on the radius of curvature, and on tissue properties.

Since the cylinder is assumed infinite along $\hat{z}$ and also is periodic in the $\hat{\phi}$ direction (Fig. 1.1), we can describe the electric field and also the current source to spectral domain while using a two-dimensional Fourier Transform (1.1). In fact, the Green's function is a 2D harmonic superposition in space, with known harmonic variation in $\hat{z}$ and $\hat{\phi}$ directions and unknown variation in $\hat{\rho}$ direction. We have to solve this 2D problem for a wide range of spectral indices m and k_z, where m is the number of cylindrical harmonics and k_z is the wave number along $\hat{z}$. In order to find the 3D solution, we must combine the solution by a summation over the complete m and k_z spectrum:

[1]However, complex impedance can not be defined for a point source.

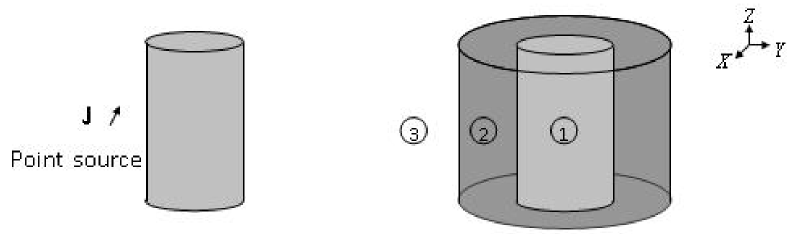

Figure 1.1 (a) The space domain and (b) the spectral domain Green's function of an infinite lossy cylinder.

$$\left\{ \begin{array}{l} \tilde{\mathbf{E}}(\rho, m, k_z) \\ \tilde{\mathbf{J}}(\rho, m, k_z) \end{array} \right. = \int_{-\infty}^{\infty} \int_{0}^{2\pi} \left\{ \begin{array}{l} \mathbf{E}(\rho, \phi, z) \\ \mathbf{J}(\rho, \phi, z) \end{array} \right. e^{jm\phi} e^{jk_z z} \, \mathrm{d}\phi \mathrm{d}z \tag{1.1}$$

$$\left\{ \begin{array}{l} \mathbf{E}(\rho, \phi, z) \\ \mathbf{J}(\rho, \phi, z) \end{array} \right. = \int_{-\infty}^{\infty} \int_{0}^{2\pi} \left\{ \begin{array}{l} \tilde{\mathbf{E}}(\rho, m, k_z) \\ \tilde{\mathbf{J}}(\rho, m, k_z) \end{array} \right. e^{-jm\phi} e^{-jk_z z} \, \mathrm{d}\phi \mathrm{d}z \tag{1.2}$$

1.3 Outline and Contributions

A fixed body without any movement is considered for the modeling in this thesis. The statistical influence of the body movements that is linked to the variations of the arm/leg/head positions, as studied in [28], and antenna displacements are out of the scope of this thesis. The EM waves in high frequencies, e.g. at 2.45 GHz, are mostly confined to the human surface rather than penetrating through the body, because of low penetration depth of body tissues, especially those with a high-water content. We set the material properties of the homogenous lossy cylinder (body) everywhere according to the high-water content of human tissues.

This thesis is structured as follows:

1.3.1 Chapter 2: Body Area Propagation Model for Tangential-to-Body Antennas

Chapter 2 provides a simple and generic body area propagation model derived directly from Maxwell's equations and revealing basic propagation trends away, inside, around, and along the body. We used a point source approximation for BAN antennas and also used a cylindrical approximation for the human body. We use a FT technique to find the Green's function due to a tangentially-polarized point source (both vertical and horizontal polarizations) near the cylinder, from the solution of a line source with an arbitrary wave-number.

We have verified the proposed analytical model by comparing it with measurements in an anechoic chamber. This chapter develops an analytical model of the body, describes the expected body area pathloss trends predicted by Maxwell's equations, and compares it with measurements of the electric field close to the body.

1.3.2 Chapter 3: Body Area Propagation Model for Normal-to-Body Antennas

For on-body applications, the radiation pattern or space diversity often can affect the received signal power more strongly than the polarization diversity [46]. However for a non line-of-sight link, e.g. between two antennas placed in the front and in the back of a body trunk, the polarization of the source can significantly impact the link quality. The normal-to-cylinder polarization is the most effective one in producing fields in the shadow region of the cylinder [44,45,47,48]. On the other hand, the body has a small effect on the current of a radially-oriented dipole antenna, when its distance from the body is bigger than a certain small value (Section 3.3.2). So, we focus on the transmittance between dipole antennas with normal-to-cylinder polarizations.

In Chapter 3, a modified addition theorem (Appendix A) is proposed to derive the cylindrical wave decomposition of fields due to a normal-to-cylinder point source. The Green's function is calculated for the same cylinder as considered in Chapter 2. The fields scattered from a lossy cylinder, as an approximation of the human body, are also calculated and tabulated for use in an integral-equation study of dipoles. Using the MoM in the 2.45 GHz *ISM* band, a pair of dipoles at a small distance from the cylinder are considered to model the transmittance between canonical standard on-body antennas that carry normal-to-cylinder currents.

An anechoic chamber measurement is performed and the measured transmittance between two dipoles on the human body has been compared with the simulated one on the lossy cylinder. Although the abdominal cross section of the body does not have exactly a circular shape, strong similarities have been observed in the pathloss trends around body and cylinder. A very good agreement has been obtained between the transmittances of dipoles, located normal-to-cylinder provided by the analytical/MoM model, *CST Microwave Studio*® simulations, and on-body experiments, including interference effects attributed to the body-attached radiating waves.

1.3.3 Chapter 4: Analysis of Power Absorption in Cylindrical Bodies

In Chapters 2 and 3, the cylindrical wave decomposition has been exploited to derive the field harmonics outside an infinite lossy cylinder, exposed to the near field of an arbitrarily-polarized point source. In Chapter 4, a Parseval type transform is applied to cylindrical field harmonics to find the power crossing the surface of the cylinder. A simple formula based on the field spectra inside the lossy medium is extracted.

As an example of our general cylindrical model, we set the permittivity of the lossy cylinder to the average complex permittivity of the human body tissues at f=2.45 GHz. The model is validated through comparisons with results from the *CST Microwave Studio*® commercial software, where the absorbed power is calculated from the efficiency of a short-dipole antenna combined to a finite lossy cylinder. A discussion about the dependence of maximum power absorption on the source polarizations and the source locations is provided, considering the surface waves along and around the body.

1.3.4 Chapter 5: Design of Antennas Devoted to Body Area Networks

A compact low-profile antenna radiating maximum power tangential to the body surface is required to maximize the transmittance between body-worn antennas, while launching and receiving the surface waves can help by increasing the radiated fields on the surface of the body. Because of short-circuiting of the tangential fields by the lossy tissues, the chance of exciting those surface waves with the current distributions normal to the body is higher than the current distributions tangential to the body. Consequently, the best candidate for BAN antennas would be the one that can produce the radially-polarized electric fields on the surface of body.

In Chapter 5, we describe the design of a relatively low-profile folded monopole antenna with a height of $\lambda/10$ and an area equal to the surface of a 50-Euro-cent coin. Some other antennas, developed to perform the measurement, are also described in this chapter.

Body Area Propagation Model for Tangential-to-Body Antennas

2

2.1 Introduction

To help understand propagation near the body, we have implemented a computationally simple model of body area propagation derived directly from Maxwell's equations. This model has been obtained through a cooperation with Gemma Roqueta and Andrew Fort [2, 49, 50]. In this chapter, except Section 2.6, we assume the antenna can be modeled as a infinitesimal current source (point source), and the body can be modeled as a lossy cylinder; then we evaluate the resulting electromagnetic fields. This approach is related to models developed for antennas printed on coated cylinders [51–54]. Unlike UTD (Uniform Theory of Diffraction)[1], this exact computation is valid regardless of the distance between the antenna and the body and can be used for tangentially polarized antennas. The physical meaning of the main steps of this derivation is provided. We begin with the solution for an infinite line source in the vicinity of an infinite lossy cylinder. We decompose the source into the cylindrical current sheets to give the incident field harmonics. We then numerically calculate the IFT of the line source to obtain the fields due to a point source, representing the antenna, near a lossy cylinder, representing the body. Using this model, we have evaluated the electric fields for propa-

[1] The UTD is an extension of GTD (Geometrical Theory of Diffraction). The UTD approximates near field electromagnetic fields using the ray diffraction.

gation around, along, away, and inside a lossy cylinder to estimate the major propagation trends near a human body, and we have proposed simple pathloss laws which can be used in practice. Finally, we have validated this approach by comparing the fields predicted by this simple model with actual measurements around the human body in an anechoic chamber. The resulting approach can therefore be used to rapidly approximate average pathloss near a body, or to physically justify the average pathloss trends of more realistic statistical models extracted from measurements and FDTD simulations.

Measurement results or FDTD simulation results allow us to accurately model the on-body propagation with a fine level of geometrical details, which is needed in most on-body applications. However, for some scenarios, such as non-line-of-sight links between two antennas placed in front and in the back of the body, or line-of-sight links between two antennas along the body trunk (in front or in back), the proposed analytical approach can be used to approximate the pathloss. In the other hand the resulting approach also helps us to generally investigate the propagation of fields along a curved surface, originating from an antenna located close to the surface.

For the on-body applications, radiation pattern or space diversity can affect the received signal power more strongly than the polarization diversity [46]. However for a non line-of-sight link, e.g. between two antennas placed in front and in the back of a body trunk, the polarization of the source can significantly impact the link quality. The normal-to-cylinder polarization is the most effective polarization in producing fields in the shadow region of the cylinder [44, 45, 47, 48]. On the other hand, the body has a small effect on the current of a radially-oriented dipole antenna, when its distance from the body is bigger than a certain small value (see Section 3.3.2). So, we target the transmittance between dipole antennas with normal-to-cylinder polarizations.

This chapter is organized as follows. Section 2.2 begins by outlining the various steps in our analytical developments. Section 2.3 reviews the well-known solution for a tangentially polarized line-source near a lossy conductor. To obtain a more realistic model of a small antenna close to the body, Section 2.4 proposes a numerical integration technique to transform the line source into a point source and addresses other practical issues required for computer implementation. Section 2.5 demonstrates from fundamental prin-

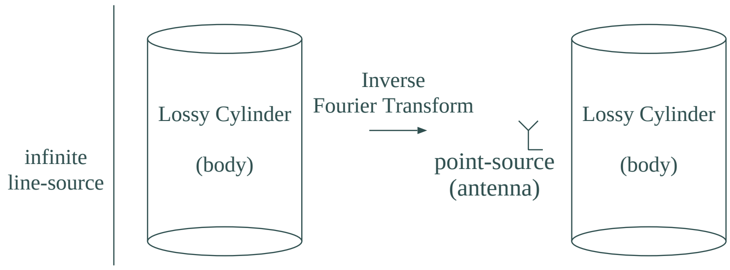

Figure 2.1 Proposed two-step procedure for body area modeling. First we obtain the solution for a line-source near a lossy cylinder. Second, we transform the solution to a point source by taking its inverse FT.

ciples the major pathloss trends expected for propagation near a curved lossy body and identifies some simplified pathloss laws which are more convenient in practice. In Section 2.6, we develop a MoM code in order to find the current distribution and also the total radiated electric fields due to a half-wavelength dipole antenna, oriented parallel to a lossy cylinder. Section 2.7 then compares the total model with measurements taken near a body in an anechoic chamber. Finally, Section 2.8 summarizes the major conclusions of this study.

2.2 Generic approach to body area modeling

Fig. 2.1 summarizes our proposed approach to body area modeling, in this chapter. We model the antennas as a point source with some polarity, and the human body as an infinite lossy cylinder with arbitrary material parameters.

In order to derive the electric fields around and inside a lossy cylinder resulting from a point source, we follow a two-step procedure as indicated in Fig. 2.1. First, we solve the problem of a linear current source located outside a lossy cylinder. The solution to this problem can be obtained by representing the displaced cylindrical waves of the line source by a superposition of undisplaced cylindrical waves originating from the cylinder axis. This allows us to easily enforce the boundary conditions around the surface of the lossy cylinder. Section 2.3 describes the details of this step. Second, we convert the line source to a point source by performing an inverse FT of the current source along the vertical spectral coordinate (k_z). The transform must be obtained numerically using a contour integral to avoid a singularity in the line source

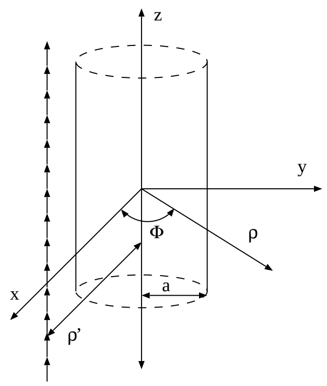

Figure 2.2 Geometry and coordinate system for our analysis

solution. Section 2.4 describes the details of this step. Throughout this chapter, we focus on the special case of a tangentially polarized point-source which is representative of low-profile antennas. Low profile antennas are more desirable for comfortable, low-cost body-worn devices. However, in the next chapter the general approach is used to investigate antennas polarized normal to the body having more desirable pathloss characteristics.

2.3 Line source

Fig. 2.2 provides a more precise diagram of the geometry emphasizing the major variables used throughout our analysis. An infinite cylinder of radius a is oriented along the z-axis at the origin of the coordinate system. An infinite linear current source is located at cylindrical coordinates (ρ_s, ϕ_s). We let the current on this line vary along the z-axis as $e^{-jk_z z}$. The exponent indicates the current source is a traveling wave in the $\hat{z}$-direction with a propagation constant k_z. This choice of current will allow us to convert it to a point source by means of an IFT in Section 2.4.

We begin the body area modeling developments by writing down the well-known Vector Helmholtz Equations which are most convenient for solving this problem:

$$\begin{aligned}(\nabla^2 + k^2)\mathbf{E} &= j\omega\mu\mathbf{J} \\ (\nabla^2 + k^2)\mathbf{H} &= -\nabla \times \mathbf{J}\end{aligned} \tag{2.1}$$

Where $k = \omega\sqrt{\mu\epsilon}$ is the wavenumber, ω is the angular frequency, μ is the material permeability, ϵ is material permittivity, and $\mathbf{J}$ is the current density.

We want to determine the electric field $\mathbf{E}$ and magnetic field $\mathbf{H}$ that satisfy (2.1) for the geometry shown in Fig. 2.2. We know that the general solution to this equation can be written as the sum of the solution to the homogeneous equation $(\nabla^2 + k^2)\mathbf{E} = 0$ or $(\nabla^2 + k^2)\mathbf{H} = 0$, and any particular solution to (2.1). In Section 2.3.1, the solution to the homogeneous equation will be explained as a scattered field by the lossy cylinder. This solution correspond physically to the general representation of the fields, that exist inside or outside the cylinder, in the absence of the sources. The particular solution will correspond to the incident field from the line source propagating through free space without the presence of the lossy cylinder and will be discussed in Section 2.3.2. The unknown coefficients in the homogeneous solution will be found by incorporating the boundary conditions, which then allows us to find the unknown coefficients. Section 2.3.3 describes the total solution obtained by summing the scattered and incident fields and enforcing the boundary conditions along the surface of the cylinder.

2.3.1 Scattered field

The z-component of the homogeneous solution to the Helmholtz equations for the electric and magnetic fields is obtained by separation of variables [51]:

$$E_z^s(\rho,\phi,z) = \sum_{m=-\infty}^{+\infty} e^{jm\phi} e^{-jk_z z} \begin{cases} A_m J_m(k'_\rho \rho) & \rho \leq a \\ A'_m H_m^{(2)}(k_\rho \rho) & \rho \geq a \end{cases} \tag{2.2}$$

We also have:

$$k_\rho = \sqrt{k^2 - k_z^2}, \quad k'_\rho = \sqrt{k'^2 - k_z^2} \tag{2.3}$$

as the radial wave vectors outside and inside the cylinder, respectively with $k' = k\sqrt{\epsilon_r \mu_r}$.

Following the same reasoning, a similar expression can be derived for the magnetic field:

$$H_z^s(\rho,\phi,z) = \sum_{m=-\infty}^{+\infty} e^{jm\phi} e^{-jk_z z} \begin{cases} B_m J_m(k'_\rho \rho) & \rho \leq a \\ B'_m H_m^{(2)}(k_\rho \rho) & \rho \geq a \end{cases} \tag{2.4}$$

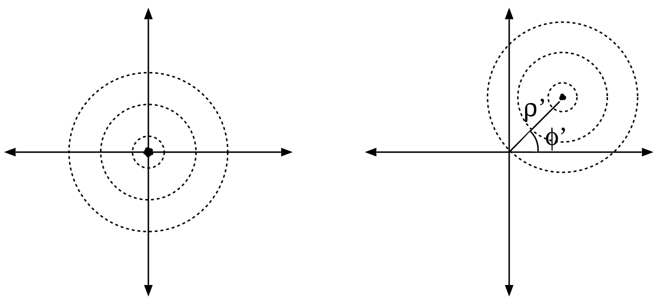

Figure 2.3 The left side shows the wavefronts of an undisplaced cylindrical wave, while the right side shows the wavefronts of a displaced cylindrical wave that would be generated by a line source located at coordinates (ρ_s, ϕ_s)

$H_m^{(2)}$ and J_m represent the Hankel function of the second kind with order m and the Bessel function of the first kind with order m respectively. The constants A_m, A'_m , B_m, and B'_m will be determined in Section 2.3.3 from the boundary conditions imposed by the geometry. We will show later how the other components of the field can be obtained from the vertical components.

2.3.2 Incident field

The incident field can be determined by noting that the field everywhere, except on the current source itself, must take the form of the homogeneous solution in (2.2) since there are no current or charge sources in free-space. Thus, the $\hat{z}$ component of the incident field will take the form:

$$E_z^i(\rho,\phi,z) = \sum_{m=-\infty}^{+\infty} e^{jm\phi} e^{-jk_z z} \begin{cases} C_m J_m(k_\rho \rho) & \rho \leq \rho_s \\ C'_m H_m^{(2)}(k_\rho \rho) & \rho \geq \rho_s \end{cases} \tag{2.5}$$

or

$$H_z^i(\rho,\phi,z) = \sum_{m=-\infty}^{+\infty} e^{jm\phi} e^{-jk_z z} \begin{cases} D_m J_m(k_\rho \rho) & \rho \leq \rho_s \\ D'_m H_m^{(2)}(k_\rho \rho) & \rho \geq \rho_s \end{cases} \tag{2.6}$$

Physically, we expect the fields generated by the line-source to consist of displaced outgoing cylindrical waves originating from the line source at $\rho = \rho_s$ (see Fig. 2.3). This expression indicates we can also express those fields by a sum of un-displaced cylindrical harmonics originating from the cylinder axis. The reason why we want to express the incident field solution as a sum of waves originating from the cylinder axis is that they have the same geometry as the lossy cylinder. This will make it easier to apply the boundary conditions of the complete solution at the surface of the cylinder in the following section.

We now need to determine the constants C_m and C'_m by applying the boundary conditions at the current source. The current source for the geometry shown in Fig. 2.2 can be expressed mathematically as:

$$\mathbf{J^v} = \sum_{n=-\infty}^{+\infty} \frac{I_v e^{-jk_z z}}{\rho_s} \delta(\rho - \rho_s)\delta(\phi - n2\pi)\hat{z} \tag{2.7}$$

Note that, without loss of generality, we have assumed that the source is located at $\phi_s = 0$ and $z' = 0$, which will simplify our notation. We have also written this expression such that it is valid for $\phi \in (-\infty, +\infty)$. This requires the term $2n\pi$ (for all integers n) since our cylindrical geometry is periodic with ϕ every 2π radians. The vector $\hat{z}$ indicates a vertical polarization. For the horizontal polarization case, we will simply replace $\hat{z}$ with $\hat{\phi}$ and denote the current density and its amplitude as $\mathbf{J^h}$ and I_h respectively.

The current source representation in (2.7) will make it difficult to apply the boundary conditions since it has the form $e^{-jk_z z}$ while the incident field in (2.10) is expressed in terms of the sum of cylindrical harmonics of the form $e^{jm\phi}e^{-jk_z z}$. We will therefore transform our line source into a similar sum of cylindrical harmonics by applying the following FT pair:

$$\sum_{n=-\infty}^{+\infty} \delta(\phi - n2\pi) \leftrightarrow \sum_{m=-\infty}^{+\infty} \delta(F - m) \tag{2.8}$$

resulting in the following expression:

$$\mathbf{J} = \frac{I}{2\pi\rho_s}\delta(\rho - \rho_s) \sum_{m=-\infty}^{+\infty} e^{jm\phi}e^{-jk_z z}\hat{z} \tag{2.9}$$

which now has the same mathematical form as (2.5). The source is now defined for all ϕ and is periodic every $\phi = 2n\pi$, indicating a cylindrical current sheet. Thus, by using the FT relation of (2.8), we have represented the original line source as a sum of cylindrical current sheets centered at the origin. This will allow us to easily apply the boundary conditions on the surface of the current sheet.

Since all expressions are now written using cylindrical harmonics having the form $e^{jm\phi}e^{-jk_z z}$ we will simply assume this term from now on without explicitly writing it every time. Furthermore, we introduce the following notation to represent a particular harmonic of propagation:

$$E^i_{m,z}(\rho,\phi,z) = \begin{cases} B_m J_m(k_\rho \rho) & \rho \leq \rho_s \\ B'_m H^{(2)}_m(k_\rho \rho) & \rho \geq \rho_s \end{cases} \tag{2.10}$$

In this notation, $E^i_{m,z}$ represents the m^{th} harmonic of the incident field from (2.5). While we have not explicitly written the factor $e^{jm\phi}e^{-jk_z z}$, it is still there and we must remember to multiply the signal by jm or $-jk_z$ whenever we take its derivative with respect to ϕ or z.

We know that the Hankel function $H^{(2)}_m(k_\rho \rho)$ from (2.10) approaches infinity as $k_\rho \rho \to 0$. Since we cannot have infinite fields in practice, the portion of our geometry which includes the origin can only consist of Bessel functions. Similarly, the fields in the region outside our cylindrical sheet can be presented by Hankel functions. This allows us to re-write the incident field inside and outside the cylindrical current sheet as

$$E^i_{m,z} = \begin{cases} C_m J_m(k_\rho \rho) & \rho \leq \rho_s \\ C'_m H^{(2)}_m(k_\rho \rho) & \rho \geq \rho_s \end{cases} \tag{2.11}$$

The expressions for the magnetic field have the same form, so we can also write the $\hat{z}$-component of the magnetic field

$$H^i_{m,z} = \begin{cases} D_m J_m(k_\rho \rho) & \rho \leq \rho_s \\ D'_m H^{(2)}_m(k_\rho \rho) & \rho \geq \rho_s \end{cases} \tag{2.12}$$

We can determine the other components of the electromagnetic field from the vertical components using the following relations which are valid for line sources with $e^{-jk_z z}$ variation. [51]:

$$\begin{aligned} \mathbf{E_s} &= \frac{1}{k_\rho^2}\left(-jk_z \nabla_s E_z + j\omega\mu \hat{z} \times \nabla_s H_z\right) \\ \mathbf{H_s} &= \frac{1}{k_\rho^2}\left(-jk_z \nabla_s H_z - j\omega\epsilon \hat{z} \times \nabla_s E_z\right) \end{aligned} \tag{2.13}$$

with

$$\begin{aligned} \nabla_s &= \hat{\rho}\frac{\partial}{\partial\rho} + \hat{\phi}\frac{jm}{\rho} \\ \hat{z}\times\nabla_s &= \hat{\phi}\frac{\partial}{\partial\rho} - \hat{\rho}\frac{jm}{\rho} \end{aligned} \tag{2.14}$$

The vectors $\mathbf{E_s}$ and $\mathbf{H_s}$ represent the $\hat{\phi}$ and $\hat{\rho}$ components of the electromagnetic field, while the scalars E_z and H_z represent the $\hat{z}$ components. Applying this relation to (2.11) and (2.12) allows us to express the $\hat{\phi}$ components as follows:

$$E^i_{m,\phi} = \begin{cases} \frac{1}{k_\rho^2}\big(C_m \frac{mk_z}{\rho} J_m(k_\rho\rho) + \\ \quad j\omega\mu k_\rho D_m J'_m(k_\rho\rho)\big) \quad \rho \le \rho_s \\ \\ \frac{1}{k_\rho^2}\big(C'_m \frac{mk_z}{\rho} H^{(2)}_m(k_\rho\rho) + \\ \quad j\omega\mu k_\rho D'_m H^{(2)'}_m(k_\rho\rho)\big) \quad \rho \ge \rho_s \end{cases} \tag{2.15}$$

and

$$H^i_{m,\phi} = \begin{cases} \frac{1}{k_\rho^2}\big(D_m \frac{mk_z}{\rho} J_m(k_\rho\rho) - \\ \quad j\omega\epsilon_0 k_\rho C_m J'_m(k_\rho\rho)\big) \quad \rho \le \rho_s \\ \\ \frac{1}{k_\rho^2}\big(D'_m \frac{mk_z}{\rho} H^{(2)}_m(k_\rho\rho) - \\ \quad j\omega\epsilon_0 k_\rho C'_m H^{(2)'}_m(k_\rho\rho)\big) \quad \rho \ge \rho_s \end{cases} \tag{2.16}$$

Equations (2.11) - (2.12) must satisfy the following tangential boundary conditions at the surface of the current sheets ($\rho = \rho_s$):

$$E_{z1} = E_{z2} \tag{2.17}$$

$$E_{\phi1} = E_{\phi2} \tag{2.18}$$

$$\hat{\rho}\times(\mathbf{H_2} - \mathbf{H_1}) = \mathbf{J} \tag{2.19}$$

The subscripts 1 and 2 indicate fields just inside and outside the current sheet respectively. The resulting solutions for a vertically and horizontally polarized current source are discussed below. By adding together weighted combinations of these components, we can generate the solution for a point source having arbitrary tangential polarity.

2.3.2.1 Vertical polarization

For the vertical polarity, the current source is polarized in the $\hat{z}$ direction, as indicated in (2.9), resulting in the following solution:

$$\begin{aligned} C_m &= -I_v \frac{k_\rho^2}{4\omega\epsilon} H_m^{(2)}(k_\rho \rho_s) && (2.20) \\ C'_m &= -I_v \frac{k_\rho^2}{4\omega\epsilon} J_m(k_\rho \rho_s) && (2.21) \\ D_m &= 0 && (2.22) \\ D'_m &= 0 && (2.23) \end{aligned}$$

2.3.2.2 Horizontal polarization

The developments for the horizontally polarized current source proceed in the same manner as the vertically polarized current source except now the current sheets have a $\hat{\phi}$ polarization instead of the $\hat{z}$ polarization. This results in the following solution:

$$\begin{aligned} C_m &= -I_h \frac{mk_z}{4\omega\epsilon\rho_s} H_m^{(2)}(k_\rho \rho_s) && (2.24) \\ C'_m &= -I_h \frac{mk_z}{4\omega\epsilon\rho_s} J_m(k_\rho \rho_s) && (2.25) \\ D_m &= -I_h k_\rho \frac{1}{4j} H_m^{(2)\prime}(k_\rho \rho_s) && (2.26) \\ D'_m &= -I_h k_\rho \frac{1}{4j} J'_m(k_\rho \rho_s) && (2.27) \end{aligned}$$

For both the horizontal and vertical polarization cases, we have made use of the following well-known identity to write the result in this simple form [51]:

$$J'_m(x) H_m^{(2)}(x) - J_m(x) H_m^{(2)\prime}(x) = \frac{2j}{\pi x} \quad (2.28)$$

As an alternative, the Addition theorem can also be applied to the line source with vertical and horizontal polarization to find the harmonics of the incident field (see Appendix C).

2.3.3 Total field

We have now developed the solution for the homogeneous equation in Section 2.3.1, and a particular solution to the non-homogeneous equation in Section 2.3.2. The general solution is the sum of these two solutions:

$$\mathbf{E^t_m} = \mathbf{E^s_m} + \mathbf{E^i_m} \tag{2.29}$$

As indicated at the end of Section 2.3.1, we still need to solve for the unknowns A_m, A'_m, B_m, and B'_m from (2.2) - (2.4) to determine the $\hat{z}$ component of the scattered solution. We can re-write the field using the notation developed in Section 2.3.2 as

$$\begin{cases} E^t_{m,z} = A_m J_m(k'_\rho \rho) & \rho \leq a \\ E^s_{m,z} = A'_m H^{(2)}_m(k_\rho \rho) & \rho \geq a \end{cases} \tag{2.30}$$

and

$$\begin{cases} H^t_{m,z} = B_m J_m(k'_\rho \rho) & \rho \leq a \\ H^s_{m,z} = B'_m H^{(2)}_m(k_\rho \rho) & \rho \geq a \end{cases} \tag{2.31}$$

Subscript m indicates the m^{th} harmonic and we implicitly assume the term $e^{jm\phi}e^{-jk_z z}$. As in the case of the incident field, we know the solution in the region inside the cylinder can only consist of Bessel functions while the region outside the cylinder can only consist of Hankel functions. The scattered and incident fields inside the cylinder have the same form so we combine these terms into E^t, which represents the total field, and assign it the constants A and A'. However, the scattered and incident fields outside the cylinder have a different form and cannot be combined together. We can also use the same approach to determine the ϕ-components from the vertical components by applying (2.13) to (2.30) and (2.31).

We can now solve for A_m, A'_m, B_m, and B'_m by applying the tangential boundary conditions of (2.17) - (2.19) to the surface of the cylinder at $\rho = a$. In our case, these boundary conditions state that the tangential fields just inside the cylinder equal the tangential fields just outside the cylinder. We can write this as follows:

$$\mathbf{E^t_{(1)}} = \mathbf{E^t_{(2)}} \tag{2.32}$$

$$\begin{aligned} \mathbf{E^t_{(1)}} &= \mathbf{E^s_{(2)}} + \mathbf{E^i_{(2)}} \\ \mathbf{E^t_{(1)}} - \mathbf{E^s_{(2)}} &= \mathbf{E^i_{(2)}} \end{aligned} \tag{2.33}$$

where $\mathbf{E}^{\mathbf{s}}_{(\mathbf{2})}$, $\mathbf{E}^{\mathbf{i}}_{(\mathbf{2})}$ represent the scattered and incident tangential field components just outside the cylinder, and $\mathbf{E}^{\mathbf{t}}_{(\mathbf{1})}$ represents the total field just inside the cylinder. Similar expressions can be written for the magnetic field. Finally, we can use our previous definitions of these various field components to re-write the second line of (2.33) in matrix format as follows:

$$\begin{bmatrix} J_{(1)} & -H_{(2)} & 0 & 0 \\ -\frac{F_\epsilon \epsilon_r}{k_{\rho 1}} J'_{(1)} & \frac{F_\epsilon}{k_{\rho 2}} H'_{(2)} & \frac{F_m}{k_{\rho 1}^2} J_{(1)} & -\frac{F_m}{k_{\rho 2}^2} H_{(2)} \\ \frac{F_m}{k_{\rho 1}^2} J_{(1)} & -\frac{F_m}{k_{\rho 2}^2} H_{(2)} & \frac{F_\mu \mu_r}{k_{\rho 1}} J'_{(1)} & -\frac{F_\mu}{k_{\rho 2}} H'_{(2)} \\ 0 & 0 & J_{(1)} & -H_{(2)} \end{bmatrix} \begin{bmatrix} A_m \\ A'_m \\ B_m \\ B'_m \end{bmatrix} = \begin{bmatrix} E^{iv}_{m,z} + E^{ih}_{m,z} \\ H^{iv}_{m,\phi} + H^{ih}_{m,\phi} \\ E^{iv}_{m,\phi} + E^{ih}_{m,\phi} \\ H^{ih}_{m,z} \end{bmatrix} \tag{2.34}$$

On the right side of the equations, the terms E^{iv}_m and E^{ih}_m represent the incident fields for vertically and horizontally polarized line-sources with amplitudes I_v and I_h respectively. Their solution was already given in Section 2.3.2. The left side of the equation is obtained from (2.30) and (2.31) using (2.13) to describe the $\hat{\phi}$ components from the $\hat{z}$ components. We have introduced the terms $F_m = \frac{mk_z}{a}$, $F_\mu = j\omega\mu$, $F_\epsilon = j\omega\epsilon_0$ to express the equation more compactly. Similarly, we have also introduced the notation $J_{(i)} = J_m(k_{\rho i}a)$ and $H_{(i)} = H^{(2)}_m(k_{\rho i}a)$, where $i = 1$ and $i = 2$ refer to the material just inside and outside the cylinder respectively.

We could solve (2.34) and express the constants A_m, A'_m, B_m, and B'_m in closed form. However, the resulting expressions are complicated and do not provide any additional insight. Therefore, we will simply solve the equation numerically when we implement the model on a computer in Section 2.4.

The dotted and dashed lines in Fig. 2.4 represent the vertically polarized incident field in free space for k_z=0 and k_z=5k_0, respectively. Because of not defining the incident field inside the body we do not have it in the middle of figure. The electric field far enough from the line source can be approximately represented as a function of $e^{jk_\rho \rho}$ which is roughly equal to $e^{jk_z \rho}$ for large values of k_z. So it is expected to observe a more rapid decay of the fields in the case of k_z=5k_0. By considering the circular lossy cylinder with ϵ_r=51-j31.47 and a=16.4 cm in our model, which is realized by adding the scattered field to the previous incident field at the frequency of 915 MHz, the total field should normally exhibit a strong reduction in the lossy medium, as compared to the incident field in free space. As we see in this figure, since the body is a very

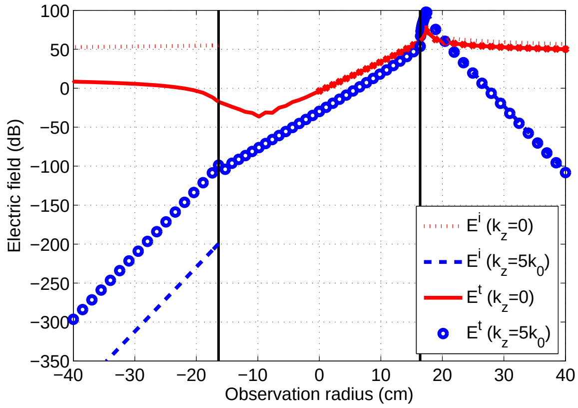

Figure 2.4 Incident and total electric fields (E_z^i and E_z^t) versus observation radius in case of vertical line source excitation close to the body.

lossy medium, the field declines a lot at the back interface of the body ($\rho \leqslant$ -16.4 cm). Theoretically, in the case of a vertically polarized line source with non-zero propagation constant ($k_z \neq 0$) all ρ, ϕ, and z components of both incident and scattered electric fields have non-zero values and can be calculated.

The vertical component of E_z, around and at a short distance from the body, is calculated by our approach and shown in Fig. 2.5 (solid line). Dotted, dashed and circle lines represent the electric fields for a cylinder made by dielectrics 10, 100, and 1000 times more lossy than a normal body. To verify the convergence of our code, we calculated the fields around a PEC cylinder with the same radius as the body and at the same observation points by another code based on the MoM. A thick solid line in Fig. 2.5 shows this field and it is the limit of lossy cylinder's field as its loss tangent approaches infinity.

2.4 Point source

In the previous section, we developed the solution for a line source near a lossy cylinder. Our goal now is to convert the solution for a line-source into the solution for a point source. This can be accomplished using the following FT equivalence:

$$\delta(z) = \frac{1}{2\pi} \int_{-\infty}^{\infty} e^{-jk_z z} dk_z \tag{2.35}$$

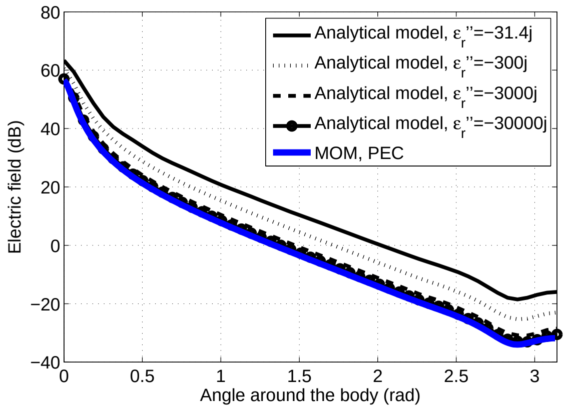

Figure 2.5 E_z as a function of ϕ for lossy cylinders with different conductivity (thin lines) and PEC cylinder (thick line) [1].

In our case, we can see that the left hand side of the equation could represent a point source. We could also interpret the right hand side of the equation to be a sum of line sources each having a current that is a traveling wave with a vertical propagation constant k_z. This is the type of current source we considered in the previous section. From the linearity of Maxwell's equations, we know that the combined field due to several sources is equal to the sum of the fields of each individual source. Therefore, we can write the following:

$$\begin{aligned}\mathbf{E^{pt}} &= \frac{1}{2\pi}\int_{-\infty}^{\infty}\mathbf{E^t}dk_z \\ &= \frac{1}{2\pi}\int_{-\infty}^{\infty}\sum_{m=-\infty}^{\infty}\left(\mathbf{E^s_m}+\mathbf{E^i_m}\right)dk_z \qquad (2.36)\end{aligned}$$

The vector $\mathbf{E^{pt}}$ represents the field due to a point source.

It is too difficult to perform the integration of (2.36) analytically, so we must resort to a numerical integration by computer. Unfortunately, this is complicated by the presence of a pole in the line source solution when $k_z = k_0$. This pole can be seen by noting $k_\rho = \sqrt{k_0^2 - k_z^2}$ as indicated in (2.3). Thus, $k_\rho \to 0$ when $k_z \to k_0$ which will cause the various Hankel functions in our solution to approach infinity. There may be other poles resulting from the solution of (2.34). To avoid these singularities in the line-source solution, we can perform a contour integral in the complex plane around the singularities.

According to Cauchy's theorem [55], an integration contour can be deformed in the complex plane without a change of the integral of an analytical function, if the end points of the original and the deformed paths coincide and there are no singularities between these paths (branch cuts are not being crossed). Since the incident and scattered fields are analytic functions for a complex k_z, we are allowed to deform the contour and circle around the singularities on the $\mathrm{Re}(\mathrm{k_z})$ axis, e.g. $k_z = \pm k$. The right poles in the Figs. 2.6 and 3.5 are below the line Im(k_z)=0 and the left ones are above the line Im(k_z)=0. So, there is no singularity between the original and the deformed paths and the deformation will not change the integration.

We have found that a parabolic contour, defined as in Fig. 2.6, provides a practical numerical integration technique that rapidly converges to a good approximation of the solution. This contour integral can be expressed as:

$$b = C\left(1 - \left(\frac{a - k_0}{k_0}\right)^2\right) \tag{2.37}$$

We must carefully choose the parameter C defining the height of the parabolic contour in Fig. 2.6. If C is too small, then the contour gets too close to the singularity and the integral becomes difficult to evaluate numerically. On the other hand, if C is too large, then the Hankel functions become difficult to evaluate since they increase exponentially with $Im\{k_z\}$. We have simply plotted the integrand and chosen the parameters of integration contour C to produce a smooth result. A broad range of the acceptable height are available and while C is chosen in this range, achieving a converged integral, with respect to the

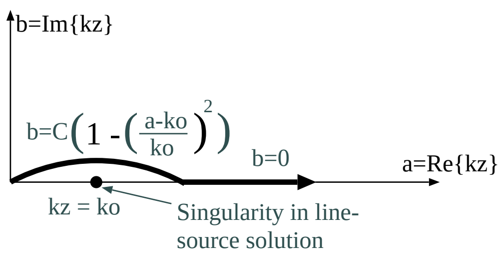

Figure 2.6 A parabolic contour around the singularity at $k_z = k_0$ is a good numerical method for evaluating the inverse FT when converting to a point source.

number of integration terms, is not a sensitive issue. Typically, C is chosen to be a positive number less than 0.01.

Finally, we can only evaluate a finite number of terms to calculate the summation over m. This can be problematic since routines for computing Hankel functions may exhibit numerical overflow problems for large m and small complex or real arguments. Fortunately, this numerical aspect of the problem has already been investigated. A simple recursive formula for obtaining the largest calculable m for Hankel functions has been derived in [56] and can be used to approximate an appropriate number of terms in the summation. Typically, less than 200 terms are required for an accurate solution.

2.5 Body area pathloss trends

We have implemented the analytical model of a point source near a lossy cylinder described in Section 2.4. We are now able to use these expressions to calculate basic pathloss trends around an arbitrary cylinder much faster than with FDTD. Section 2.5.1 investigates propagation trends away from and into the lossy cylinder. Section 2.5.2 investigates propagation trends along and around the surface of a lossy cylinder. We will compare these results with actual measurements around a human body in Section 2.7.

2.5.1 Propagation away and into a lossy cylinder

Frequency (MHz)	*Wavelength in air (cm)*	*Dielectric Constant* (ϵ_H)	*Conductivity* σ_H *(mho/m)*	*Wavelength* λ_H *(cm)*
400	69.3	53	1.43	8.76
915	32.8	51	1.60	4.46
2450	12.2	47	2.21	1.76
6000	5.17	43.3	4.73	0.775

Table 2.1 Electric properties of human tissues with high-water content such as muscle and skin [57].

Fig. 2.7 shows the electric field magnitude expressed in dBV/m as a function of observation radius for a point source just outside a lossy cylinder [2]. It shows the field values for both 400 MHz and 2.45 GHz sources. In both cases, the point source is located at $\rho_s = 0.16$ meters. The lossy cylinder is centered at the origin and has a radius of $d/2 = 0.15$ meters which roughly corresponds to the radius of a typical human torso. It is indicated on the figure with dashed lines. The source is therefore just one centimeter away from the cylinder on the right side.

The frequency-dependent conductivity and permittivity of body tissues are mainly based on the amount of the water (and ionic) content. Tissues with

[2] dBV/m is $20log10(E)$ and represents the magnitude of the electric field in dB relative to 1 V/m

high-water content, such as skin and muscle, have a higher value of conductivity and permittivity than tissues with low-water content, such as bone and fat. The penetration depth of the low-water content and high-water content tissues at 2.45 GHz are almost 2 cm and 10 cm, respectively. We set the material properties of the cylinder according to the high-water content human tissues, as shown in Table 2.1.

The electric field away from the cylinder on the right side of the Fig. 2.7 decays proportionally with distance ($|E|^2 \propto d^{-2}$) as expected in free space. The electric field into the cylinder between the dashed lines is roughly a straight line on our log-linear scale indicating it decays exponentially with distance ($E \propto \exp(-d)$). This is also not surprising since the waves are propagating through a lossy medium and therefore decay exponentially [58]. As expected, the electric field decays more rapidly at 2.45 GHz than at 400 MHz since the skin depth is proportional to the square root of the wavelength [58]. This effect is compounded by the fact that body tissues of high-water content tend to be better conductors at higher frequency. As expected, the field values on the opposite side of the cylinder are much lower since they are more shadowed by the cylinder.

The field in the backside of the body mainly depends on the waves radiating around the cylinder rather than the waves propagating through the lossy cylinder. Thereby, in a certain region in the backside, the level of the field on the surface is higher than that inside the cylinder. Fig. 2.7 shows the local minimum of the electric field inside the cylinder. The field decays roughly exponentially on either side of this minimum. This behavior suggests that, at high frequencies, the fields on the opposite side of the body will result from diffraction *around* the surface of the body rather than penetration *through* the body. This occurs because the body is a relatively good conductor. These results have also been verified with FDTD simulations on more sophisticated models of the body incorporating heterogeneous tissues [59].

Finally, the left side of Fig. 2.7 shows how tangential fields decay rapidly close to the surface of a lossy conductor. For example, the fields on the left edge of the figure are actually higher than the fields next to the cylinder even though they are physically much further away from the antenna. If bodies were perfect conductors, the electric field would vanish on the surface com-

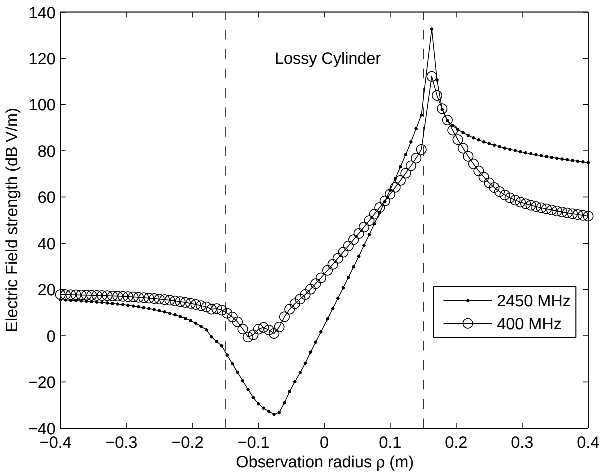

Figure 2.7 Electric field as a function of observation radius for a point source just outside a lossy cylinder. A 1 Amp point source is located at $\rho = 0.16$ meter on the right side of the figure. The lossy cylinder is shown with dashed lines.

pletely. The human body is actually an imperfect conductor, so there will be some tangential component to the electric field. Nevertheless, we can expect this field component to decay rapidly close to the body surface resulting in higher pathloss. Note that a normally polarized electric field would not decay close to the surface of a conductor in the same manner, indicating that antenna polarization will have a fundamental impact on body area propagation and hence communication performance.

2.5.2 Propagation on the surface of a lossy cylinder

Fig. 2.8 shows the electric field magnitude expressed in dB V/m as a function of distance for a 2.45 GHz point source. As before, the lossy cylinder has a radius of $a = 0.15$ meters. The point source is located just 1 centimeter away from the body at $\rho_s = 0.16$ meters. Three curves are presented. The top curve shows the electric field versus distance for a point source in free space. The middle curve shows the electric field versus distance along the front surface of the cylinder. The bottom curve shows the electric field versus distance *around* the surface of the cylinder. The top two curves are obtained using a

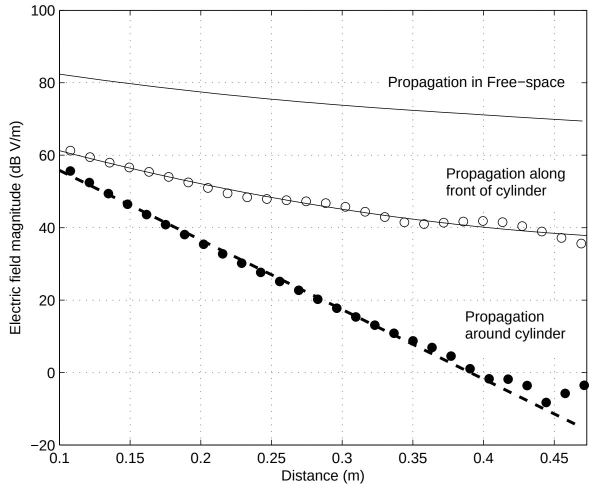

Figure 2.8 Electric field as a function of distance through free-space, along the length of the cylinder, and around the cylinder. The lossy cylinder radius is 0.15 m, and both the observation and source radii are 1 centimeter away from the cylinder. All results are for a frequency of 2.45 GHz and a 1 Amp current.

horizontally polarized point source and calculating the electric field along the $\hat{z}$ direction. For the top curve, we set the material properties of the lossy cylinder to the properties of free space. For the middle curve, we set the lossy cylinder properties according to the high-water content tissues of Table 2.1. The bottom curve was obtained by using a vertically polarized point source and varying the angle of observation $\hat{\phi}$. In all cases, the observation radius is set to the radius of the source ($\rho = \rho_s = 0.16$ m).

We can see from Fig. 2.8 that the two curves along and around the surface of the cylinder (shown with circles and dots respectively) are shifted down compared with the free space curve. As explained in the previous section, this is because we expect the tangential fields to be small close to a lossy conductor compared with fields in free space. It is also clear that we can expect the pathloss versus distance trend on a body to be very sensitive to the trajectory we consider. The electric field will decay significantly more rapidly when considering propagation around a body into the shadow region compared with propagation along the front of a body.

The middle curve, representing propagation along the front surface of the cylinder, decays somewhat faster than in free space. In free space, $|E|^2 \propto d^{-2}$ while we have found that $|E^2| \propto d^{-m}$ with m between 3-3.5 provides a reasonable approximation for different frequencies and radii. The excellent fit of this power law relationship is shown by the dashed line. It is difficult to provide a physical interpretation of this trend other than to say it is a consequence of Maxwell's Equations. We can suggest that higher pathloss trends are normally expected near conducting surfaces due to material losses. However, given the close proximity of the source and lossy surface, other contributions such as surface waves may also influence results.

The bottom curve representing propagation around the cylinder is approximately a straight line on our log-linear scale indicating it decays roughly exponentially with distance ($|E|^2 \propto \exp(-\alpha d)$) with $\alpha \cong$0.4. The excellent fit of an exponential decay law is shown by the dashed line. High-frequency asymptotic approximations for diffraction around curved conducting surfaces based on the Uniform Theory of Diffraction (UTD) also tend to decay exponentially with distance [35]. In this case, waves guided by a curved surface are often called *creeping waves*. Unfortunately, we do not know of any suitable UTD approximations valid for tangentially polarized sources close to a conducting surface [3]. This is because the source and surface are very close with respect to the wavelength we consider. UTD approximations are only valid when the geometry does not vary significantly over an interval on the order of a wavelength [35]. Nevertheless, we propose that the exponential decay our model predicts can be interpreted as creeping waves diffracting around curved surfaces and suggest as future work finding suitable approximations to show this analytically for our geometry. For creeping wave propagation, the rapid attenuation around the body is related to the continuous shedding of energy tangent to the cylinder as a wave rotates around the surface into the shadowed region [35]. Thus, energy is radiated away from the body during the diffraction process which results in a faster pathloss versus distance trend close to the surface of the body. The fluctuation of the curve near the back of the body can be interpreted as the interference of clockwise and counter-

[3]On the other hand, UTD approximations valid for normally polarized sources located on perfectly conducting surfaces are well known [35] and have even been employed in body area propagation studies [18]

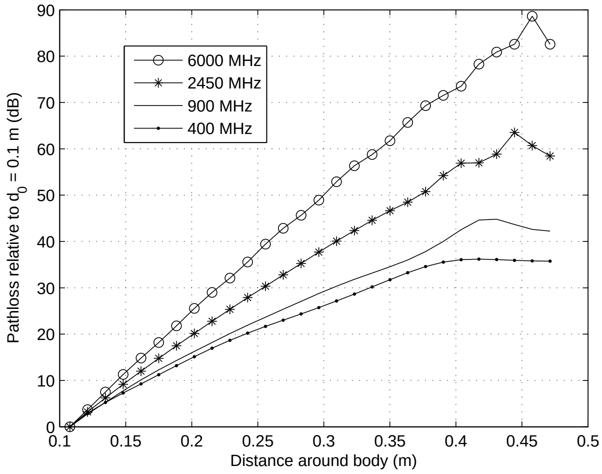

Figure 2.9 Propagation around a lossy cylinder at different frequencies.

clockwise creeping waves. Fig. 2.9 shows the pathloss versus distance trend for propagation around the same 0.15 m radius cylinder at different frequencies. The pathloss is shown in dB relative to the pathloss at a reference distance of 0.1 meters. In general, the rate of exponential decay increases with frequency around a lossy cylinder which is also consistent with creeping wave diffraction [35]. We also see that the curves tend to flatten out on the opposite side of the body with respect to a perfect exponential decay, especially at lower frequencies. This is likely due to clockwise and counter-clockwise diffracting waves interfering with each other on opposite sides of the cylinder.

2.6 Vertical dipole in the presence of the body

We developed a code based on the Method of Moments (MOM) to simulate the current on the vertical half-wavelength dipole antenna, including the effect of the human body. The methodology of inserting the effect of a scatterer on the current of a dipole antenna is explained for a general case, later in Section 3.3. Here, we explain the MoM results in the form of dipole currents with vertical polarization, in the presence of the lossy cylinder and also, for comparison, an infinite PEC plane.

Fig. 2.10 shows a dipole antenna next to an arbitrary-shaped scatterer, that would be a lossy cylinder or an infinite PEC plane. By using the Pocklington's integral equation 3.18, the current on the axis of the wire can be obtained from the tabulated scatterer Green's function.

We consider an infinite lossy cylinder, with diameter d=2a, whose axis is coincident with $\hat{z}$. The relative permittivity of this cylinder has been considered equal to that of the human body at 2.45 GHz, ϵ_r=47-16.22j. Fields outside and inside the infinite cylinder do not vary with z. However, after adding a z-dependent excitation, e.g. a vertical point source located at (ρ_s,ϕ_s,z_s), the fields are not independent from z anymore. However the fields for an observation point with a fixed (z-z_s) remain independent from z. This translational symmetry along z helps us to simplify the expression of scattered fields and to tabulate the Green's function with a 1-D matrix. Fig. 2.11 shows the scattered fields versus observation height z for a source located at z=0. It gives an idea of how scattered fields are decreasing by going further from the source, in the $\hat{z}$ direction and for a given observation radius. This figure also shows higher scattered fields for the source and observation points closer to the body.

The difference between the scattered field from perfectly infinite conducting plane and infinite lossy cylinder (Fig. 2.11), more visible at the place of the minimum, produce a difference in the current of the antenna, as we will show in the following. Minimums in the scattered fields E_z^s from the lossy cylinder and infinite PEC plane are due to destructive interference of the field compo-

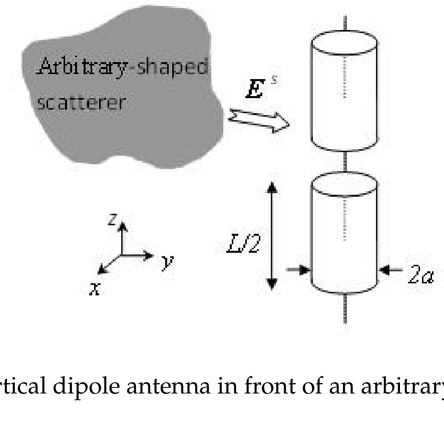

Figure 2.10 Vertical dipole antenna in front of an arbitrary-shaped scatterer.

nents. However, these interferences do not happen in the same value of z for real and imaginary parts and so it cannot provide a null.

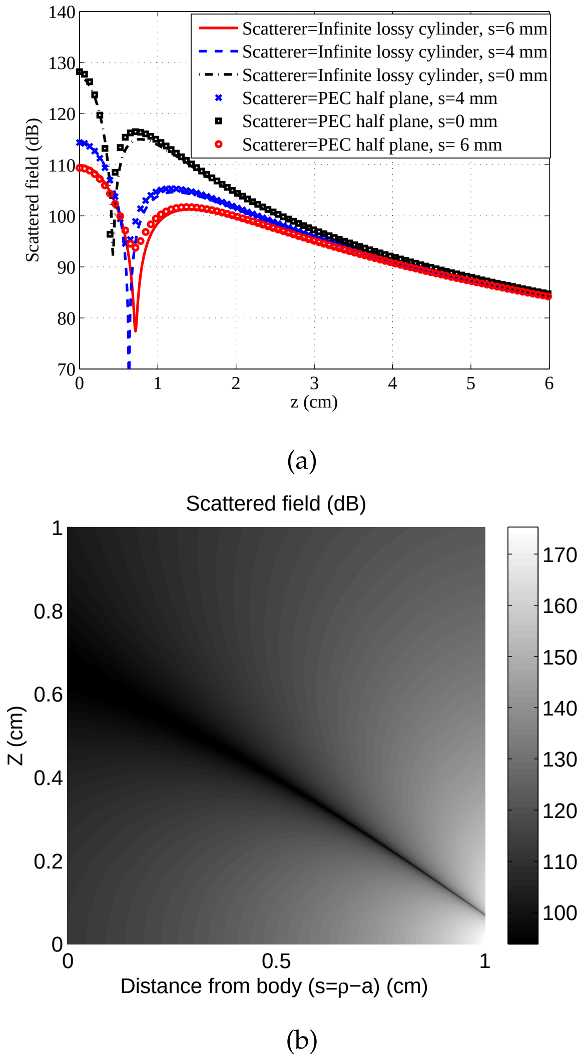

Figure 2.11 (a) Numerical scattered fields (E_z^s) from an infinitely lossy cylinder and also analytical ones from perfectly conducting half plane, for different observation radii. (b) 2D representation of E_s^z for different ρ and z of the observation point. The 1 A.m. point source is located at (ρ_s=14.6, ϕ_s=0,z_s=0). The relative permittivity of the infinite lossy cylinder (d=28 cm) at 2.45 GHz equals to 47-16.22j.

At 2.45 GHz, we can consider the human body as a quite lossy cylinder. To compare the effects of human body and an infinite PEC plane on the current of a dipole antenna, we gradually increased the conductivity of the lossy cylinder and found the current of the dipole at a distance s from the cylinder. To do that, we inserted the tabulated $\mathbf{E}^s$ of the infinite lossy cylinders, shown in Fig. 2.11 for arbitrary $\triangle z$=$|z - z_s|$, in our MOM code. Fig. 2.12 shows currents on the dipole antenna located just outside and at a distance s from the cylinders with several conductivities; ϵ_r=47-16.22j, 47-162.2j, and 47-8110j. A generator (a balanced voltage source) with the Thevenin equivalent voltage of V_{th}=1 V and the Thevenin equivalent impedance of R_{th}=50 Ω feeds the dipole at its center (see the inset of Fig. 3.12). Because of the body finite conductivity, the antenna current distribution in the presence of the body is smaller than the current in front of the PEC plane.

Since the current induced on the outer part of conductor creates an in-phase current on the dipole antenna, we see an increase in the total current of the dipole antenna when it is close to the infinite PEC plane. This increase of the current can be represented by the fact that the dipole antenna is approximately *short-circuited* by the infinite PEC plane. As shown in Fig. 2.12, the human body at 2.45 GHz provides a relatively big change on the antenna current distribution, at a few millimeter distances. With relatively same cosine shapes of antenna currents, we see 33% and 19% increases in the maximum of the antenna current located at 6 mm and 4 mm from the human body, respectively. Increasing the conductivity of the lossy cylinder, or approaching the dipole to the scatterer, causes stronger scattered fields and thereby leads to an increase in the total current on the dipole antenna, with similar cosine shapes of the antenna currents. The equivalent currents induced on the outer part of lossy cylinder creates an in-phase current on the dipole which can be regarded as the dipole being almost "short-circuited" by the conducting cylinder. In this case, the fields radiated by currents on the conducting cylinder(the image of the dipole antenna) can almost cancel those radiated directly by the dipole antenna.

The input impedance of the dipole antenna parallel to the human body and also an infinite PEC plane is shown in Fig. 2.13. From Fig. 2.12 we know that the magnitude of the input impedance of the antenna in the presence of the human body is higher than that in the presence of an infinite PEC plane.

By increasing the distance between the antenna and scatterer, the values of the resistance and reactance will approach the corresponding values of the isolated element, Z_m=73+42.5j [25].

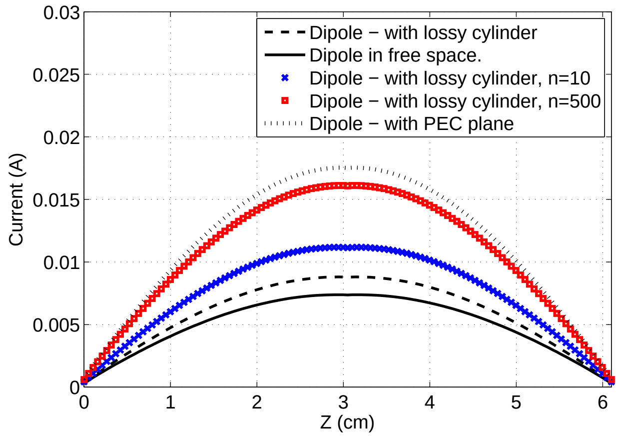

(a)

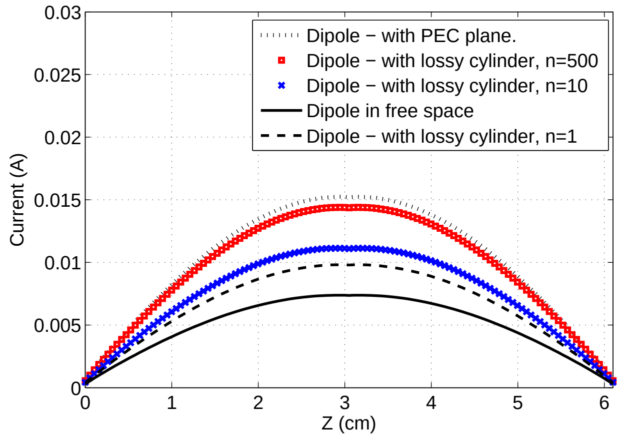

(b)

Figure 2.12 Normalized currents on a vertical dipole in (a) 4 mm and (b) 6 mm away from a lossy cylinder (d= 28 cm) with different losses; ϵ_r=47-j16.22n in which n is equal to 1,10, and 500. They are also compared with the currents of a dipole antenna in front of an infinite PEC plane.

From the results of the currents on the dipole antenna in the presence of the body, we have the basis function coefficients. Finding the entry of the MoM matrix for testing functions at arbitrary points can provide us the tested electric fields in those points. As a simple example, Fig. 2.14 shows the vertical electric fields (E_z) versus z for (ρ=ρ_s, ϕ=ϕ_s=0) with and without the presence of the human body. Theoretically, within -$L/2$< z <$L/2$ the vertical field is estimated tangential to the dipole antenna and should be zero; actually that was imposed by the MOM technique to get the BF coefficient. The peak at the center of the figure (z=0) is related to the dipole excitation. As shown in Fig. 2.14, a lossy cylinder with the same characteristics as the human body can reduce the electric fields by 21 and 16 dB for an observation point at $\lambda/2$ and λ distances from the edge of the antenna, respectively, when it is oriented parallel to the half-wavelength dipole antenna.

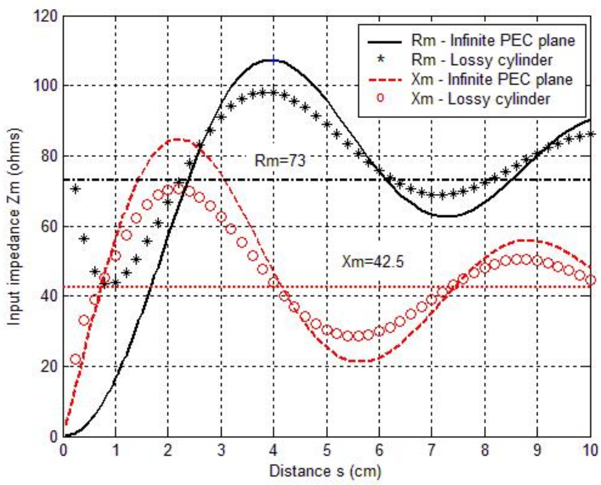

Figure 2.13 Input impedance (Z_m=R_m+jX_m) of a vertical half-wavelength dipole antenna at 2.45 GHz, when the antenna is parallel and close to the infinite PEC plane and infinite lossy cylinder with the same parameters as human body (a=14cm, ϵ_r=47-j16.22).

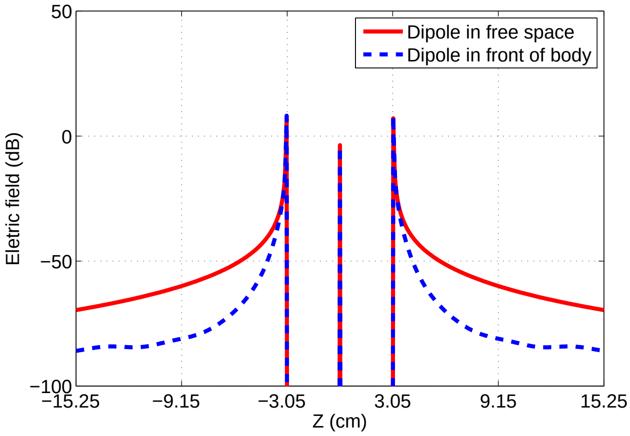

Figure 2.14 Total vertical electric fields (E_z) versus z for vertical half-wavelength dipole antenna (L=0.5λ) placed 4 mm away from an infinite lossy cylinder. The cylinder radius is 14 cm, ϵ_r=47-16.22j, and λ=12.2 cm. The dipole excitation by the gap causes the peak at the middle of the dipole [25].

2.7 Comparison with measurements

Obviously, the geometry considered in the previous sections does not perfectly represent an antenna and body. Thus, we have compared the pathloss trends predicted by our simplified lossy-cylinder model with measurements of the electric field close to the human body using actual antennas. Section 2.7.1 describes our measurement setup, while Section 2.7.2 compares our model and measurement results.

2.7.1 Measurement setup

An HP8753ES VNA is used to measure the S_{21} parameter between two antennas placed at various positions on a human body in an anechoic chamber. The two antennas are connected to the VNA using 6 meter low-loss coaxial cables. Measurements are taken at 915 MHz and 2.45 GHz. We focus on these frequencies since they represent unlicensed ISM bands available internationally [60], and are also used by recent narrowband standardization efforts such as Zigbee [61] and Bluetooth [62].

The same small, low-profile Skycross SMT-8TO25-MA [63] antennas are used for all measurements. The antennas are 50.5 by 28 by 8 mm in size and weigh only 4.2 grams. These antennas were chosen since they are close to the size and profile requirements typical of comfortable body worn sensor devices [5]. Furthermore, they have a wide bandwidth which minimizes degradation resulting from the antenna being de-tuned when placed near the body [64]. In case of a narrow bandwidth antenna, a small de-tuning can shift the operating

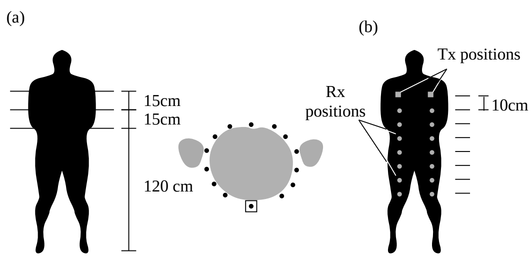

Figure 2.15 Experimental setup: measurement locations (a) around body and (b) along body.

frequency and thereby it leads to a strong mismatch. Nevertheless, antennas with a wider bandwidth can see their matching degraded (over all or part of the band) when placed near the body.

The distance between the body and the antenna can significantly influence the pathloss and needs to be carefully controlled [13]. We control this separation by putting a 5 mm dielectric between the body and the antenna. In the same manner as [20], the antenna is taped to this dielectric and held against the body using tight elastics so they can not move while a measurement is being made. In all cases, the antennas are mounted so they are vertically polarized parallel to the body surface.

We analyze the antenna matching by measuring the S_{11} parameter in free-space and close to the body. In free space, the S_{11} parameter is below -10 dB across the band of interest indicating the measurement setup itself does not introduce significant matching loss. When mounted on the body, the S_{11} parameter can vary depending on the placement of the antenna on the body. It remains good at 915 MHz ($S_{11} <$ -10 dB) but in some cases becomes marginal at 2.4 GHz ($S_{11} <$ -5 dB). It is possible that the coaxial cable and connector may radiate energy influence the pathloss versus distance trends. However, the display on our VNA remains stable when we move the cables indicating they do not radiate enough energy to appreciably alter our results.

Fig. 2.15a shows where the antennas are placed around the torso. All channel parameters are extracted from measurements performed in 3 planes separated by approximately 15 cm along the vertical axis (see left diagram). The right diagram shows where the antennas are placed for each plane. The receiver positions are marked with circles, while the transmitter is marked with a box around the circle. The transmitter is always placed on the front, and the receiver is placed at distances of 10 - 45 cm in steps of 5 cm measured around the perimeter of the body.

Fig. 2.15b shows where the antennas are placed for communication along the torso. The transmitter is worn at approximately shoulder height at one of two different positions. The receiver is placed directly below the transmitter at seven positions separated by 10 cm covering the range from the shoulder to the knees. To gather more measurement points, we repeat the procedure on the back of the body.

2.7.2 Measurement and model comparison

In this section, we present some measurement results achieved by Andrew Fort [2, 65]. We compare the pathloss versus distance measured around and along the body with the analytical model developed in Sections 2.3 - 2.4, where we simplified the problem by approximating the human body and the antenna with a lossy cylinder and an infinitesimal current source, respectively. The infinitesimal current source in the analytical model is an approximation of the small and low-profile Skycross SMT-8TO25-MA antenna that has been used in the measurements. We try to measure the pathloss without the influence

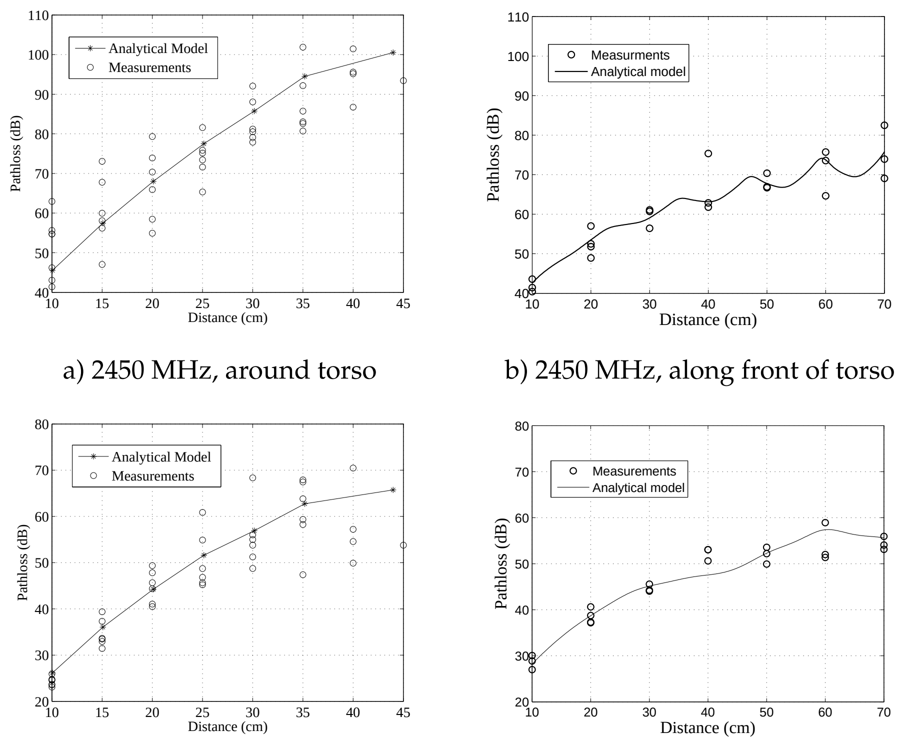

a) 2450 MHz, around torso

b) 2450 MHz, along front of torso

c) 915 MHz, around torso

d) 915 MHz, along front of torso

Figure 2.16 Comparison of the analytical model for propagation around/along a cylinder and measurements around/along a real human body in an anechoic chamber [2].

of the nearby scatterers. To eliminate reflections from the walls, we perform the measurement inside an anechoic chamber and we surround the VNA by absorbing barriers. However, our anechoic chamber is not perfect and the fields reflected from walls might influence the received power in the backside of the body. We use an input power of 5dBm, a sweep speed of 5ms, and we averaged together 5 measurements taken consequently.

Fig. 2.16 shows the pathloss versus distance around the body and along the body for 2.45 GHz and 915 MHz frequencies with the analytical model developed in Sections 2.3 - 2.4. In Fig. 2.16, the vertical axis represents the pathloss and the horizontal axis is the distance traveled by the wave around or along the surface of the body. The circles indicate individual measurements, while the solid line was calculated using our physical model derived from Maxwell's equations. The torso used in this experiment has a radius of between 13-15 cm depending on the height at which the measurement is made. Thus, we use a cylinder radius of $a = 14$ centimeters and placed the antenna and observation point at $\rho_s = 14.5$ centimeters away from the lossy cylinder in our analytical model. Furthermore, we set the material properties to the high-water content tissues of Table 2.1. Since a point source does not exhibit the same near-field losses as the antenna used in our experiment, the analytical results are normalized to minimize the mean squared error.

The analytical model of a lossy cylinder matches the average trends of the measurements around a real body remarkably well considering the gross simplification of the body shape and antenna. As predicted by Maxwell's Equations, propagation around the body results in a more rapid attenuation versus distance trend than propagation along the body. However, there is a large variance in the pathloss measured at a particular distance around the torso consistent with other measured and simulated results [18]. This variance can be attributed to several physical factors including random interaction of the antenna and body at different locations, reflections off the arms, and variations in the local curvature or tissue properties. Since our analytical model is based on a uniform lossy cylinder and does not incorporate antenna losses, we can not expect it to take into account these fluctuations. This effect is better analyzed using statistical models based on either measurements or FDTD simulations. Some researchers have proposed modeling these contributions using a log-normal random variable since many of the effects are multiplicative [18,21,22].

Comparing the top two figures with the bottom two figures, it is clear that the pathloss within 10-20 centimeters of the antenna is significantly lower at 915 MHz than at 2.45 GHz. This indicates that the losses for these particular antennas are lower at 915 MHz than at 2.45 GHz. Part of this can be explained by the higher matching losses at 2.45 GHz compared with 915 MHz. Furthermore, at least in free-space, the antennas are constant gain (non-constant aperture) between 800 MHz - 2.45 GHz resulting in an attenuation of higher frequencies. However, the antenna properties are also affected by the nearby body and propagation is along the body surface rather than through free-space.

Finally, similar pathloss trends for tangentially polarized antennas have been reported in the literature consistent with our theoretical derivations [12, 21, 22]. However, pathloss measurements in office building rather than in an anechoic chamber tend to flatten out on the back of the body in comparison with Fig. 2.16 due to the presence of nearby scatterers [12,20,22], and can also exhibit small-scale fading due to the interference of diffracting components near the body with reflections from nearby scatterers [22].

2.8 Conclusions

We have proposed a simplified physical body area propagation model derived directly from Maxwell's equations. The model assumes the body can be approximated as an infinite lossy cylinder and the antenna can be approximated as a point source just outside the cylinder. A complete derivation starting from Maxwell's equations was developed together with a practical numerical method for evaluating it on a computer. We then used this model to identify the following approximate body area propagation trends which can be used to justify more sophisticated empirical models:

- $|E|^2 \propto d^{-2}$ away from the body
- $|E|^2 \propto \exp(-\alpha d)$ into the body
- $|E|^2 \propto \exp(-\beta d)$ around the body

- $|E|^2 \propto d^{-m}$ along the body with $m \approx 3 - 3.5$

The electric field (E) is inversely proportional to the distance away from the body in free space. However, the field has a much more rapid exponential decay into and around the body. The exponential decay into the body is expected in a lossy medium. Along the front of the body, the pathloss versus distance decays more rapidly than in free space but does not follow the same rapid exponential trends as propagation around the body. The decay rates (α, β, and m) depend on several factors including the tissue properties, frequency, polarity, and proximity to the body. While they cannot be evaluated directly, they can be estimated easily from our analytical model much faster than with numerical simulation methods such as FDTD.

For the first time, we have shown how the average pathloss trends of small tangentially polarized antennas measured in an anechoic chamber closely follow the trends predicted from Maxwell's Equations for propagation around and along a lossy cylinder. As predicted, pathloss due to diffraction around the body is significantly higher than pathloss along the body. There is a large variance in the pathloss measured at a particular distance around the torso. This variance can be attributed to several physical factors including random interaction of the antenna and body at different locations, reflections off the arms, and variations in the local curvature or tissue properties.

We have also shown how the input impedance of the dipole antenna changes in the presence of the body. The Green's functions are also used in MOM code to show the decrease of the field when the antenna orientation is parallel and close to the human body.

Body Area Propagation Model for Normal-to-Body Antennas

3

3.1 Introduction

The Green's function for an infinite circular or elliptical cylinder in free space can be determined analytically from Maxwell's equations [66–69]. Such Green's functions have been used for validation purposes in [44,45]. In Chapter 2, we have used a FT technique to find the cylinder Green's function due to a tangentially-polarized point source from the solution of the line source with an arbitrary wave-number [1,2,24,25,29,49]. The proposed model has identified the body area pathloss trend as follows: along the front of the body, the pathloss versus distance decays more rapidly than in free space, but does not follow the fast trend found around the body. The decay rates depend on several factors including the body tissue properties, frequency, polarity, and proximity to the body.

The normal-to-body polarization is the most effective polarization in producing fields in the shadow region of the body [44,45,47]. Hence, the normal-to-body components of the antenna current play the main role in establishing the on-body communication link. On the other hand, the body has a small effect on the current of a radially-oriented dipole antenna, when its distance from the body is bigger than a certain small value (see Section 3.3.2). Hence, we perform our analysis and experiments on the normal-to-body dipoles.

In order to design body-worn antennas for on-body communications, it is necessary to investigate the effects of the human body, mainly containing lossy tissues, on the return loss and the near-field radiation pattern of closely mounted antennas. The near-field radiation pattern of the antenna is defined as the distribution of fields versus the three coordinates of space in the vicinity of the antenna. The far-field pattern may not provide a complete picture, especially knowing that the antennas occupy a non-negligible space with respect to the wavelength. It means that the point source approximation of a BAN antenna is not valid anymore and we have to develop a MoM analysis to calculate accurately the antenna current. Hence, in this chapter, we go directly for the transmittance between dipole antennas, obtained from the excited current and the coupled current of antennas. We consider a pair of them at a small distance from the infinite cylinder that represents the body and we model the transmittance between standard on-body antennas that carry normal-to-body currents. In spite of the fact that the normal-to-body dipole is not sufficiently compact enough to be immediately applicable for BAN technology, the analysis can be extended to low-profile on-body antennas.

The case of the radially-polarized point source excitation (Fig. 3.1) makes the cylindrical source decomposition adopted in Chapter 2 impractical, because the coefficients of the field harmonics cannot be calculated from the tangential current intensities. The addition theorem has been used in Chapter 2 to represent outward-traveling waves from the line source with parallel polarizations [49]. For a radially-polarized point source, we propose a *modified addition theorem* for Bessel and Hankel functions and exploit it to produce a cylindrical wave decomposition of the incident field. The cylindrical field harmonics from the radially polarized point source, together with the characteristic matrix of the cylinder (the one expressing boundary conditions) are calculated to provide the fields scattered by the cylinder. After tabulating the scattered fields around the cylinder for different point source distances d_s, we impose the boundary conditions in an integral equation approach to calculate the current on a normal-to-cylinder dipole antenna and, accordingly, we calculate the transmittances between on-body dipoles. The analytical/MoM transmittance between the dipoles on the infinite lossy cylinder is in a good agreement with the measured transmittance between the on-body dipoles.

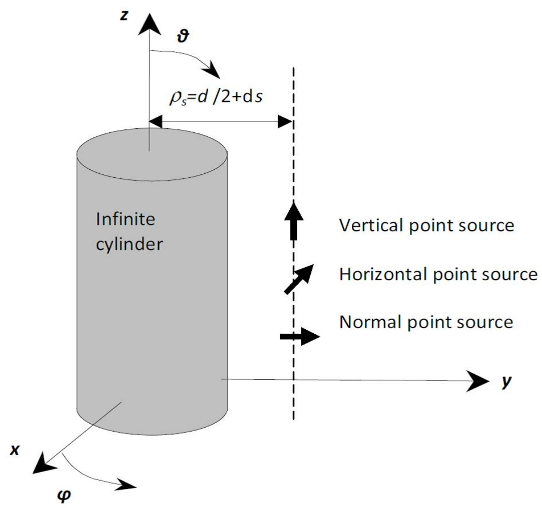

Figure 3.1 An infinite lossy cylinder (ϵ_r=47-16.22j) along the $\hat{z}$-axis with radius of a=$d/2$, representing the simplified body trunk, close to point sources with three possible polarizations, i.e. vertical, horizontal, and normal ones.

This chapter is organized as follows. In Section 3.2, the cylinder Green's function due to a point source with radial polarization is calculated and the results are tabulated to be used in Section 3.3, where the MoM is used to find the current distribution on a normal dipole antenna at f=2.45 GHz. The transmittance results between two radially polarized dipoles have been validated with measurement results and also with results obtained with the *CST Microwave Studio*® software [70]. Section 3.4 summarizes and discusses the contributions of this chapter.

3.2 Radiated fields due to a normal point source close to the cylinder

Fig. 3.1 shows our approach to body area modeling. An infinite circular cylinder of radius a=$d/2$=15 cm is oriented along the $\hat{z}$ axis at the origin of the system of coordinates. According to the average parameters of the human tissue at f=2.45 GHz [6,57], we set the frequency-dependent properties of the cylinder materials $\epsilon(\omega) - j\sigma(\omega)/\omega$ to the conductivity of σ=2.21 S/m and the relative permittivity of ϵ_r=47-16.22j. There are three possible polarizations for a point source located close to the cylinder, i.e. vertical, horizontal, and normal. In this section, we consider the normal point source and the goal is to calculate the cylinder-scattered fields due to the radially polarized point source located at an arbitrary distance d_s from the cylinder.

3.2.1 General approach

The total electric field consists of the incident field from the source and the cylinder-scattered field. In order to obtain the cylinder-scattered fields, we first have to calculate the incident fields from a line source ($\mathbf{E}^{il}$) with an arbitrary k_z (wave vector along the $\hat{z}$ axis). The line source derivation is carried out in Section 3.2.2, by proposing a modified addition theorem for the Bessel functions. In Section 3.2.3, scattered fields due to the line source $\mathbf{E}^{sl}$ are computed by imposing the cylinder boundary conditions. Finally, the cylinder-scattered field due to a point source $\mathbf{E}^{sp}$ is obtained by numerically integrating $\mathbf{E}^{sl}$ over k_z, accomplished by using:

$$\delta(z) = \frac{1}{2\pi}\int_{-\infty}^{\infty} e^{-jk_z z}\mathrm{d}k_z \Longrightarrow E_{point} = \frac{1}{2\pi}\int_{-\infty}^{\infty} E_{line}(k_z)\mathrm{d}k_z \qquad (3.1)$$

where k_z is the wave vector along z and δ is the Dirac delta function. For verification, the same numerical integration technique, giving the free-space point source fields from the line source ones, is applied to the incident fields and the results are compared with the exact analytical expressions.

3.2.2 Derivation of the line source incident fields $\mathbf{E}^{il}$

Fig. 3.2 shows details of the geometry we are dealing with in this section to determine the incident fields. Although there is no cylinder in the incident field calculations, we consider the coordinate origin at the center of the removed cylinder. Without loss of generality, we place the line source at (ρ=ρ_s, ϕ=0) and we try to find $\mathbf{E}^{il}$ at an arbitrary point located at (ρ, ϕ, z=0). The current on the line source varies along the $\hat{z}$ axis as $e^{-jk_z z}$. $\mathbf{E}^{il}$ can be described

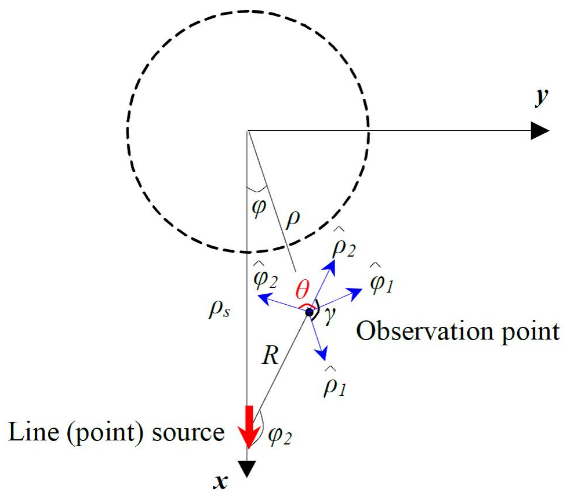

Figure 3.2 Top view of a radially polarized line (point) source (ρ=ρ_s, ϕ=0, z=0) and the observation point (ρ, ϕ, z=0).

based on its cylindrical harmonics as:

$$\mathbf{E^i} = \sum_{m=-M}^{M} \{E^i_{m\rho}\hat{\rho} + E^i_{m\phi}\hat{\phi} + E^i_{mz}\hat{z}\} e^{jm\phi} e^{-jk_z z} \tag{3.2}$$

where k_z is the wave vector along z, m is the cylindrical harmonic order, and ($r\hat{h}o$, $p\hat{h}i$, $\hat{z}$) refer to the cylindrical unit vectors.

To represent the outward-traveling waves from the line source, we use the addition theorem [71] applied to the second-kind Hankel functions, to obtain the vector potential ($\mathbf{A}^l$) [72]:

$$\mathbf{A}^l = \frac{\hat{x}}{4j} H_0^{(2)}(k_\rho|\rho - \rho_s|) = \frac{\hat{x}}{4j} \sum_{m=-\infty}^{\infty} H_m^{(2)}(k_\rho \rho_s) J_m(k_\rho \rho) e^{j(m\phi - k_z z)} \tag{3.3}$$

where ρ_s (larger than ρ) is the radial distance of the source from the origin and ${k_\rho}^2$+${k_z}^2$=k^2. Vector potentials in the directions of ρ and ϕ, ${A_\rho}^l$ and ${A_\phi}^l$, are calculated respectively, by describing the x-unit vector ($\hat{x}$) along ρ and ϕ directions ($\hat{\rho}$, $\hat{\phi}$):

$$A^l_\rho = \cos\phi H_0^{(2)}(k_\rho|\rho - \rho_s|) \frac{e^{-jk_z z}}{4j} \tag{3.4}$$

$$A^l_\phi = -\sin\phi H_0^{(2)}(k_\rho|\rho-\rho_s|)\frac{e^{-jk_z z}}{4j} \tag{3.5}$$

According to Appendix A, (3.4-3.5) can be written using only order-m Hankel and Bessel functions and their derivatives:

$$A^l_\rho = \frac{1}{4j}\sum_{m=-\infty}^{\infty}\{\frac{m^2}{k_\rho^2\rho\rho_s}H_m^{(2)}(k_\rho\rho_s)J_m(k_\rho\rho) + H_m^{\prime(2)}(k_\rho\rho_s)J_m^\prime(k_\rho\rho)\}e^{j(m\phi-k_z z)} \tag{3.6}$$

$$A^l_\phi = \frac{1}{4}\sum_{m=-\infty}^{\infty}\frac{m}{k_\rho}\{\frac{H_m^{(2)'}(k_\rho\rho_s)J_m(k_\rho\rho)}{\rho} + \frac{H_m^{(2)}(k_\rho\rho_s)J_m^\prime(k_\rho\rho)}{\rho_s}\}e^{j(m\phi-k_z z)} \tag{3.7}$$

which amounts to using a modified addition theorem (see Appendix A). From there, the harmonics of the electric and magnetic fields in the z direction can be derived in terms of m^{th} order Bessel and Hankel functions:

$$E^{il}_{z,m} = \frac{1}{j\omega\epsilon}\nabla_z\cdot\mathbf{A}^l_m = -\frac{\eta k_z}{k}H_m^{\prime(2)}(k_\rho\rho_s)Q_m \tag{3.8}$$

$$H^{il}_{z,m} = \nabla_z\times\mathbf{A}^l_m = \frac{jm}{k_\rho\rho_s}H_m^{(2)}(k_\rho\rho_s)Q_m \tag{3.9}$$

$$Q_m = \frac{J_m^\prime(k_\rho\rho)}{\rho} + k_\rho J_m^{\prime\prime}(k_\rho\rho) - \frac{m^2}{k_\rho\rho^2}J_m(k_\rho\rho) \tag{3.10}$$

The harmonics of the fields with polarizations tangential to the cylinder interface ($E^i_{z,m}$, $H^i_{z,m}$, $E^i_{\phi,m}$, and $H^i_{\phi,m}$) are required upon imposing the boundary conditions. As recalled in Appendix B, the ρ and ϕ components of the field can be obtained from the z component [51].

Fig. 3.3 shows the incident electric fields due to line sources for wave vectors k_z=0, 0.75k, and 1.25k, for the following parameters: the radius of the cylinder is a=$d/2$=15 cm and the observation point and the point source are located at 0 and 3 cm distances from the cylinder, i.e. ρ=15 cm, and ρ_s =18 cm. Knowing that k_ρ^2+k_z^2=k^2=ω^2/c^2 where c is the velocity of light, we expect a more rapid decay of the fields for $k_z/k \gg 1$. In that case, k_ρ almost equals jk_z which leads to more evanescent waves versus radial coordinates. Independently from k_z, the line source along z direction and with radial polarization (Fig. 3.2) cannot create E^{il}_ϕ at ϕ=0 and ϕ=180, where E^{il}_ϕ is perpendicular to the source polarization.

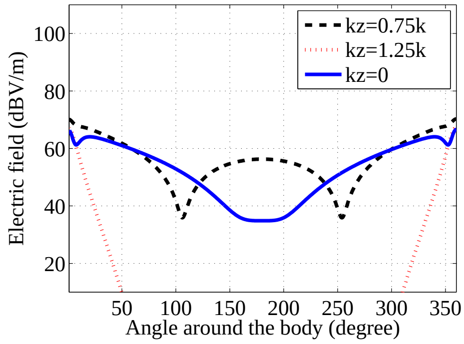

(a)

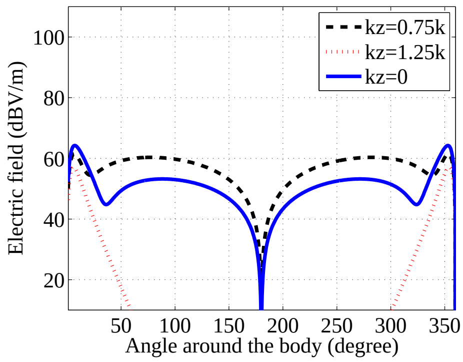

(b)

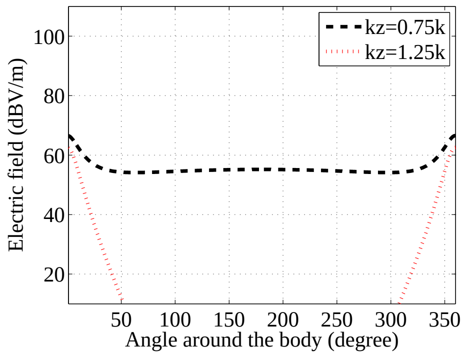

(c)

Figure 3.3 (a) ρ-component (E_ρ^{il}), (b) ϕ-component (E_ϕ^{il}), (c) z-component (E_z^{il}) of the incident electric fields, due to a line source along z axis with radial polarization. The frequency is f=2.45 GHz, the observation points and the source points are located at ρ=15 cm, and ρ_s=18 cm, respectively.

3.2.3 Cylinder-scattered fields from radially-polarized point source

Here, we use the results of Section 3.2.2, i.e. the incident fields from the radially polarized line source, to solve the Helmholtz equations by the separation of variables method in order to find the scattered fields from the infinite lossy cylinder [73]. The z components of the electric and magnetic fields inside and outside the lossy cylinder with radius of $d/2$=a (Fig. 3.1), are given by:

$$E_z^{sl} = \sum_{m=-\infty}^{\infty} e^{jm\phi} e^{-jk_z z} \times \begin{cases} A_m J_m(k'_\rho \rho) & a \geq \rho \\ A'_m H_m^{(2)}(k_\rho \rho) & \rho \geq a \end{cases} \tag{3.11}$$

$$H_z^{sl} = \sum_{m=-\infty}^{\infty} e^{jm\phi} e^{-jk_z z} \times \begin{cases} B_m J_m(k'_\rho \rho) & a \geq \rho \\ B'_m H_m^{(2)}(k_\rho \rho) & \rho \geq a \end{cases} \tag{3.12}$$

where k_ρ=$\sqrt{k^2 - k_z^2}$ and k'_ρ=$\sqrt{k'^2 - k_z^2}$ are the radial wave vectors outside and inside the cylinder, respectively with k'=$k\sqrt{\epsilon_r}$.

The number of harmonics M needed to approximate the scattered field to a given accuracy depends on the positions of the point source and observation points. In the case of close vicinity to the cylinder (ρ_s or ρ < 2 cm) the summation needs to have high number of harmonics $M \cong 150$, but for the rest of the cases $M \cong 50$ is enough. The constants A_m, B_m, A'_m, and B'_m are determined from the boundary conditions imposed by the geometry. Other components of the scattered electric and magnetic fields, i.e. $E^{sl}_{\rho,m}$, $E^{sl}_{\phi,m}$, $H^{sl}_{\rho,m}$, and $H^{sl}_{\phi,m}$ are obtained in Appendix B from the z components. In [2], the authors expressed the boundary conditions in matrix form in terms of tangential components of electric and magnetic fields for each (m, k_z) harmonics. The corresponding equation is found in (3.13). More details regarding the derivation of the cylinder matrix have been explained in Chapter 2. Since the cylinder matrix is characterized by the scatterer (lossy cylinder) and is independent from the source, we can use the same matrix as in Chapter 2, in the case of the radially polarized point source excitation, as studied here. The calculated incident field harmonics in Section 3.2.2 is introduced in the right hand side of (3.13) to provide the scattered field coefficients, i.e. A_m, B_m, A'_m, and B'_m of (3.11) and

(3.12).

$$\begin{bmatrix} J_m(k'_\rho a) & -H_m^{(2)}(k_\rho a) & 0 & 0 \\ -\frac{j\omega\epsilon_0\epsilon_r}{k'_\rho} J'_m(k'_\rho a) & \frac{j\omega\epsilon_0}{k_\rho} H_m'^{(2)}(k_\rho a) & \frac{mk_z}{ak_\rho'^2} J_m(k'_\rho a) & -\frac{mk_z}{ak_\rho^2} H_m^{(2)}(k_\rho a) \\ \frac{mk_z}{ak_\rho'^2} J_m(k'_\rho a) & -\frac{mk_z}{ak_\rho^2} H_m^{(2)}(k_\rho a) & \frac{j\omega\mu_0\mu_r}{k'_\rho} J'_m(k'_\rho a) & -\frac{j\omega\mu_0}{k_\rho} H_m'^{(2)}(k_\rho a) \\ 0 & 0 & J_m(k'_\rho a) & -H_m^{(2)}(k_\rho a) \end{bmatrix}$$
$$\times \begin{bmatrix} A_m \\ A'_m \\ B_m \\ B'_m \end{bmatrix} = \begin{bmatrix} E_{mz}^{iP} \\ H_{m\phi}^{iP} \\ E_{m\phi}^{iP} \\ H_{mz}^{iP} \end{bmatrix} \tag{3.13}$$

Fig. 3.4 shows all scattered field harmonics (E_ρ^{sl}, E_ϕ^{sl}, and E_z^{sl}) for different axial wave vectors, k_z=0, 0.75k, and 1.25k. The line source, radiating at f=2.45 GHz, is located in front of the cylinder and in 3 cm away from it (ϵ_r=47-16.22j, ϕ_s=0, $d/2$=a=15 cm, and ρ_s=18 cm). The observation points are located on the cylinder-air interface (ρ=15 cm). The scattered field harmonics are predicted to show a maximum in front of the cylinder at ϕ=0. However, this maximum is shifted a few degrees ($\cong 6°$) in the ϕ component of the scattered field, because the scattered field has zero values in the front (ϕ=0) and in the back ($\phi = 180°$) of the cylinder.

By solving (3.13) and expressing the constants A_m, B_m, A'_m, and B'_m in closed form, we find the singularities in the line-source solution. Equation (3.14) gives the eigenvalues equations of the cylinder matrix; the poles in the complex k_z-plane are shown in Fig. 3.5 for cylinders with permittivity values of ϵ_{r1}=51-37j and ϵ_{r2}=51-74j.

$$X_m^2 + Y_m^2 - \frac{\epsilon_r + \mu_r}{\sqrt{\mu_r\epsilon_r}} X_m Y_m - \left(\frac{mk_z(\mu_r\epsilon_r - 1)}{k'^2 d}\right)^2 = 0$$
$$X_m = \frac{H_m^{(2)'}(k_\rho\rho)}{H_m^{(2)}(k_\rho\rho)}, \qquad Y_m = \frac{J'_m(k'_\rho\rho)}{J_m(k'_\rho\rho)} \tag{3.14}$$

The obvious singularities are the poles in the matrix components, i.e. k_z=$\pm k$ and k_z=$\pm k'$, corresponding to the TEM contribution of plane wave propagation in free space and to eigenmodes of propagation in the lossy medium, respectively.

To avoid the singularities in the line-source solution, the same complex contour as the one already described in Chapter 2 is chosen (Fig. 3.5). So that, the scattered electric field $\mathbf{E}^{sp}$ is obtained by numerical integrating of $\mathbf{E}^{sl}$:

$$E_z^{sP} = \frac{1}{2\pi} \int_{\infty}^{\infty} \mathrm{d}k_z \sum_{m=-M}^{M} e^{jm\phi} e^{-jk_z z} \times \begin{cases} A_m J_m(k'_\rho \rho) & a \geq \rho \\ A'_m H_m^{(2)}(k_\rho \rho) & \rho \geq a \end{cases} \tag{3.15}$$

The same integration technique is also applied to the incident fields radiated from the line source ($\mathbf{E}^{il}$) to give the point source incident fields ($\mathbf{E}^{ip}$). On the other hand, an exact analytical expression of $\mathbf{E}^{ip}$ is available, by using the projection of the fields as mentioned in (3.16) and (3.17) [47]. We name the first approach "numerical" (in view of the computation of the series and integrals) and the second one "analytical".

$$E_{\rho 1}^{iP} = E_{\rho 2}^{iP} \cos\gamma - E_{\phi 2}^{iP} \sin\theta \tag{3.16}$$

$$E_{\phi 1}^{iP} = E_{\rho 2}^{iP} \sin\gamma + E_{\phi 2}^{iP} \cos\theta \tag{3.17}$$

indices 1 and 2 indicate that the origin of the system of coordinates is set to the "center of the removed cylinder" and to the "point source", respectively (Fig. 3.2). γ is the angle between the radial unit vectors ($\hat{\rho}_1 \cdot \hat{\rho}_2$) and θ is the angle between the tangential unit vectors ($\hat{\phi}_1 \cdot \hat{\phi}_2$), ($\gamma$=$\theta$=$\phi_2$-$\phi$).

Fig. 3.6 shows the variation of the radial and tangential components of the incident electric fields (E_ρ^{ip} and E_ϕ^{ip}) at (ρ=15 cm, ϕ, z=0) while the point source is located at (ρ_s=18 cm, ϕ, z=0). The plain and marked curves are associated respectively with the analytical and the numerical approaches, at 0.915 GHz and 2.45 GHz. Except for the observation points located very close to the point source, i.e. $\phi \cong 0$, numerical and analytical approaches provide extremely close results. E_z^{iP} in Fig. 3.6 equals to zero (-∞ in dB scale), because radially polarized sources cannot create any electric field in the z direction at the height of the source. Fig. 3.7 shows the scattered fields E^{sp} on the body-air interface, due to a radially polarized point source at (ρ_s=18 cm, ϕ=0, z=0) at f_1=0.915 GHz and f_2=2.45 GHz.

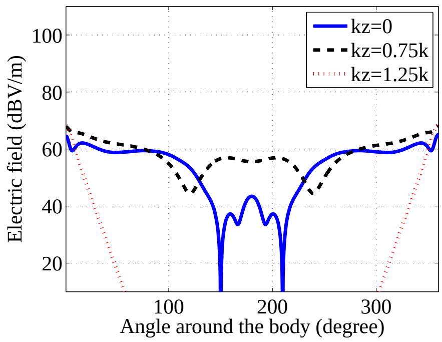

(a)

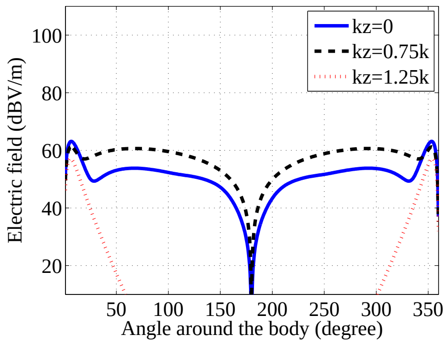

(b)

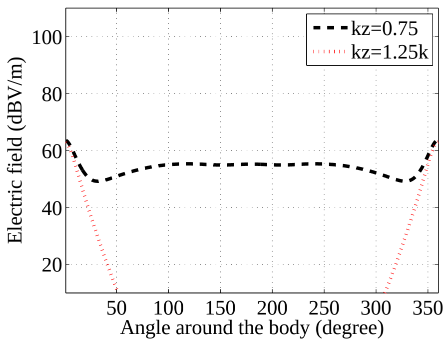

(c)

Figure 3.4 (a) ρ-component (E_{ρ}^{sl}), (b) ϕ-component (E_{ϕ}^{sl}), (c) z-component (E_{z}^{sl}) of the scattered electric fields, due to a line source at ρ_s=18 cm and along the z-direction with radial polarization, in the vicinity of a lossy cylinder with diameter of d=30 cm, and permittivity of ϵ_r=47-16.22j. The observation point is located at ρ=15 cm and the frequency is f=2.45 GHz.

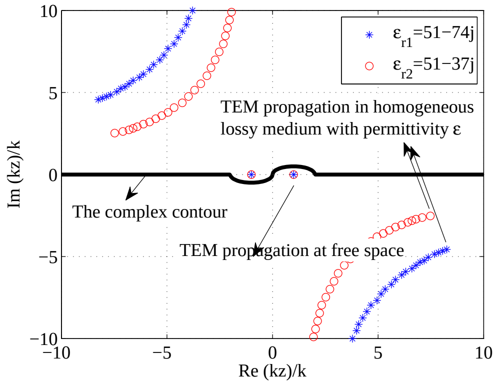

Figure 3.5 The eigenvalues of the normalized axial wave vector $\frac{k_z}{k}$ for two lossy cylinders with ϵ_{r1}=51-37j (permittivity of human body at f= 0.915 GHz) and ϵ_{r2}=51-74j. The complex contour avoids the singularities.

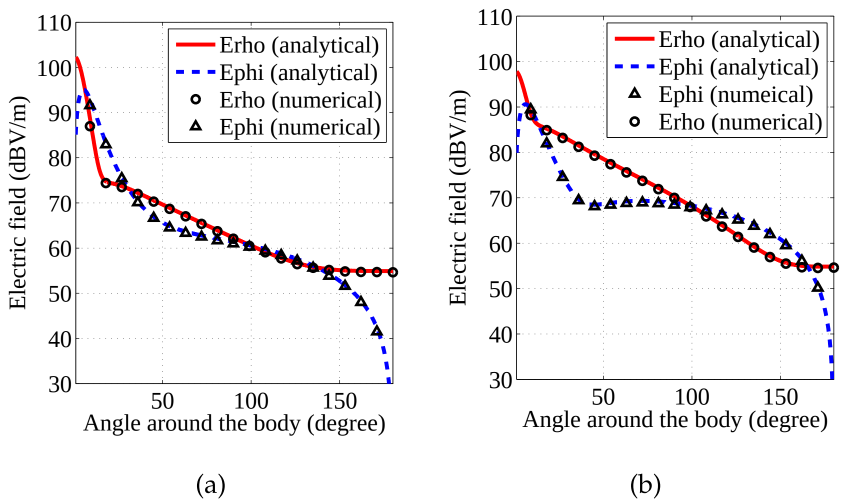

Figure 3.6 ρ and ϕ components of the incident electric field (E_ρ^{ip} and E_ϕ^{ip}) due to a point source normal to the body at (a) 0.915 GHz and (b) 2.45 GHz. Both source and observation points are at z=0, ρ=15 cm, and ρ_s=18 cm (d_s=3 cm).

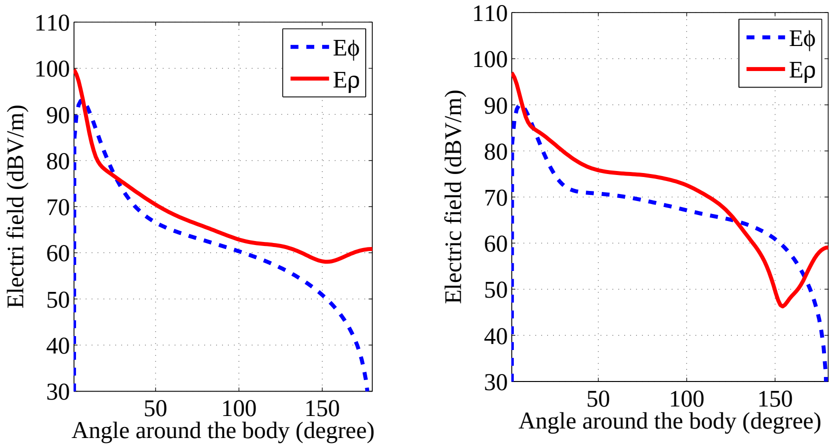

(a) (b)

Figure 3.7 ρ and ϕ components of the scattered electric field (E_{ρ}^{sP} and E_{ϕ}^{sp}) due to a radially polarized point source located at ρ_s=18 cm at (a) 0.915 GHz (ϵ_r=51-37.47j) and (b) 2.45 GHz (ϵ_r=47-16.22j). Both source and observation points are located in the XY plane at z=0.

3.3 Using the MoM for modeling a dipole antenna normal to the cylinder

In this section we integrate the cylinder Green's function, into an integral-equation formulation. The methodology is described in Section 3.3.1. The cylinder-dipole interactions and the effect of the cylinder on the matching and current of the antenna are given in Sections 3.3.2 and 3.3.3. The transmittances between two radially-polarized dipole antennas with and without the body are studied; measurement results and *CST Microwave Studio®* results have been used to validate the proposed model (Section 3.3.5).

3.3.1 General approach

First, a code based on the Method of Moments (MoM) is developed to calculate the current and input impedance of a dipole antenna in free space [74]. To model the mutual coupling from the lossy cylinder (Fig. 3.8), we should consider the fields scattered by the cylinder in the MoM code. By using the Pocklington's integral equation [74], we express the boundary condition on the surface of the dipole, in terms of total tangential electric fields, to find the current on the axis of the wire (along $\hat{\rho}$).

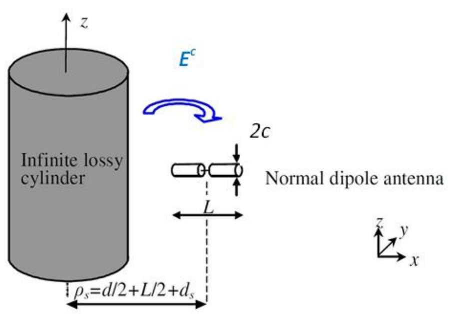

Figure 3.8 Radially-polarized dipole antenna located close to the infinite lossy cylinder with diameter of d. $\mathbf{E}^c$ is the field radiated by a basis function and then scattered from the body.

$$\int (\mathbf{E}^f(\rho,\rho_s) + \mathbf{E}^c(\rho,\rho_s))\mathbf{J}^t \mathrm{d}\rho = \begin{cases} -V & \text{if } \mathbf{J}^t \text{ overlaps the source} \\ 0 & \text{elsewhere} \end{cases} \quad (3.18)$$

where $\mathbf{J}^t$ is a testing function with triangular shape located on the outer part of the dipole antenna, and V is the excitation voltage. The total electric fields, whose tangential components are equal to zero on the outer part of the dipole, are integrated over the testing function. The scattered field $\mathbf{E}^c$ is the field radiated by the basis function $\mathbf{J}^b$ and then scattered from the body. The cylinder has the same characteristics as in Section 3.2. $\mathbf{E}^f$ is the field radiated from the basis function in free space (without a scatterer); it is derived from the vector potential:

$$\mathbf{E}^f(\rho,\rho_s) = \frac{\eta}{jk}(k^2\mathbf{A}_\rho + \nabla_x\nabla\cdot\mathbf{A}_\rho) \quad (3.19)$$

where η is the wave impedance, k is the wavenumber, and $\mathbf{A}_\rho$ is the vector potential, which is obtained from:

$$\mathbf{A}_\rho = \int \mathbf{J}^b g \mathrm{d}\rho_s \quad (3.20)$$

where g is the scalar Green's function $g = e^{-jkR}/4\pi R$, with $R = \sqrt{(\rho-\rho_s)^2 + c^2}$, if basis and testing functions are located on the same wire.

We discretize the current of the dipole as $\mathbf{J} \cong \sum_{j=1}^{M} x_j \mathbf{J}_j^b$ to obtain the MoM system of equations $Zx = V$, where x_j are unknowns and V_j are zero everywhere, except for the entry corresponding to the testing function that overlaps the delta-gap source, $j = (M+1)/2$. An element of the MoM impedance matrix can be written as $Z_{i,j} = \int (\mathbf{E}_j^f + \mathbf{E}_j^c)\cdot\mathbf{J}_i^t$, corresponding to basis function $\mathbf{J}_j^b$ and testing function $\mathbf{J}_i^t$.

The electric field $\mathbf{E}^c$ due to basis function $\mathbf{J}_j^b$ and scattered by the cylinder is obtained from the appropriate component of the dyadic Green's function $\mathbf{G}^b$ see B.6:

$$\mathbf{E}_j^c(\rho) = \int_{d/2+d_s}^{d/2+d_s+L} \mathbf{G}(\rho,\rho_s)\mathbf{J}_j^b(\rho_s)\mathrm{d}\rho_s \quad (3.21)$$

where $\mathbf{J}_j^b$ is a triangular basis function. The current distribution along the dipole antenna is described with M=33 basis functions. Integration (3.21) is carried out by computing $G(\rho, \rho_s)$ through mere interpolation from a precomputed table G^b. Since G only describes the scattered field, it is a very smooth function of ρ and ρ_s. Therefore, a tabulation with very few points along ρ and ρ_s is sufficient:

$$\mathbf{G}^b = \begin{bmatrix} G^b_{1,1} & G^b_{1,2} & \cdots & G^b_{1,NS} \\ G^b_{2,1} & \ddots & & \\ \vdots & & \ddots & \vdots \\ G^b_{NO,1} & & \cdots & G^b_{NO,NS} \end{bmatrix}_{NO,NS} \tag{3.22}$$

where NO and NS are the number of observation and source points, respectively. In this work $NO = NS = N = 5$ and we use the method described in Section 3.2 to find the matrix values and to fill in the Green's function matrix. For any observation point or source point, a 2D interpolation has been used to find the values at intermediate positions from the matrix G^b. This is possible because the fields scattered from the cylinder form a smooth function.

For an isolated dipole antenna in free space, $\mathbf{E}^b$ is equal to zero and for the case of an infinite lossy cylinder as a scatterer, $\mathbf{E}^b$ is tabulated. It is shown in Fig. 3.7, for the case of d=30 cm, ρ=15 cm, and ρ_s=18 cm. In [25], the simpler case of a vertical dipole antenna, instead of a normal one, is studied. In that case, $\mathbf{G}^b$ depends only on the difference between ρ and ρ_s, hence it is represented by a $1 \times N$ matrix.

3.3.2 Input impedance of the radially-polarized dipole

Finding the minimum distance between a matched antenna and the body is one of the goals when investigating the body-antenna interactions [75]. Although a zero distance is practically the most convenient case, it leads strong antenna mismatch, especially for vertically-polarized antennas.

The scattered fields are smooth functions, decaying away from the cylinder and not many points of the cylinder Green's function need to be calculated. If we set that resolution to 1 cm (i.e. about $\lambda/10$ or 5 points on antenna), G^b needs 3.7 minutes to be calculated with an Intel CPU 650 at 3.20 GHz processor. A MoM code can accordingly use the tabulated Green's function to simulate quickly the transmittance between any pair of antennas. In our study, only 0.7 seconds are needed to obtain S_{21} for the dipoles, which is much faster than with FDTD or improved FDTD methods. For comparison, in [15], an improved FDTD simulation leads to a 376 minutes for computing the transmittance between two on-body cavity-backed slot antennas at 5.2 GHz (simulations performed on Intel Xeon X5670 at 2.93 GHz processor). We should note however the higher frequency for the example in [15] (factor close to 2) and the much finer level of geometrical detail allowed by the FDTD approach.

Fig. 3.9 shows several columns of the Green's function matrix of (3.22), i.e. scattered fields versus the distance from the body, due to the radially-polarized point sources located at different positions (ρ_s=15, 18, and 21 cm, ϕ=0, z=0). It shows how scattered fields are decreasing away from the body. The results for the tangentially-polarized point sources can be found in [25]. The exact analytical scattered fields from a normal PEC plate are shown in Fig. 3.9 with the marked lines. For the same source-scatterer distance d_s, the PEC plate reflects the wave stronger than the body, which has a limited conductivity. However, this superiority is decreasing when getting close to the interface, either with the point source or with the observation point, since the curvature of the cylinder is locally less visible.

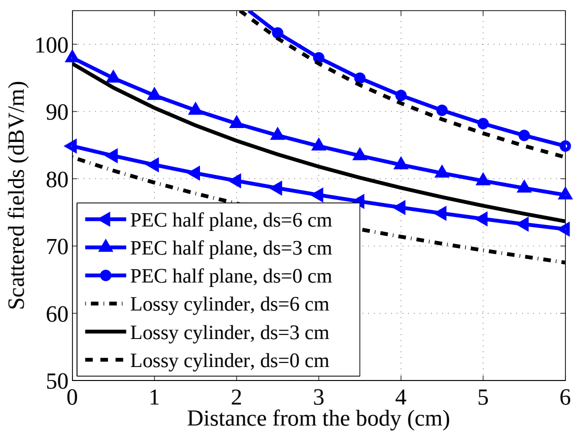

Figure 3.9 ρ components of the numerical scattered fields (E_ρ^{sp}) from an infinitely lossy cylinder and analytical scattered fields from perfectly conducting plate. Point sources, with strength of 1 $A.m.$, are located at different distances from the scatterers d_s=0, 3, and 6 cm.

The type of scatterer, the dipole-scatterer distance b and the dipole orientation are the external parameters that affect the input impedance of the antenna. The input impedance of an ultra-thin half-wavelength dipole polarized perpendicular (tangential) to the scatterer gets the minimum (maximum) influences from the scatterer (Fig. 3.10). Strong changes of the input impedance of the radially-polarized dipoles on the cylinder have been observed for small values of b. By increasing b, the values of the resistance and reactance will approach the corresponding values for the isolated element, Z_m=77.9+46j. For the same source-scatterer distance d_s=b, a PEC plate can reflect the wave stronger than the body, which has a limited conductivity.

Fig. 3.11 illustrates the effects of the dipole length and position on its reflection coefficient S_{11} when it is radially placed next to a scatterer, in the form of contour plots of S_{11} versus dipole-scatterer distance b and dipole length L. The dipole is very thin (2c=1.5 μm, left) or in a more applicable range (2c=1.5 mm, right). The gray regions of Fig. 3.11 shows the dipole dimensions that can keep the antenna matched to a 50 Ω generator with $S_{11} \leq$ -10 dB. For dipoles far from the scatterer (large b), the acceptable range of L to have the antenna matched converges towards corresponding values of a sole dipole in free space, i.e. 0.48< L/λ <0.496 and 0.43< L/λ <0.484 for ultra-thin and thin dipoles, respectively.

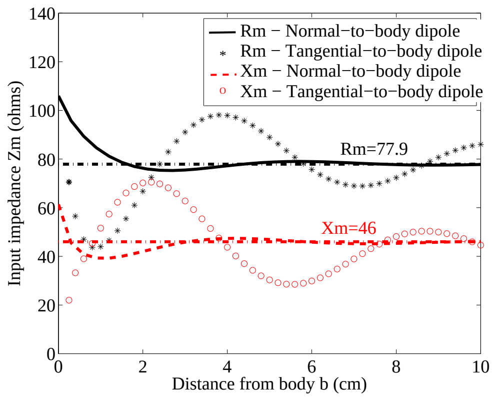

Figure 3.10 Input impedance ($Z_m = R_m + jX_m$) of the ultra-thin half-wavelength dipole antenna (2c=1.5 μm) at 2.45 GHz, when the antenna orientation is parallel or normal to the infinite lossy cylinder with d=30cm and ϵ_r=47-j16.22.

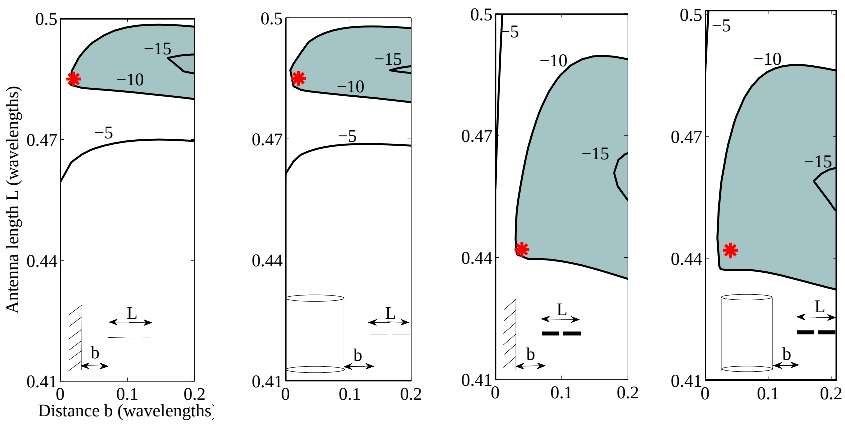

(a) (b) (c) (d)

Figure 3.11 Dipole reflection coefficient S_{11} in dB, versus the antenna length L and the dipole-scatterer distance b, with the diameters of $2c$=1.5 mm (thin) and $2c$=1.5 μm (ultra-thin). At f=2.45 GHz, dipoles are radially placed close to the PEC plate or the lossy cylinder with ϵ_r=47-16.22j. The stars show the appropriate antenna lengths L at minimum b in the acceptable matching regions (S_{11} less than -10 dB, gray surfaces).

Decreasing L causes a rapid decrease in the dipole reactance, thereby a good impedance matching of the dipole can be achieved by cutting the dipole ends a little. The stars in Fig. 3.11 show the appropriate L for a minimum b of a matched dipole; corresponding values for the thin dipole equal to L=0.442λ=54.1 mm and b=0.04λ=4.9 mm. The input impedance of the mentioned dipole in free space is obtained as Z_{MOM}=59.6-23.3j Ω (S_{11}=-13 dB), which is in good agreement with the results from the method proposed in [76,77] with *CST Microwave Studio*®, Z_{CST}=61.1-23.1j Ω.

3.3.3 Current on the dipoles

The scattered fields from the PEC plate or the lossy cylinder affect the dipole currents differently; in both cases, more strongly when the dipole and the scatterer are in parallel (tangentially polarized dipoles) and/or close situations. In the parallel situations, increasing the conductivity of the lossy cylinder, or approaching the dipole to the scatterer, causes stronger scattered fields and thereby leads to an increase in the total current on the dipole antenna, with similar (close to cosine) shapes of the antenna currents.

We used the MoM code to model the current on the normal-to-cylinder dipoles with the optimum size, as calculated in Section 3.3.2, and for f=2.45 GHz. A generator with the Thevenin equivalent voltage of V_{th}=1 V and the Thevenin equivalent impedance of R_{th}=50 Ω feeds the dipole at its center. The dipole current I_1 has a maximum of I_{1max}=8.2 mA almost at the center.

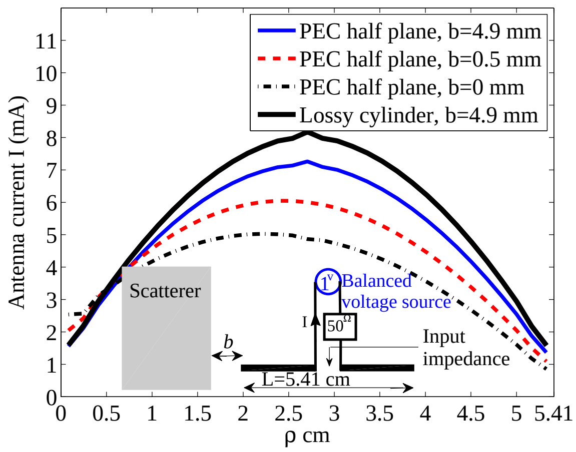

Figure 3.12 MoM results for the antenna currents for different distances from the scatterer b. The thin dipole has a diameter of $2c$=1.5 mm and a length of L=54.1 mm. The dipole is fed at its center by a generator.

Approaching the dipole to the scatterer makes the antenna current asymmetrical, with a current that tends to increase on the arm closer to the scatterer, as shown in Fig. 3.12. Besides, the increase in the average current amplitude helps to maximize the radiating waves on the cylinder-air interface. They travel around the cylinder and increase the field in the back of the cylinder in the shadow region. The closer the antenna is located to the cylinder, the higher radiating waves are produced around the cylinder. As an example, moving the radially-polarized point source 4 cm apart from the cylinder (ρ_s=22 cm), decreases the normal-to-cylinder electric field up to 4 dB around the cylinder inside the shadow region. It should be mentioned that the final goal is maximizing S_{21} around the body, while the dipole reflection coefficient is kept at an acceptable level.

Using the MoM approach described in Section 3.2.1, we calculate the load currents of two radially-polarized dipoles, $I_{excited}$ and $I_{coupled}$, placed close to the cylinder (ρ_s=b+$L/2$+$d/2$, ϕ=0, z=0) and (ρ_s=b+$L/2$+$d/2$, ϕ_c=0, z=0), respectively, as shown in the inset of Fig. 3.13. In this figure, the thick solid line represents the dipole current considering the mutual coupling with the cylinder and the thin solid line represents the dipole port current in the same positions but in the free space, which is verified by NEC simulation results [78]. The length of the antennas and their distances from the cylinder remain the same for all simulations. The active dipole is connected at its center to a generator with a Thevenin equivalent voltage of V_{th}=1 V and a series impedance of R_{th}=50 Ω, while the passive dipole is connected to a 50 Ω load. An increase of angular distance ϕ_c causes a decrease in the mutual coupling between two antennas, with an oscillatory behavior probably through multiple-scattering on the cylinder. However, these oscillations are stronger in the presence of the cylinder.

In the range $0<\phi_c<34.5°$, where a direct path is present between the antenna feeding points, the waves reflected from the cylinder produce a relatively strong coupling to the passive antenna. The maximum peak of $I_{coupled}$ at ϕ_c=28° has been made by the in-phase superposition of reflected and direct waves. In the range of $44°<\phi_c<180°$, there is no direct path between any two points of the dipoles, and waves traveling around the cylinder are responsible for the observed values of $I_{coupled}$.

3.3.4 Total fields due to the radially-polarized dipole

We consider the dipole antenna with the optimum size and distance from body, fed at its center by a source with voltage of V_{th}=1 V and impedance of

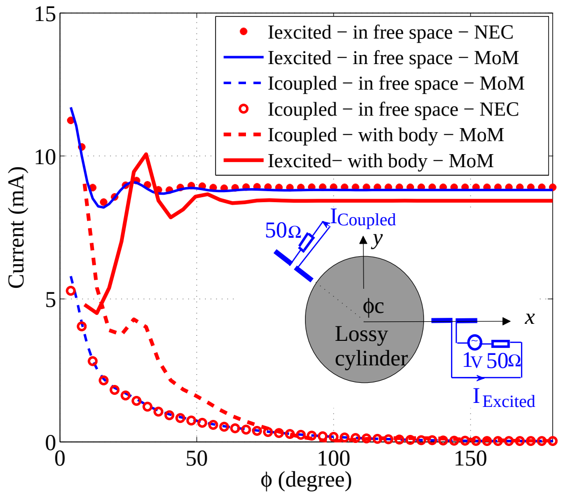

Figure 3.13 Current magnitude of two radially-polarized on-body antennas versus the angle ϕ_c, with and without the presence of the body, at f=2.45 GHz. Dipoles diameters of $2c$=1.5 mm and lengths of L=54.1 mm. Body diameter: d=30 cm.

R_{th}=50 Ω. Fig. 3.14 shows the top view of the electric field magnitude from the dipole antenna in free space (E^i). The position of the body is shown with the dashed circle. To find which portion of the incident field is normal to the body (E^i_ρ), we should project E^i of Fig. 3.14a onto the ρ direction of another coordinate system with origin at the center of the dashed circle (Fig. 3.14b). Applying this projection to the electric field, changes the direction of propagation from X to ϕ, as can be seen in the contours of Figs. 3.14a and 3.14b. Human body, with very high lossy tissues, can almost work like a PEC cylinder and eliminates the tangential component of the field E^i_ϕ on its surface and keep only normal component E^i_ρ. So, E^i_ρ gives an intuition how the propagation would be in presence of the human body.

The dipole antenna in the vicinity of a finite lossy cylinder, with a hight of H=125 cm and a diameter of d=30 cm, consisting of 86 million mesh cells, is modeled in *CST Microwave Studio*®, in a cooperation with *Antennas Research Group* of *University of London* [26]. In Fig. 3.15, the total field, i.e. the incident field of Fig. 3.14b plus the scattered field from the cylindrical body, has almost the same type of propagation behavior along ϕ in front of the body, except of the excited surface currents attached to the body-air interface. Unlike the incident field of Fig. 3.14b, interaction of the excited surface waves (clockwise and counter clockwise) creates a standing wave which can be seen explicitly at the back of the body, where we have a poor incident electric field. Since the displacement fields D_ρ=ϵE_ρ must be continuous across the dielectric interface, there is a discontinuity of E_ρ at ρ=$d/2$. E_ϕ with a continuous distribution across the dielectric interface at ρ=$d/2$, are shown in Fig. 3.15, where the lossy body degrade sharply E_ϕ.

Fig. 3.16 shows how the normal component of the field varies on the body surface (ρ=$d^+/2$), with and without the presence of the body, through plain and dashed lines, respectively. Normal electric fields obtained with the cylindrical-object Green's functions (plain curve) are in a very good agreement with those obtained from *CST Microwave Studio*® (circled curve) [26]. Note that all the figures contain absolute values, no normalization is applied, and the electric field strengths are calculated in dBV/m. We have used a probe to measure E_ρ around the body. Since the input impedance of the probe is sensitive to the fields reflected by the scatterers, we have considered the antenna in the close vicinity of human body, upon designing the matching network. To have the probe better matched to a 50-Ω generator in the measurement, we should locate the probe very close to the body, e.g. by means of the mechanical support that will be explained in Section 3.3.5. More details about the design of the probe is given in Appendix D.

For the normal electric fields in Fig. 3.16, three different trends of on-body propagation are noticeable:

- ϕ <10°: A linear and rapid attenuation of 6.59 dB/cm in free space and 8 dB/cm with the presence of the body. This field attenuation rate is increasing by moving the antenna farther from the body. For a given point on the body surface, little change in the antenna-body distance d_s causes a rapid attenuation of the field strength at this region, compared with the field attenuations in other regions.
- 10°< ϕ <120°: Linear attenuation of 0.86 dB/cm in free space and 1.14 dB/cm in the presence of the body. In this range, the lossy cylinder (human body) guides the fields to a certain extent, which can significantly increase the field for observation points on the back side of the

body. In fact, diffraction around the surface of the body supports the transmittance. It makes the normal-normal configuration highly favorable to on-body communications. Inside the body, the field propagates through the lossy medium and it decays exponentially with the distance with a ratio of 5.19 dB/cm. The attenuation ratio inside the body is a function of $\mathrm{Im}(\sqrt{\epsilon})$.

- $120° < \phi < 180°$: With noticeable oscillation in the presence of the body, shows that the interference between the waves traveling clockwise and counter-clockwise produces a standing wave in the backside of the body.

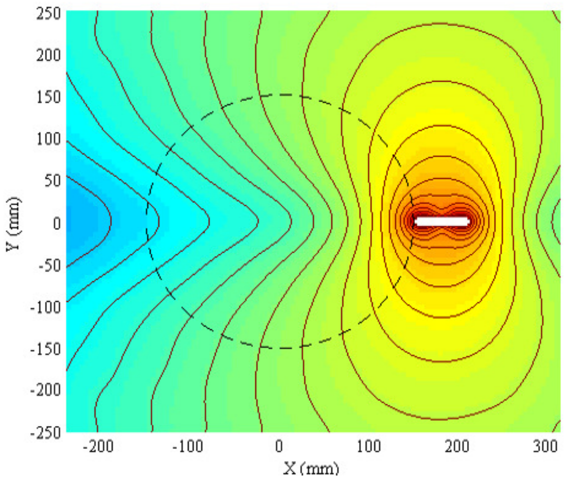

(a)

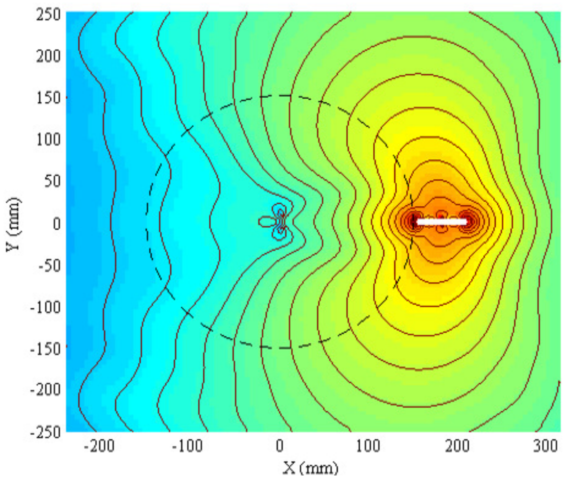

(b)

Figure 3.14 (a) Top view of the electrical field distribution from the dipole antenna, in free space E^i. (The dashed line shows the place that the body will be added). (b) Top view of the incident electrical field distribution normal to the excluded body E^i. The body is shown with the dashed line. [26]

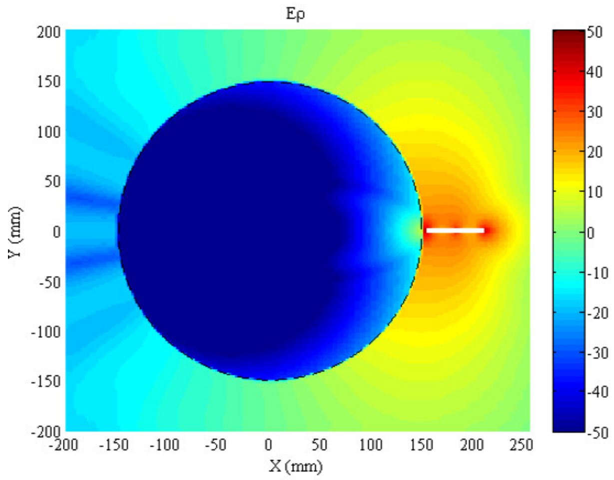

(a)

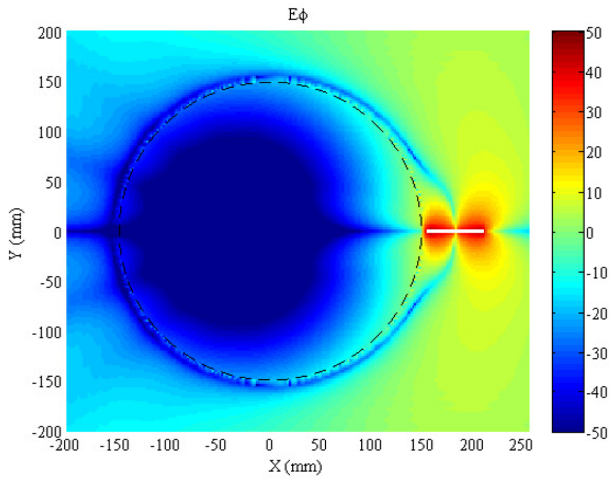

(b)

Figure 3.15 Top view of the electrical field distribution (a) normal to the (dashed line) body E_ρ and (b) tangential to the body E_ϕ, in its close vicinity to the dipole antenna. Standing waves at the left side of the figure (back of the body) shows the interaction between two waves propagating in opposite directions [26].

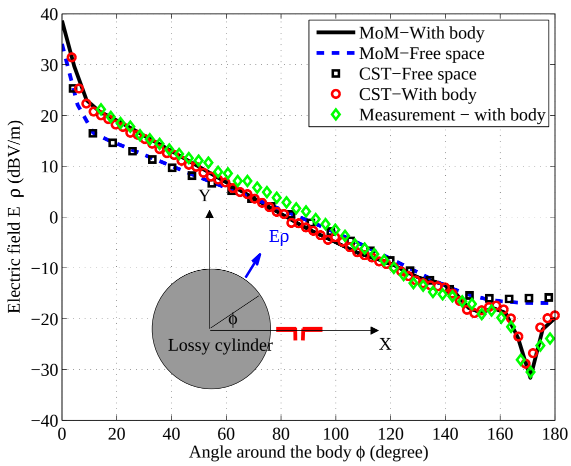

Figure 3.16 Electric field E_ρ around the body (ρ=$d^+/2$, ϕ, z=0), due to the dipole normal to the body, with a center at (ρ_s=$d/2$+d_s+$L/2$, ϕ_s=0, z=0). Cylinder length H in *CST Microwave Studio*® simulations is equal to 125 cm and in MoM simulations is equal to infinity. [26].

3.3.5 Measurements and model validation

To be able to verify the proposed model with measurement results, we calculate the transmittance between two radially-polarized on-body dipoles by means of the developed MoM code. Consider a two-port network of dipole antennas, one is connected to a generator with the Thevenin equivalent voltage of 1 V and the Thevenin equivalent impedance of 50 Ω and the other one is connected to a 50 Ω matched line (Fig. 3.17). The load currents of "dipole 1" and "dipole 2", in center of the dipoles, are I_1 and I_2, respectively. If we have "M" basis functions for each dipole, those currents correspond to $x_{(M+1)/2}$ and $x_{(3M+1)/2}$. In Section 3.3.1, the MoM system of equations is defined as $Zx = V$, where V is a vector with zero everywhere, except for entry of $(M+1)/2$. To find the mutual impedances between two ports, and afterwards the S-parameters, we multiply the inverse of the MoM impedance matrix $Z^{-1} = Y$ (MoM admittance matrix), to both sides of the MoM equations to find the unknown currents, $x = YV$. Thereby, the loading currents I_1 and I_2 would be equal to $x_{(M+1)/2,1} = y_{(M+1)/2,(M+1)/2}$ and $x_{(3M+1)/2,1} = y_{(3M+1)/2,(M+1)/2}$. Knowing the array admittance matrix elements $(y_{11}, y_{21}, y_{21}, y_{22})$, we find the array impedance matrix elements $(z_{11}, z_{21}, z_{21}, z_{22})$ and then we use it in ((3.23)) [79], to find the S-parameters.

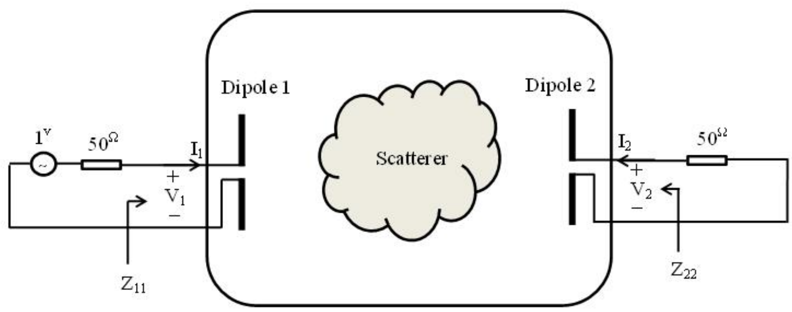

Figure 3.17 Two-port network of dipoles in the presence of the scatterer.

$$S = \begin{bmatrix} \frac{(z_{11}-Z_0)(z_{22}+Z_0)-z_{12}z_{21}}{D_z} & \frac{2z_{12}Z_0}{D_z} \\ \frac{2z_{21}Z_0}{D_z} & \frac{(z_{11}+Z_0)(z_{22}-Z_0)-z_{12}z_{21}}{D_z} \end{bmatrix} \quad (3.23)$$

where $D_z = (z_{11} + Z_0)(z_{22} + Z_0)\text{-}z_{12}z_{21}$.

The configurations of the dipoles around the body and the defined parameters $I_{coupled}$, $I_{excited}$, and ϕ_c, remain the same as described in Section 3.3.3. The mutual inductance matrix of dipoles is calculated to give the S-parameter matrix. The solid curves in Fig. 3.18 show the transmittances of dipoles versus the separation angle ϕ_c, as calculated with the MoM, for two cases: (3.18.a) in free space and (3.18.b) in presence of the body. The differences between transmittances, shown in Figs. 3.18(a) and 3.18(b), show the contribution of the surface current on the body (extinction theorem).

Afterwards, the same structure, but with a finite cylinder (h=125 cm, d=30 cm), is modeled with *CST Microwave Studio*® and the results are shown with the dashed lines in Fig. 3.18. The electric field distribution of two dipoles around the body obtained from CST simulations is also shown in Fig. 3.19. This figure shows how the electric-field waves, radiated from the first dipole, travel around the body to be absorbed by the second dipole. An important fraction of power is also absorbed in tissues near the active antenna.

The transmittances obtained with the cylindrical-object Green's functions (solid curves) are in very good agreement with those obtained from CST (dashed curves). Note that all the figures contain absolute values, no normalization is applied. While two antennas are close together ($0<\phi_c<30°$), the direct path is dominant and the scatterer does not have a significant effect on S_{21}. In the range $30°<\phi_c<180°$, there is no direct path between the dipole tips and the lossy cylinder interface supports the radiating waves. In this range, the attenuation rate of the transmittance in presence of the body, S_{21}=0.93 dB/cm, is close to that in free space, which is S_{21}=0.82 dB/cm. This makes the normal-normal configuration highly favorable to on-body communications. The radially-polarized point sources [75] and dipoles [26] create the standing waves at the back of the lossy cylinder and thereby cause a strong variation of the field. The transmittance between two dipoles gets also affected by this interference of clockwise and counter-clockwise waves. The variation of S_{21} can be clearly seen in the right side of Fig. 3.18-b.

To validate the simulation results, we performed a set of measurements in an anechoic chamber by placing two dipoles (with the optimum size of L=54.1 mm and $2c$=1.5 mm, calculated in Section 3.3.2) on the trunk surface of a volunteer. During the measurements, he locked his hands behind the head with a standing posture, while his abdomen circumference was approximately fixed and equal to that of the lossy cylinder, πd=94.2 cm. On-body dipoles were connected to an $Agilent\ N5242A\ VNA$ using 6 meter low-loss coaxial cables. A BALUN transition has been designed and fabricated to connect the dipoles to the coaxial lines (details are discussed in Chapter 5). On-body measurement results might include some errors because of the breathing, unwanted movements of the body, or unwanted changes in the direction of the normal-to-body dipole antennas. To overcome the mentioned problems, solid foam with the shape of the body trunk is fabricated and the foam is located on the body abdomen (Fig. 3.20). It contains a series of holes with diameters of 1.5 mm, at 1 cm distance from each other, in order to fix the distance and direction of the wired antennas with respect to the body.

Fig. 3.18-b shows a very good agreement between the measurement results (circled line) and the lossy-cylinder simulation results (plain curves and dashed curves). However, little differences between the simulation and measurement results appear in the range of 120°<ϕ<165°. This is perhaps due to the non-circular shape of the human body in this part [44, 45]. The variation of transmittances in the back of the body (140°<ϕ<180°), because of interference between opposite traveling waves, can be explicitly seen in both S_{21} results. With or without the presence of the body, S_{21} in the range of 140°<ϕ<180° has very low values, from -45dB to -65dB, so that the simulation and the measurement are carried out with special considerations; the measurement is performed with a VNA that supports a high dynamic range. With *CST Microwave Studio*®, the simulation bounding box, imposing the far field boundary conditions, is made large enough (otherwise waves reflected from the box have an impact). The experimental results validate the practical points addressed by our model, namely the sharp decay of S_{21} with an average rate of 2.86 dB/cm for 0<ϕ<10°, the linear decay of S_{21} with a rate of 0.93 dB/cm around the body, and standing-wave pattern, on the back-side of S_{21}, starting

from ϕ=180° and disappearing around ϕ=120°. In [80], Hall et al. give data for an around-the-torso measurement, using two quarter-wavelength monopoles antennas that are mounted normal to body on the waist. The rate of the attenuation, obtained from a linear fit for distances of about 10 to 50 cm, are almost 1 dB/cm.

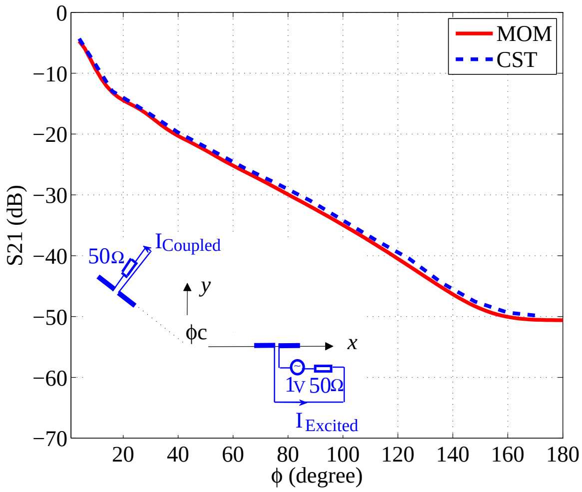

(a)

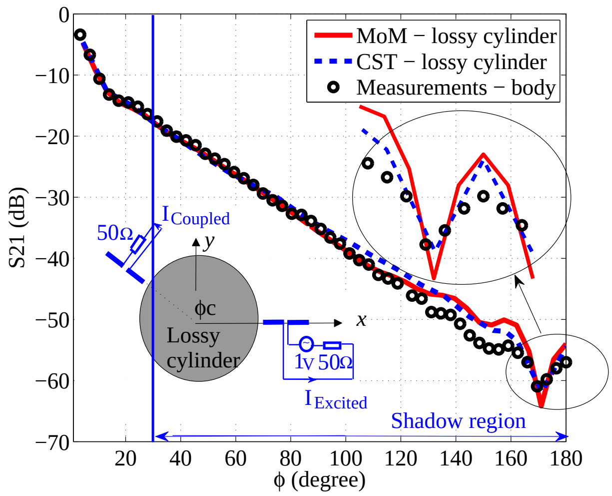

(b)

Figure 3.18 Transmittances of two radially-polarized on-body dipoles, achieved at f=2.45 GHz according to MoM, CST, and measurement, (a) in free space and (b) in presence of the lossy cylinder (body).

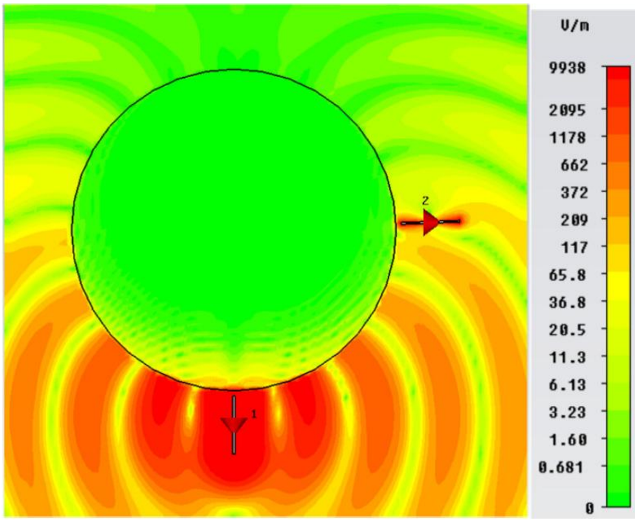

Figure 3.19 Top view of the electrical field distributions around the lossy cylinder, obtained from CST simulations. Dipoles number 1 and 2 are carrying $I_{Excited}$ and $I_{Coupled}$, respectively.

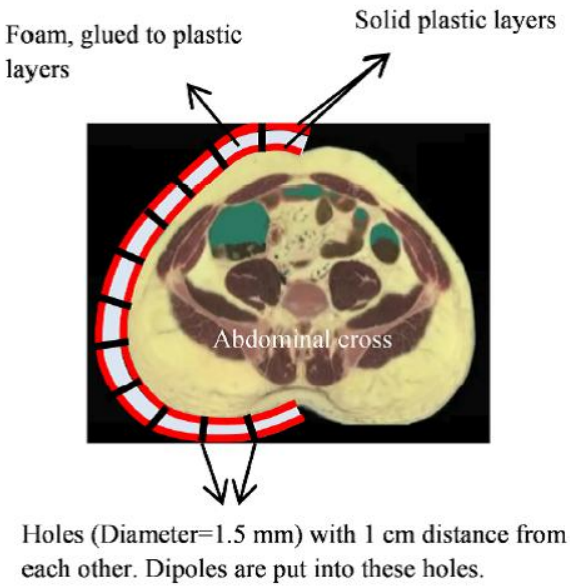

Figure 3.20 Abdominal cross section of the human body [3]. A solid foam mounted on the body trunk to perform the measurement with the minimum error.

3.4 Conclusions and perspectives

An analytical formulation has been proposed for the field distributions around an infinite lossy cylinder due to a radially-polarized point source. The fields scattered from the cylinder (cylinder Green's function) have been compared with the fields scattered from the perfectly conducting plate, for different positions of the source and observation points. Exploiting this Green's function, a MoM code has been developed to calculate the excited and coupled currents of two dipoles placed close and normal to a cylinder that represents the body. Respecting the body-antenna mutual interactions, we have optimized the length and the distance to the body of a dipole, in order to excite the maximum radiating waves around the body, while the antenna keeps its acceptable impedance matching to a 50 Ω generator. The current and input impedance of the radially-polarized dipole have been explored in presence of the body and it is shown how a high-conductive scatterer in the close vicinity of the dipole can make the antenna current asymmetrical.

The analytical-numerical results provide the pathloss trends around the body from modeling the canonical dipole-dipole transmittance on the body. The proposed model has been validated through comparisons with results from commercial simulators and experiments. A very good agreement has been achieved.

The radiating waves attached to the body-air interface are associated to the dominant path of propagation in the range of $30^\circ<\phi<180^\circ$ around the body, while there is no direct path between the on-body dipoles. In this range, the attenuation rate of the transmittance in presence of the body, S_{21}=0.93 dB/cm, is close to the one in free space, which is S_{21}=0.82 dB/cm. Unlike the cases where the dipole is placed parallel to the body, the attached waves traveling around the body maintain a high transmittance between normal-to-body antennas. The interference between these waves in the back of the body ($150^\circ<\phi<210^\circ$) can produce a strong variation of the antenna transmittance.

Analysis of Power Absorption in Cylindrical Bodies

4

In Chapters 2 and 3, the cylindrical wave decomposition has been exploited to derive the field harmonics outside of an infinite lossy cylinder, exposed to the near field of an arbitrary-polarized point source. In this chapter, a Parseval type transform is applied to cylindrical field harmonics to find the power crossing the surface of the cylinder. The proposed model has been validated through comparisons with results from CST Microwave Studio, where the absorbed power is calculated from the efficiency of a short-dipole antenna located close to a finite lossy cylinder. When the cylinder is oriented along the $\hat{z}$ axis in the near-field zone of the point source, the normal-to-body polarization interestingly causes the maximum power absorption in the cylinder with respect to other polarizations. That is due to the surface waves launched along and around the cylinder.

4.1 Introduction

For antennas placed inside or outside a lossy medium, it is important to find the mechanisms of power absorption. The RF power dissipated in lossy media, e.g. in MRI scans or in close proximity of mobile phones to human body, are widely analyzed by popular computational methods like the FDTD method [81–85]. However, these methods are time consuming, especially for electrically-large objects. On the other hand, analytical modeling of the simple structures like cylinders [2, 29] or spheres [84, 86] can be faster and allow the physical interpretation of phenomena at hand. The near-field interaction of the source and scatterer should be modeled by considering the coupling in the absorbed power analysis. This modeling has been done for the spherical case by using the Mie series solution [87,88], but - to our best knowledge - not for cylindrical structures.

A 2-D analytical modeling of the power absorbed by an *M*-layer circular dielectric cylinder is presented in [89]. A volume integral equation approach has been applied in [90] to calculate the field induced in a spheroidal body when it is exposed to the near field of a small loop antenna. The absorbed power has been accordingly obtained by integrating over the volume. The effects of the loop orientations on the absorbed power is studied in [91], by using the coupled surface and volume integral equation. A Surface Integral Equation technique to analyze the EM field in a homogenous dielectric body of revolution has been developed in [92]. The dissipated power is accordingly obtained by an integration along the body.

In Chapters 2 and 3 we employed a FT technique to find the infinite cylinder Green's function due to tangentially and normally-polarized point sources from solution of the line sources. Exploiting this Green's function, MoM codes have been developed to calculate the excited and coupled currents of on-body dipoles [2, 25, 29]. Here, we extract an easy formulation, based on the spectral-domain representation, to calculate the power absorbed by an infinite homogenous cylinder (Section 4.2), rather than volume integration over dissipate power. In Section 4.3, the absorbed power of a finite (long) cylinder is obtained from the efficiency of a closely-located antenna using the *CST Microwave Studio* software. A conclusion is drawn in Section 4.4.

4.2 Formulation for the absorbed Power

Fig. 4.1 shows a circular cylinder of radius a, oriented along the $\hat{z}$ axis at the origin of the system of coordinates. Three possible polarizations of a closely-located point source are vertical, horizontal, and normal to the cylinder.

The tangential components of the electric and magnetic fields on the surface of the cylinder ($\boldsymbol{E}_t$=$\boldsymbol{E}_z$+$\boldsymbol{E}_\phi$ and $\boldsymbol{H}_t$=$\boldsymbol{H}_z$+$\boldsymbol{H}_\phi$, respectively) can be used to

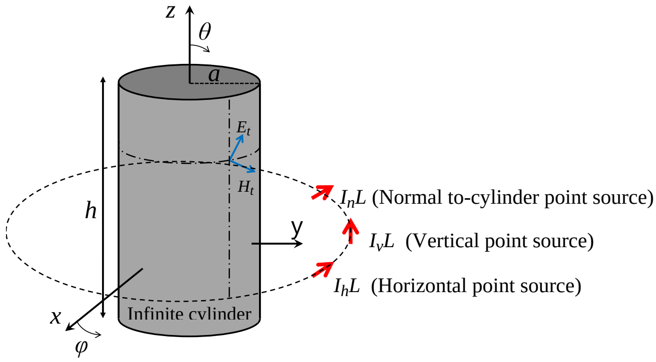

Figure 4.1 An circular lossy cylinder along the $\hat{z}$-axis with radius of a, exposed to the near field of a point source with vertical, horizontal, or normal polarization.

define the total time-average inward-directed power P^s over the body surface as:

$$P^s = \frac{a}{2}\int_{-\infty}^{\infty}\int_{0}^{2\pi} \mathrm{Re}\{E_z(a,\phi,z)H_\phi^*(a,\phi,z) \\ -E_\phi(a,\phi,z)H_z^*(a,\phi,z)\}\mathrm{d}z\mathrm{d}\phi \tag{4.1}$$

where $*$ indicates complex conjugation and Re denotes the real part. P^s is the net flow of energy across the surface of the cylinder and it would be zero, in case of a non-lossy dielectric cylinder.

As we discussed in Chapters 2 and 3, the electric and magnetic fields ($\boldsymbol{E}$ and $\boldsymbol{H}$), inside or outside the cylinder and due to an arbitrarily-polarized point source at $\rho = \rho_s$, can be defined based on their cylindrical harmonics ($\tilde{\boldsymbol{E}}_m$ and $\tilde{\boldsymbol{H}}_m$) [2,29]:

$$\begin{Bmatrix} \boldsymbol{E}(z,\phi) \\ \boldsymbol{H}(z,\phi) \end{Bmatrix} = \frac{1}{2\pi}\sum_{m=-\infty}^{\infty}\int_{k_z=-\infty}^{\infty}\begin{Bmatrix} \tilde{\boldsymbol{E}}_m(k_z,m) \\ \tilde{\boldsymbol{H}}_m(k_z,m) \end{Bmatrix} e^{j(m\phi - k_z z)}\mathrm{d}k_z \tag{4.2}$$

where k_z is the wave vector along z and m is the cylindrical harmonic order. Field harmonics $\tilde{\boldsymbol{E}}_m$ and $\tilde{\boldsymbol{H}}_m$ consist of the incident fields from the source and the fields scattered by the cylinder.

The spectral field components on the cylinder surface can be written as:

$$\tilde{E}_{z,m} = A_m J_m(k'_\rho a) \tag{4.3}$$

$$\tilde{H}_{z,m} = B_m J_m(k'_\rho a) \tag{4.4}$$

where ${k'_\rho}^2$+${k_z}^2$=k^2 and k is the wavenumber inside the cylinder k=$k_0\sqrt{\mu_r \epsilon_r}$. A_m and B_m are complex constant coefficients associated to TM^z and TE^z modes, respectively. They can be obtained by applying the boundary conditions on the surface of the cylindrical current sheet (see Sections 2.3.2 and 3.2.2), using the incident field harmonics from the source. The other components of the fields on the surface of the cylinder (ρ=a) can be determined by the vertical components (See Appendix B, and (2.16)).

Using (4.2), P^s can be described based on cylindrical field harmonics:

$$\begin{aligned} P^s = \frac{a}{2} \int\limits_{z=-\infty}^{\infty} \int\limits_{\phi=0}^{2\pi} \frac{1}{(2\pi)^2} \mathrm{Re}\{ \sum_{m=-\infty}^{\infty} \int\limits_{k_z=-\infty}^{\infty} & \tilde{E}_{zm}(m,k_z) e^{j(m\phi - k_z z)} \mathrm{d}k_z \times \\ \sum_{m'=-\infty}^{\infty} \int\limits_{k'_z=-\infty}^{\infty} & \tilde{H}^*_{\phi m'}(m',k'_z) e^{-j(m'\phi - k'_z z)} \mathrm{d}k'_z - \\ \sum_{m=-\infty}^{\infty} \int\limits_{k_z=-\infty}^{\infty} & \tilde{E}_{\phi m}(m,k_z) e^{j(m\phi - k_z z)} \mathrm{d}k_z \times \\ \sum_{m'=-\infty}^{\infty} \int\limits_{k'_z=-\infty}^{\infty} & \tilde{H}^*_{zm'}(m',k'_z) e^{-j(m'\phi - k'_z z)} \mathrm{d}k'_z \} \mathrm{d}\phi \mathrm{d}z \end{aligned} \tag{4.5}$$

We can rewrite it as:

$$\begin{aligned} P^s = \tfrac{a}{2(2\pi)^2} \int\limits_{z=-\infty}^{\infty} \int\limits_{\phi=0}^{2\pi} \int\limits_{k_z=-\infty}^{\infty} \int\limits_{k'_z=-\infty}^{\infty} \sum_{m=-\infty}^{\infty} \sum_{m'=-\infty}^{\infty} \mathrm{Re}\{ & \tilde{E}_{zm}(m,k_z) \tilde{H}^*_{\phi m'}(m',k'_z) \\ - \tilde{E}_{\phi m}(m,k_z) \tilde{H}^*_{zm'}(m',k'_z) e^{j((m-m')\phi + (k_z - k'_z) z)} \} & \mathrm{d}k_z \mathrm{d}k'_z \mathrm{d}\phi \mathrm{d}z \end{aligned} \tag{4.6}$$

Since the integration and summation of the exponential factors produce $(2\pi)^2 \delta_k(m-m')\delta(k_z - k'_z)$[1], we can describe P^s in a simple form (akin to Parseval's theorem):

$$\begin{aligned} P^s = \frac{a}{2} \sum_{m=-\infty}^{\infty} \int_{k_z=-\infty}^{\infty} \mathrm{Re}\{ & \tilde{E}_{zm}(m,k_z) \tilde{H}^*_{\phi m}(m,k_z) \\ & - \tilde{E}_{\phi m}(m,k_z) \tilde{H}^*_{zm}(m,k_z) \} \mathrm{d}k_z \end{aligned} \tag{4.7}$$

[1] δ and δ_k are the Dirac and the Kronecker delta functions, respectively.

Applying (4.3), (4.4), (B.7), and (B.8), we can expand $\tilde{E}_{zm}(m,k_z)\tilde{H}^*_{\phi m}(m,k_z) - \tilde{E}_{\phi m}(m,k_z)\tilde{H}^*_{zm}(m,k_z)$ based on the Bessel functions:

$$\begin{aligned} A_m J_m(k'_\rho a)\{\frac{j\omega\epsilon A^*_m J^*_m(k'_\rho a)}{k'_\rho} + \frac{mk_z B^*_m J^*_m(k'_\rho a)}{\rho k'^2_\rho}\} - \\ B_m J_m(k'_\rho a)\{\frac{mk_z A^*_m J^*_m(k'_\rho a)}{\rho k'^2_\rho} + \frac{j\omega\mu B^*_m J^*_m(k'_\rho a)}{k'_\rho}\} \end{aligned} \tag{4.8}$$

Applying (4.8) to (4.7), we can express P^s in terms of TE^z, TM^z, and coupled modes:

$$\begin{aligned} P^s &= P^s(\mathrm{TM^z}) + P^s(\mathrm{TE^z}) + P^s(\mathrm{Coupled}) \\ &= \sum_{m=-\infty}^{\infty}\int_{-\infty}^{\infty}\mathrm{Re}\{\frac{k}{\eta}\xi|A_m|^2 + k\eta\xi^*|B_m|^2 + \zeta A_m B^*_m\}\mathrm{d}k_z \end{aligned} \tag{4.9}$$

with

$$\xi = \frac{jaJ(k'_\rho a)J^{*'}(k'_\rho a)}{2k^{*'}_\rho}$$

$$\zeta = \frac{-jmk_z J(k'_\rho a)J^*(k'_\rho a)}{k^{*'2}_\rho}$$

where η is the wave impedance inside the cylinder. The existence of the coupled term $P^s(Coupled)$ means that the dissipated power should not be modeled just by pure TE^z and TM^z modes.

To see which percentage of the energy is absorbed by the lossy cylinder, one can calculate the total time-average radiated power from the point source P^t. The difference $(P^t - P^s)$ is the total radiated power that can be obtained by integrating the Poynting vector over a closed surface, where an asymptotic approximation of Hankel functions for large argument can be used. By excluding the effects of the lossy cylinder, the maximum radiated power from a point source can be easily calculated in free space, using a closed-surface integration of the real part of the Poynting vector [93]. The current $\mathbf{I}$ is extending over incremental length L of the point source. A normalized form of the absorbed power $\bar{P}^s = P^s/|\mathbf{I}L|^2$ is presented in Section 4.3, to be verified with the numerical results.

4.3 Analytical and Numerical Results

As an example, we set the permittivity of the lossy cylinder to ϵ_r=47-16.2j, which is the average complex permittivity of the human body tissues at f=2.45 GHz [14].

To simulate the absorbed power with *CST Microwave Studio*, we consider a short dipole antenna (l_a=$\lambda/50$) in the close vicinity of a finite lossy cylinder with hight of h_{CST}=200 cm and radius of a=15 cm. The short antenna has a very poor matching, causing a very small total efficiency $\nu_t \cong 0$.

The radiation efficiency ν_r does not take into account the antenna return loss and it is defined as the ratio of the radiated power P^{rad} to the total accepted power P^{ta} of the antenna. We use ν_r to find the normalized absorbed power $\bar{P}^a$, as given by:

$$\bar{P}^a = \frac{P^{ta} - P^{rad}}{|\mathbf{I}_a l_a|^2} = \frac{(1-\nu_r)P^{ta}}{|\mathbf{I}_a l_a|^2} = \frac{(1-\nu_r)\mathrm{Re}(\mathrm{Z_{in}})}{|l_a|^2} \tag{4.10}$$

where Z_{in}, $\mathbf{I}_a$, and l_a are the impedance, current, and length of the short dipole antenna, respectively.

In Fig. 4.2, we have used (4.10) to give the power absorbed by the infinite cylinder $\bar{P}^s$, due to an arbitrarily polarized point source and for different source-cylinder distances. Based on (4.10), $\bar{P}^a$ of a finite cylinder due to a short dipole is obtained with *CST Microwave Studio*. The comparison between analytical and numerical absorbed powers is performed with respect to a constant current of the source, rather than a constant input power. Because in the analytical approach we can not explicitly define an impedance for a point source. The method proposed in [76,77] is used to obtain the antenna current. A good agreement has been obtained for all polarizations.

While the cylinder is exposed to the near field of a point source, the maximum absorbed power is achieved by normal-to-body polarization. In this zone, the normal point source can excite surface waves around and along the body and since the lossy cylinder can trap the energy in the form of surface waves close to the cylinder-air interface, an increase of the total power absorption ratio can be observed for small antenna-cylinder distances. In case of the far exposure, there would be no strong surface waves on the cylinder and the highest absorption rate belongs to the source with horizontal polarization.

The total absorbed power inside the body for normal, vertical, and horizontal polarizations have been shown in Figs. 4.3.a, 4.3.b, and 4.3.c, respectively. The distance between the center of the short dipole antenna and the cylinder is $\lambda/4$. Note that all the figures contain absolute values and no normalization is applied. Standing waves on the backside of the cylinder show the interactions between the clockwise and counter clockwise excited surface waves around the cylinder [26, 29]. Strong, weak, and zero standing waves have been observed for normal, horizontal, and vertical polarizations, respectively. In addition to the normal-to-body source, the horizontal source can also radiate such that normal-to-body components of the electric field produce surface waves around the body (unlike the case of a vertically-polarized source). The surface waves carry energy around the cylinder and increase the absorbed power, as can be seen in the first row of Fig. 4.3, showing a top view of the absorbed power. The horizontally-polarized point source illuminates a larger area of the cylinder surface as compared to the case of vertically-polarized point sources (Figs. 4.3.b and 4.3.c). Consequently, for any source-cylinder distance, the body-absorption rate in the horizontal case is always higher than in the vertical case.

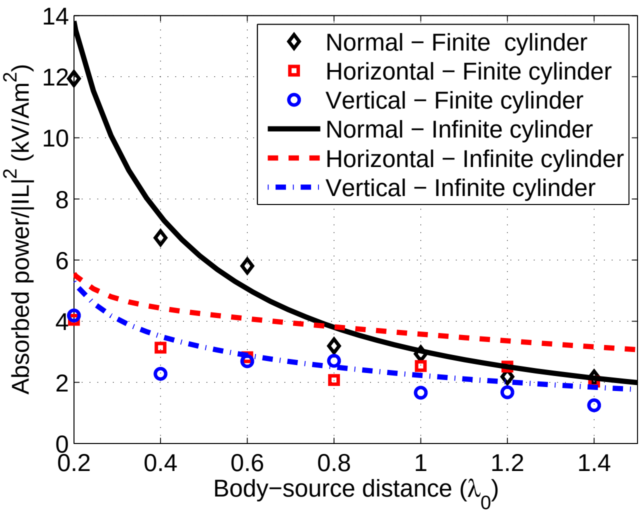

Figure 4.2 The time-average absorbed power by a lossy cylinder with a=15 cm and ϵ_r=47-16.2j, from a point source radiating at f=2.45 GHz. The plain and marked curves are associated respectively with the analytical and the numerical approaches.

In case of a normally-polarized sources, a very slow decay rate of the power density along the cylinder (Fig. 4.3.a) confirms the existence of strong surface waves.

4.4 Conclusion

We derived a simple analytical formulation to calculate the power absorption in cylinders originating from arbitrarily-polarized point sources, based on the FT properties and Parseval theorem. As an example, we set the complex permittivity of the cylinder to that of the human body at f=2.45 GHz. The analytical absorbed power is compared with the results from

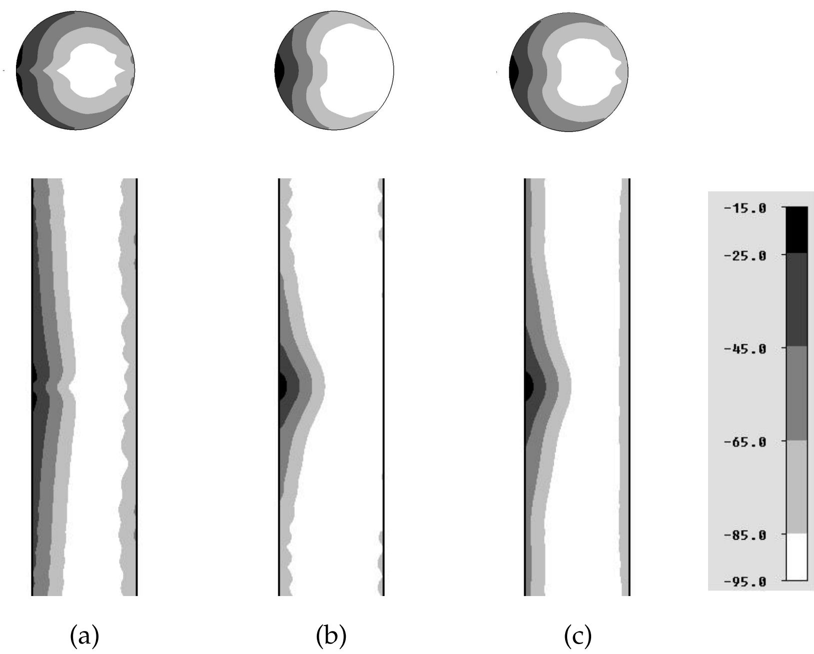

Figure 4.3 Top view (top) and side view (bottom) of the absorbed power density (dBW/m^3) inside the lossy cylinder (with ϵ_r=47-16.2j and a=15 cm) due to a short dipole with length of $\lambda/50$, located at $\lambda/4$ distance from the body and with (a) normal, (b) vertical, and (c) horizontal polarizations.

CST Microwave Studio, where the absorbed power is calculated from the efficiency of a very short dipole antenna in the close vicinity of the cylinder.

We conclude that the maximum power absorption occurs for different source polarizations based on the source-cylinder distances. For a small cylinder-source distance, the cylinder has the highest absorbed power from the normal-to-cylinder point source, because of its capability to launch surface waves around and along cylinder. In case of large source-cylinder distances, the horizontal polarization always causes the maximum power absorption inside the cylinder, because it can better illuminate the surface of the cylinder.

It is desirable to link the current on the antenna with the generator's available power or the power effectively delivered by the antenna in the presence of the scatterer. This will be the subject of a further study.

5 Design of Antennas Devoted to Body Area Networks

This chapter has been removed because of the patent confidentiality.

6 Conclusion

The goal of this thesis was designing a BAN antenna, by analytically modeling the coupling between on-body antennas and a lossy dielectric cylinder which represents a simplified model of the human body. A number of contributions have been brought by this thesis. The main ones are:

- A simplified cylindrical model derived directly from Maxwell's equations and then used to model the body area propagation. Those derivations are not entirely new. They are represented with a new look to help us to implement the Green's function of the electric fields in a MATLAB routine and thereby enable us to achieve results with good convergence. A "modified addition theorem" is proposed to represents the incident fields, radiated from a point source with normal-to-cylinder polarization, in a format similar to what we already have in the conventional tangential-to-cylinder case. The Green's function of the electric fields in the presence of the cylinder is used in a MoM code to study the communications between on-body antennas. This approach is computationally faster than FDTD at the cost of a simplified body model. However, considering that all bodies are different, an exact calculation of electric field values near a particular body model may not provide significantly more insight than a cylindrical approximation, at least as far as antenna design is concerned. Furthermore, if more precise field values are necessary, FDTD methods can be used to fine-tune or verify antenna parameters obtained more easily with the method of moments.

• The following approximate body area propagation trends are identified for tangential-to-body antennas:
- $|E|^2 \propto d^{-2}$ away from the body
- $|E|^2 \propto \exp(-\alpha d)$ into the body
- $|E|^2 \propto \exp(-\beta d)$ around the bodywith $\alpha \cong$0.4
- $|E|^2 \propto d^{-m}$ along the body with $m \cong 3 - 3.5$
where d is the distance, and the decay rates (α, β, and m) depend on several factors including the tissue properties, frequency, polarity, and proximity to the body. While they cannot be evaluated directly, they can be estimated easily from our analytical model much faster than with numerical simulation methods such as FDTD.

• We have shown that the measured average pathloss trends of compact tangentially polarized antennas follows the trends predicted from analytical approach, for propagation around and along a lossy cylinder.

• The field originating from a radially-polarized point source and scattered from body (Green's function of cylinder) have been compared with the fields scattered from the perfectly conducting plate, for different positions of the source and observation points.

• Respecting the body-antenna mutual interactions, we have optimized the length and the distance of a dipole to the body, in order to excite the maximum radiating waves around the body, while the antenna keeps its acceptable impedance matching to a 50 Ω generator. Unlike the tangentially-polarized case, the normally-polarized sources are less affected by the lossy scatterers and a short distance between the normally-polarized antenna and the body can guaranty a good return loss of the antenna. Proper design of more complicated antennas with radially-polarized current flows can lead to excellent matching much closer to the body.

• MoM analysis shows that the current of the half-wavelength dipoles gets differently affected by the body. A lossy scatterer boosts the current of the closely-placed tangential dipoles. The equivalent currents induced on the outer part of the conducting body creates an in-phase current on the dipole, which can be regarded as the dipole being almost *short-circuited* by the conducting cylinder. In this case, the fields radiated by currents on the conducting cylinder (or the image of the antenna) can almost compensate those radiated directly by the dipole antenna.

• The analytical-numerical results, which have been verified with the results from commercial simulators and experiments), provide the pathloss trends around the body from modeling the dipole-dipole transmittance on the body:

◇ $0<\phi<10^{\circ}$: A sharp decay of S_{21} with an average rate of -2.86 dB/cm.

◇ $30^{\circ}<\phi<180^{\circ}$: The radiating waves attached to the body-air interface are associated to the dominant path of the propagation, where there is no direct path between the on-body dipoles. The attenuation rate of the transmittance between two dipoles in presence of the body, S_{21}=0.93 dB/cm, is close to that in free space, which is S_{21}=0.82 dB/cm. The decaying rate of the normally-polarized electric fields, originated from the same dipole, with (without) presence of the body is 1.14 dB/cm (0.83 dB/cm). Unlike the cases where the source is placed parallel to the body, the attached waves traveling around the body maintain a high transmittance between normal-to-body antennas, e.g. fields decaying rate in case of a parallel Skycross antenna is 1.8 dB/cm and in case of a normal-to-body dipole antenna is 1.14 dB/cm. It makes the normal-to-body polarization highly favorable to on-body communications.

◇ $150^{\circ}<\phi<210^{\circ}$: The interference of clockwise and counter-clockwise waves in the back of the body produce a strong variation of the antenna transmittance. With or without the presence of the body, S_{21} in this range has very low values, from -50dB to -65dB, so that the simulation and the measurement should be carried out with special considerations.

• A simple analytical formulation to calculate the power absorption in cylinders originating from arbitrarily-polarized point sources have been derived based on the FT properties and the Parseval theorem. The maximum power absorption occurs for different source polarizations based on the source-cylinder distances. For a small cylinder-source distance, the cylinder has the highest absorbed power from the normal-to-cylinder point source, because of its capability to launch surface waves around and along the cylinder. In case of large source-cylinder distances, the horizontal polarization always causes the maximum power absorption inside the cylinder, because it can better illuminate the surface of the cylinder.

• The absorbed power is calculated from the efficiency of a very short dipole antenna in the close vicinity of the cylinder. That power is compared with the absorbed power obtained from the analytical approach.

• As a result of our MoM approach in Section 3, we found that a compact low-profile antenna radiating maximum power tangential to the body surface is required to maximize coupling between body-worn devices, and increase the chance of exciting the creeping waves. Consequently, a low-profile folded monopole antenna, which has a normal-to-body current flow, is designed and fabricated on a circular ground plane. The antenna is matched at 2.45 GHz to a 50 Ω line and it shows a symmetrical radiation pattern. The area of the antenna is equal to a 50-Euro-cent coin and the hight of the antenna is $\lambda/9.5$=1.3 cm.

6.1 Future prospects

Our modeling approach is very generic and we can recommend several future uses and extensions. In the prolongation of this thesis, several items deserve future works. Frequency dispersion and pathloss trends can be investigated for ultra-wideband propagation systems by evaluating the fields across several different frequencies.

The performance of our model is restricted by the infinite circular cylinder approximation. The formulations related to more complicated structures can be driven to increase the model performance: elliptical cylinder to better model the body trunk [111], three cylinders to model the body trunk and arms [28], multilayered cylinder (or sphere) to model the inhomogeneous body trunk (or head) [84, 112], and finite cylinder to better model the body trunk considering the edge effects [32]. The analytical model developed in this thesis can be also used to investigate the *in-body* and *off-body* communications. Locally approximating the curvature of the body with a homogenous lossy cylinder is good enough to design a BAN antenna and there is no strong need to model the body with more complicated structures. However, considering multilayered cylinders may help to better study the creeping waves on the body.

Phase and group velocities and, hence, dispersion of the creeping waves attached to the body-air interface and traveling around the body, can be studied, using the proposed analytical model. Furthermore, the model can be used as a Green's function in a more complete integral equation approach to treat three-dimensional antennas involving dielectric materials. This would also allow the more general study of propagation around curved surfaces, including the study of antennas able to efficiently excite surface waves.

A Modified Addition Theorem

Here, the goal is to express a modified addition theorem in order to represent $\cos(\phi)H_0^{(2)}(K_\rho|\rho-\rho_s|)$ and $\sin(\phi)H_0^{(2)}(K_\rho|\rho-\rho_s|)$ only with the m-order Hankel and Bessel functions. Using the addition theorem [71], we expand $H_0^{(2)}(K_\rho|\rho-\rho_s|)$ as a linear superposition of the undisplaced cylinder harmonics:

$$\cos(\phi)H_0^{(2)}(K_\rho|\rho-\rho_s|) = \sum_{m=-\infty}^{\infty} H_m^{(2)}(K_\rho\rho_s)J_m(K_\rho\rho)\cos(\phi)e^{jm\phi} \tag{A.1}$$

$$\sin(\phi)H_0^{(2)}(K_\rho|\rho-\rho_s|) = \sum_{m=-\infty}^{\infty} H_m^{(2)}(K_\rho\rho_s)J_m(K_\rho\rho)\sin(\phi)e^{jm\phi} \tag{A.2}$$

By shifting the order of series m, we remove the unwanted factors, $\cos(\phi)$ and $\sin(\phi)$:

$$\sum_{m=-\infty}^{\infty} H_m^{(2)}(K_\rho\rho_s)J_m(K_\rho\rho)\cos(\phi)e^{jm\phi} = \tag{A.3}$$

$$\frac{1}{2}\sum_{m=-\infty}^{\infty} H_{m-1}^{(2)}(K_\rho\rho_s)J_{m-1}(K_\rho\rho)e^{jm\phi} + \frac{1}{2}\sum_{m=-\infty}^{\infty} H_{m+1}^{(2)}(K_\rho\rho_s)J_{m+1}(K_\rho\rho)e^{jm\phi}$$

$$\sum_{m=-\infty}^{\infty} H_m^{(2)}(K_\rho\rho_s)J_m(K_\rho\rho)\sin(\phi)e^{jm\phi} = \tag{A.4}$$

$$\frac{1}{2j}\sum_{m=-\infty}^{\infty} H_{m-1}^{(2)}(K_\rho\rho_s)J_{m-1}(K_\rho\rho)e^{jm\phi} - \frac{1}{2j}\sum_{m=-\infty}^{\infty} H_{m+1}^{(2)}(K_\rho\rho_s)J_{m+1}(K_\rho\rho)e^{jm\phi}$$

We hence can rewrite (A.1) and (A.2) as:

$$\cos(\phi)H_0^{(2)}(K_\rho|\rho-\rho_s|) = \tag{A.5}$$
$$\frac{1}{2}\sum_{m=-\infty}^{\infty}\{H_{m-1}^{(2)}(K_\rho\rho_s)J_{m-1}(K_\rho\rho)+H_{m+1}^{(2)}(K_\rho\rho_s)J_{m+1}(K_\rho\rho)\}e^{jm\phi}$$

$$\sin(\phi)H_0^{(2)}(K_\rho|\rho-\rho_s|) = \tag{A.6}$$
$$\frac{1}{2j}\sum_{m=-\infty}^{\infty}\{H_{m-1}^{(2)}(K_\rho\rho_s)J_{m-1}(K_\rho\rho)-H_{m+1}^{(2)}(K_\rho\rho_s)J_{m+1}(K_\rho\rho)\}e^{jm\phi}$$

We suppose the arguments inside the brackets can be written in a form, containing the Bessel functions with the orders of (m-1) and (m+1):

$$\{H_{m-1}^{(2)}(K_\rho\rho_s)J_{m-1}(K_\rho\rho)\pm H_{m+1}^{(2)}(K_\rho\rho_s)J_{m+1}(K_\rho\rho)\} = \tag{A.7}$$
$$\chi^{\pm}(k_\rho\rho_s)\{J_{m-1}(k_\rho\rho)+J_{m+1}(k_\rho\rho)\}+\gamma^{\pm}(k_\rho\rho_s)\{J_{m-1}(k_\rho\rho)-J_{m+1}(k_\rho\rho)\}$$

where χ and γ are unknown coefficients that can be found using [70]:

$$2B_m'(\chi) = B_{m-1}(\chi) - B_{m+1}(\chi) \tag{A.8}$$

$$\frac{2m}{\chi}B_m(\chi) = B_{m-1}(\chi) + B_{m+1}(\chi) \tag{A.9}$$

where $B_m(x)$ are either Bessel or Hankel functions. Inserting those coefficients in (A.8), we obtain:

$$\chi^+(k_\rho\rho_s) = \gamma^-(k_\rho\rho_s) = \frac{m}{k_\rho\rho_s}H_m^{(2)}(K_\rho\rho_s) \tag{A.10}$$

$$\chi^-(k_\rho\rho_s) = \gamma^+(k_\rho\rho_s) = H_m^{(2)'}(K_\rho\rho_s) \tag{A.11}$$

which only contains m-th order Bessel and Hankel functions and their derivatives. This allows us to write:

$$\{H_{m-1}^{(2)}(X)J_{m-1}(Y)+H_{m+1}^{(2)}(X)J_{m+1}(Y)\} = \tag{A.12}$$
$$\frac{2m^2}{XY}H_m^{(2)}(X)J_m(Y)+2H_m^{(2)'}(X)J'_m(Y)$$

$$\{H_{m-1}^{(2)}(X)J_{m-1}(Y)-H_{m+1}^{(2)}(X)J_{m+1}(Y)\} = \tag{A.13}$$
$$\frac{2m}{Y}H_m^{(2)'}(X)J_m(Y)+\frac{2m}{X}H_m^{(2)}(X)J'_m(Y)$$

So, the modified versions of the addition theorem can be written as:

$$\cos(\phi)H_0^{(2)}(K_\rho|\rho-\rho_s|) = \tag{A.14}$$
$$\sum_{m=-\infty}^{\infty}\{\frac{m^2}{k_\rho^2\rho\rho_s}H_m^{(2)}(K_\rho\rho_s)J_m(K_\rho\rho)+H_m^{(2)'}(K_\rho\rho_s)J'_m(K_\rho\rho)\}e^{jm\phi}$$

$$\sin(\phi)H_0^{(2)}(K_\rho|\rho-\rho_s|) = \tag{A.15}$$
$$\sum_{m=-\infty}^{\infty}\{\frac{m}{jk_\rho\rho_s}H_m^{(2)'}(K_\rho\rho_s)J_m(K_\rho\rho)+\frac{m}{jk_\rho\rho}H_m^{(2)}(K_\rho\rho_s)J'_m(K_\rho\rho)\}e^{jm\phi}$$

The Radiated Field Components from the Radially-Polarized Excitation

B

Using the vector potential, the ϕ components of the incident electric and magnetic field harmonics are derived as:

$$E^{il}_{\phi,m} = m\eta\{\frac{k}{k_\rho \rho} H^{(2)'}_m (K_\rho \rho_s) J_m(K_\rho \rho) + \tag{B.1}$$

$$\frac{k}{k_\rho \rho_s} H^{(2)}_m (K_\rho \rho_s) J'_m(K_\rho \rho) + \frac{1}{k\rho} H^{(2)'}_m (K_\rho \rho_s) Q_m\}$$

$$H^{il}_{\phi,m} = -jk_z\{\frac{m^2}{k^2_\rho \rho \rho_s} H^{(2)}_m (K_\rho \rho_s) J_m(K_\rho \rho) + H^{(2)'}_m (K_\rho \rho_s) J'_m(K_\rho \rho)\} \tag{B.2}$$

where Q_m is defined by (3.10).

Following [113], all field components can be obtained from z components, given in (3.8-3.9):

$$\begin{aligned} \mathbf{E_s} &= \tfrac{1}{k^2_\rho} \left(-jk_z \nabla_s E_z + j\omega\mu \hat{z} \times \nabla_s H_z\right) \\ \mathbf{H_s} &= \tfrac{1}{k^2_\rho} \left(-jk_z \nabla_s H_z - j\omega\epsilon \hat{z} \times \nabla_s E_z\right) \end{aligned} \tag{B.3}$$

with

$$\begin{gathered} \nabla_s = \hat{\rho}\tfrac{\partial}{\partial\rho} + \hat{\phi}\tfrac{jm}{\rho} \\ \hat{z} \times \nabla_s = \hat{\phi}\tfrac{\partial}{\partial\rho} - \hat{\rho}\tfrac{jm}{\rho} \end{gathered} \tag{B.4}$$

The results are:

$$E^{sl}_{\rho,m} = \begin{cases} \dfrac{-jk_z A_m J'_m(k'_\rho \rho)}{k'_\rho} + \dfrac{m\omega\mu B_m J_m(k'_\rho\rho)}{\rho k'^2_\rho} & a \geq \rho \\ \\ \dfrac{-jk_z A'_m H^{(2)'}_m(k_\rho\rho)}{k_\rho} + \dfrac{m\omega\mu B'_m H_m(k_\rho\rho)}{\rho k^2_\rho} & \rho \geq a \end{cases} \tag{B.5}$$

$$H^{sl}_{\rho,m} = \begin{cases} \dfrac{-m\omega\epsilon_0\epsilon_r A_m J_m(k'_\rho \rho)}{k'^2_\rho \rho} - \dfrac{jk_z B_m J'_m(k'_\rho\rho)}{k'_\rho} & a \geq \rho \\ \\ \dfrac{-m\omega\epsilon_0 A'_m H^{(2)}_m(k_\rho\rho)}{k^2_\rho \rho} - \dfrac{jk_z B'_m H^{(2)'}_m(k_\rho\rho)}{k_\rho} & \rho \geq a \end{cases} \tag{B.6}$$

$$E^{sl}_{\phi,m} = \begin{cases} \dfrac{mk_z A_m J_m(k'_\rho \rho)}{k'^2_\rho \rho} + \dfrac{j\omega\mu B_m J'_m(k'_\rho\rho)}{k'_\rho} & a \geq \rho \\ \\ \dfrac{mk_z A'_m H^{(2)}_m(k_\rho\rho)}{k^2_\rho \rho} + \dfrac{j\omega\mu B'_m H^{(2)'}_m(k_\rho\rho)}{k_\rho} & \rho \geq a \end{cases} \tag{B.7}$$

$$H^{sl}_{\phi,m} = \begin{cases} \dfrac{-j\omega\epsilon_0\epsilon_r A_m J'_m(k'_\rho \rho)}{k'_\rho} + \dfrac{mk_z B_m J_m(k'_\rho\rho)}{k'^2_\rho \rho} & a \geq \rho \\ \\ \dfrac{-j\omega\epsilon_0 A'_m H^{(2)'}_m(k_\rho\rho)}{k_\rho} + \dfrac{mk_z B'_m H^{(2)}_m(k_\rho\rho)}{k^2_\rho \rho} & \rho \geq a \end{cases} \tag{B.8}$$

Applying Addition theorem to vertically-polarized sources

C

The z-component of the electric field harmonic, due to a vetically-polarized line source, can be written based on the magnetic vector potential $\mathbf{A}^l_m$ as:

$$\mathbf{E}^{il}_{z,m} = -j\omega\mu\mathbf{A}^l_m - \frac{j}{\omega\epsilon}\nabla(\nabla\cdot\mathbf{A}^l_m) \tag{C.1}$$

We use addition theorem, applied to the second-kind Hankel functions, to obtain the vector potential ($\mathbf{A}^l$) [72] :

$$\mathbf{A}^l = \frac{\hat{z}}{4j}H_0^{(2)}(k_\rho|\rho-\rho_s|) = \frac{\hat{z}}{4j}\sum_{m=-\infty}^{\infty}H_m^{(2)}(k_\rho\rho_s)J_m(k_\rho\rho)e^{j(m\phi-k_z z)} \tag{C.2}$$

where ρ_s (larger than ρ) is the radial distance of the source from the origin and ${k_\rho}^2$+${k_z}^2$=k^2. From (C.1) and (C.2), the harmonics of the electric field in the z direction can be derived in terms of m^{th} order Bessel and Hankel functions:

$$\mathbf{E}^{il}_{z,m} = -\frac{k_\rho^2}{4\omega\epsilon}H_m^{(2)}(k_\rho\rho_s)J_m(k_\rho\rho) \tag{C.3}$$

which is consistent with the results in (2.20) and (2.11), where a current sheet model of the source has been used.

Short dipole antenna

D

A short dipole antenna (probe) is needed in order to measure the received signal with linear polarization. Decreasing the length of the dipole antenna also enables us to measure the normal-to-body fields closer to the body without significant perturbation. If we simply cut the arms of a dipole antenna, matching of the antenna to a 50-ohm line dramatically decreases and a very small fraction of the available power can radiate. As an example a quarter-wavelength dipole has a reflection coefficient of S_{11}=-1 dB. To solve this problem, we have designed a matching network at f=2.45 GHz, as shown in Fig. D.1. We first measured the input impedance of the probe in the close vicinity to the human body and then we used that impedance to design the matching-network. A long matching network is designed to keep the cables far enough from the probe, to minimize the effects of wires. A parallel stub, terminated in a open circuit, cancels the imaginary part of the input admittance. Fig. D.2 shows the measured return loss of the antenna with the matching network, in which S_{11} at f=2.45 GHz is improved from -1 dB to -11 dB.

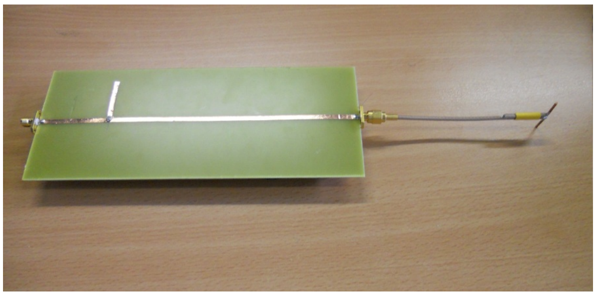

Figure D.1 Short dipole antenna matched to the 50-ohm transmission line, through a matching network.

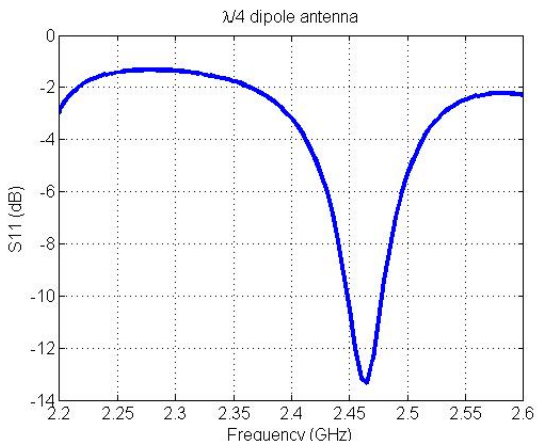

Figure D.2 The measured return loss of the short dipole antenna which is improved by the matching network.

List of Publications

Journal papers

Published

- L. Liu, F. Keshmiri, C. Craeye, P. De Doncker, and C. Oestges, "An Analytical Modeling of Polarized Timevariant On-body Propagation Channels with Dynamic Body Scattering," *EURASIP Journal on Wireless Communications and Networking*, pp 1-15, Apr. 2011.
- A. Fort, F. Keshmiri, G. Roqueta, C. Craeye, and C. Oestges, "A Body Are Propagation Model Derived from Fundamental Principles: analytical Analysis and Comparison with Measurements," *IEEE Transactions on Antenna and Propagations*, Vol. 58, no. 2, pp 503-514, Feb. 2010.

Pending

- F. Keshmiri, and C. Craeye, "Moment-Method Analysis of Normal-to-Body Antennas Using a Green's Function Approach," *IEEE Transactions on Antenna and Propagations*.
- F. Keshmiri, and C. Craeye, "Polarization-Dependent Power Absorption in Cylindrical Bodies:Analytical Formulation and Numerical Validation," *IEEE Transactions on Antenna and Propagations*.
- C. Craeye, and F. Keshmiri "On the power radiated by a point source in the presence of a scatterer," *IEEE Transactions on Antenna and Propagations*.

Conference papers (Peer-reviewed)

- F. Keshmiri, T. Yilmaz, Y. Hao and C. Craeye, "MoM analysis of antenna devoted to BAN," in Proceedings of the *5th European Conference on Antennas and Propagation (EUCAP2011)*, pp.441-444, Rome, Italy, Apr. 2011.

- F. Keshmiri and C. Craeye, "Wave Propagation from Sources with Arbitrary Polarization Next to the Human Body," in Proceeding of the *IEEE AP-S/USNC/URSI International Symposium*, Toronto, Canada, Jul. 2010.

- L. Liu, F. Keshmiri, P. De. Doncker, C. Craeye, and C.Oestges, "3-D Body Scattering Interference to Vertically Polarized On-Body Propagation," in Proceeding of the *IEEE AP-S/USNC/URSI International Symposium*, Toronto, Canada, Jul. 2010.

- A. Mallat, P. Gérard, F. Keshmiri, C. Oestges, and C. Craeye, D. Flandre and L. Vandendorpe, "Testbed for IR-UWB Based Ranging and Positioning: Experimental Performance and Comparison to CRLBs," in Proceeding of the *IEEE International Symposium Wireless Pervasive Comp. (ISWPC)*, Modena, Italy, May 2010.

- F. Keshmiri, and C. Craeye, "A Green's Function Approach for Analysis of Body-Area-Network Antennas," in Proceeding of the *Loughborough Antennas and Propagation Conference (LAPC2009)*, London, UK, Nov. 2009.

- A. Fort, F. Keshmiri, L. Liu, C. Oestges, Ph. De. Doncker, and C. Craeye, "Analysis of Wave Propagation Including Shadow Fading Correlation for BAN Applications," textitIET seminar, London, UK, Apr. 2009.

- F. Keshmiri, A. Fort, and C.Craeye, "Analysis of Wave Propagation for BAN Application," in Proceeding of the *3rd European Conference*

on Antennas and Propagation (EuCAP2009), Berlin, Germany, Mar. 2009.

- F. Keshmiri, R. Chandra, and C. Craeye, "Design of a UWB Antenna with Stabilized Radiation Pattern," in Proceeding of the *IEEE AP-S/USNC/URSI International Symposium*, San Diego, USA, Jul. 2008.

Bibliography

[1] F. Keshmiri, A. Fort, and C. Craeye, "Analysis of wave propagation for BAN applications," in *Antennas and Propagation, 2009. EuCAP 2009. 3rd European Conference on*, march 2009, pp. 709 –712.

[2] A. Fort, F. Keshmiri, G. Roqueta, C. Craeye, and C. Oestges, "A body area propagation model derived from fundamental principles: analytical analysis and comparison with measurements," *IEEE Transactions on Antenna and Propagations*, vol. 58, no. 2, pp. 503–514, February 2010.

[3] The Visible Human Project, U.S. National Library of Medicine. [Online]. Available: http://vimeo.com/21371213

[4] S. Ullah, H. Higgins, B. Braem, B. Latre, C. Blondia, I. Moerman, S. Saleem, Z. Rahman, and K. S. Kwak, "A comprehensive survey of wireless body area networks: On PHY, MAC, and network layers solutions," *Journal of Medical Systems (Springer)*, 2010.

[5] B. Gyselinckx, C. V. Hoof, and S. Donnay, "Body area networks, the ascent of autonomous wireless microsystems," in *International Symposium on Hardware Technology Drivers of Ambient Intelligence*, 2004.

[6] P. S. Hall and Y. Hao, *Antennas and propagation for body-centric Wireless Communications*. Norwood, Massachusetts: Artech House, Inc., 2006.

[7] P. Hall, M. Ricci, and T. Hee, "Measurements of on-body propagation characteristics," in *International Conference on Microwave and Millimeter Wave Technology*, 2002, pp. 770–772.

[8] A. Fort, C. Desset, J. Ryckaert, P. D. Doncker, L. V. Biesen, and P. Wambacq, “Characterization of the ultra-wideband body area propagation channel,” in *International Conference on Ultra-Wideband ICU*, Zurich, Switzerland, 2005, pp. 22–27.

[9] A. Alomainy, Y. Hao, X. Hu, C. G. Parini, and P. S. Hall, “UWB on-body radio propagation and system modelling for wireless body-centric networks,” in *IEE Communications Proceedings*, vol. 153, no. 1, February 2006, pp. 107–114.

[10] E. Reusens and W. Joseph, “On-body measurements and characterization of wireless communication channel for arm and torso of human,” in *International Workshop on Wearable and Implantable Body Sensor Networks*, Aachen, Germany, 2007, pp. 264–269.

[11] H. Ghannoum, C. Roblin, and X. Begaud, “Investigation and modeling of the UWB on-body propagation channel,” *Springer*, vol. 52, no. 1, pp. 17–28, May 2010.

[12] T. Zasowski, F. Althaus, M. Stager, A. Wittneben, and G. Trőster, “UWB for noninvasive wireless body area networks: channel measurements and results,” in *2003 IEEE Conference on Ultra Wideband Systems and Technologies*, 2003, pp. 285–289.

[13] A. Fort, C. Desset, J. Ryckaert, P. De Doncker, L. Van Biesen, and P. Wambacq, “Characterization of the ultra wideband body area propagation channel,” in *International Conference on Ultra-Wideband (ICU) Proceedings*, Zurich, September 2005, pp. 22–27.

[14] Y. Hao, A. Alomainy, P. S. Hall, Y. I. Nechayev, C. G. Parini, and C. C. Constantinou, “Antennas and propagation for body centric wireless communications,” in *IEEE/ACES International Conference on Wireless Communications and Applied Computational Electromagnetics*, 2005, pp. 586–589.

[15] S. Dumanli and C. Railton, “On-body transmission at 5.2 GHz: Simulations using FDTD with a time domain huygen’s technique,” *IEEE Transactions on Antennas and Propagation*, vol. 59, no. 10, pp. 3910 –3917, oct. 2011.

[16] W. Scanlon and N. Evans, "Numerical analysis of bodyworn UHF antenna systems," *Electronics and Communication Engineering Journal*, vol. 13, no. 2, pp. 53–64, 2001.

[17] J. Ryckaert, P. DeDoncker, S. Donnay, A. Delehoye, and R.Meys, "Channel model for wireless communication around the human body," in *Electronics letters*, vol. 40, no. 9, April 2004, pp. 543–544.

[18] Y. Zhao, Y. Hao, A. Alomainy, and C. Parini, "Uwb on-body radio channel modeling using ray theory and subband fdtd method," *Microwave Theory and Techniques, IEEE Transactions on*, vol. 54, no. 4, pp. 1827 – 1835, june 2006.

[19] E. Reusens, W. Joseph, B. Latre, B. Braem, G. Vermeeren, E. Tanghe, L. Martens, I. Moerman, and C. Blondia, "Characterization of on-body communication channel and energy efficient topology design for wireless body area networks," *IEEE Transactions on Information Technology and Biomedicine*, vol. 13, no. 6, pp. 933–945, November 2009.

[20] A. Fort, J. Ryckaert, C. Desset, P. De Doncker, and L. Van Biesen, "Ultra wideband channel model for communication around the human body," *IEEE Journal on Selected Areas of Communication*, 2006.

[21] A. Fort, C. Desset, P. De Doncker, and L. Van Biesen, "An ultra wideband body area propagation channel model: From statistics to implementation," *IEEE Transactions on Microwave Theory and Techniques*, 2006.

[22] A. Fort, P. Wambacq, C. Desset, and L. V. Biesen, "An indoor body area channel model for narrowband communications," *IET Microwave Antennas and Propagation*, 2007.

[23] A. F. Molisch, D. Cassioli, C.-C. Chong, S. Emami, A. Fort, B. Kannan, J. Karedal, J. Kunisch, H. G. Schantz, K. Siwiak, and M. Z. Win, "A comprehensive standardized model for ultrawideband propagation channels," *IEEE Transactions on Antennas and Propagation*, vol. 54, no. 11, pp. 3143–3150, November 2006.

[24] A. Fort, L. Liu, F. Keshmiri, P. D. Doncker, C. Oestges, and C. Craeye, "Analysis of wave propagation including shadow fading correla-

tion for ban applications," in *IET Antennas and propagations seminar for body-centeric wireless communications*, 2009, pp. 1–28.

[25] F. Keshmiri and C. Craeye, "A Green's function approach for analysis of body-area-network antennas," in *Loughborough Antennas and Propagation Conference LAPC2009*, 2009.

[26] F. Keshmiri, T. Yilmaz, Y. Hao, and C. Craeye, "MoM analysis of antenna devoted to BAN," in *5th European Conference on Antennas and Propagation, EuCAP 2011*, 2011, pp. 441–444.

[27] M. Grimm and D. Manteuffel, "Electromagnetic wave propagation on human trunk models excited by half-wavelength dipoles," in *Loughborough Antennas and Propagation Conference LAPC2010*, 2010, pp. 493–496.

[28] L. Liu, F. Keshmiri, C. Craeye, P. D. Doncker, and C. Oestges, "An analytical modeling of polarized time-variant on-body propagation channels with dynamic body scattering," *EURASIP Journal on Wireless Communications and Networking*, pp. 1–15, April 2011.

[29] F. Keshmiri and C. Craeye, "Moment-method analysis of normal-to-body antennas using a Green's function approach," *IEEE Transactions on Antennas and Propagation*, Under revision, 2011.

[30] S. Khalatbari, D. Sardari, A. Mirzaee, and H. Sadafi, "Calculating SAR in two models of the human head exposed to mobile phones radiations at 900 and 1800 MHz," in *Progress in Electromagnetics Research Symposium PIERS*, Cambridge, USA, March 2006.

[31] S. H. Kvist, J. Thaysen, and K. Jakobsen, "The effect of the head size on the ear-to-ear radio-propagation channel for body-centric wireless networks," in *Loughborough Antennas and Propagation Conference LAPC2009*, 2010, pp. 345–348.

[32] T. U. T. Sasamori, M. Takahashi, "Transmission mechanism of wearable device for on-body wireless communications," *IEEE Transactions on Antenna and Propagations*, vol. 57, no. 4, pp. 936–942, April 2009.

[33] J. B. Keller, "Geometrical theory of diffraction," *Journal of the Optical Society of America*, vol. 52, pp. 116–130, 1962.

[34] R. Kouyoumjian and P. Pathak, "A uniform geometrical theory of diffraction for an edge in a perfectly conducting surface," *Proceedings of the IEEE*, vol. 62, no. 11, pp. 1448 – 1461, nov. 1974.

[35] D. A. Mcnamara, C. Pistorius, and J. Malherbe, *Introduction to the uniform geometrical theory of diffraction*. Artech House: Boston, 1991.

[36] P. Pathak, W. Burnside, and R. Marhefka, "A uniform gtd analysis of the diffraction of electromagnetic waves by a smooth convex surface," *IEEE Transactions on Antennas and Propagation*, vol. 28, no. 5, pp. 631 – 642, sep 1980.

[37] P. Pathak, N. Wang, W. Burnside, and R. Kouyoumjian, "A uniform gtd solution for the radiation from sources on a convex surface," *IEEE Transactions on Antennas and Propagation*, vol. 29, no. 4, pp. 609 – 622, jul 1981.

[38] CDC. [Online]. Available: http://www.cdc.gov/nchs/fastats/bodymeas.htm

[39] T. Alves, B. Poussot, and J.-M. Laheurte, "Analytical propagation modeling of ban channels based on the creeping-wave theory," *IEEE Transactions on Antennas and Propagation*, vol. 59, no. 4, pp. 1269 –1274, april 2011.

[40] A. Lea, P. Hui, J. Ollikainen, and R. Vaughan, "Propagation between on-body antennas," *IEEE Transactions on Antennas and Propagation*, vol. 57, no. 11, pp. 3619 –3627, nov. 2009.

[41] L. Akhoondzadeh-Asl, Y. Nechayev, and P. Hall, "Surface and creeping waves excitation by body-worn antennas," in *Antennas and Propagation Conference (LAPC), 2010 Loughborough*, nov. 2010, pp. 48 –51.

[42] G. Conway, W. Scanlon, S. Cotton, and M. Bentum, "An analytical path-loss model for on-body radio propagation," in *Electromagnetic Theory (EMTS), 2010 URSI International Symposium on*, aug. 2010, pp. 332 –335.

[43] A. V. Raisanen and A. Lehto, *Radio engineering for wireless communication and sensor applications*. Artech House, 2003.

[44] A. Eid, N. Murtaza, and J. Wallace, "Green's function models and measurements for body area network (ban) channels," in *Wireless Information*

Technology and Systems (ICWITS), 2010 IEEE International Conference on, 28 2010-sept. 3 2010, pp. 1 –4.

[45] A. Eid and J. Wallace, "Accurate modeling of body area network channels using surface-based method of moments," *IEEE Transactions on Antennas and Propagation*, vol. 59, no. 8, pp. 3022 –3030, aug. 2011.

[46] L. Akhoondzadeh-Asl, I. Khan, and P. Hall, "Polarisation diversity performance for on-body communication applications," *Microwaves, Antennas Propagation, IET*, vol. 5, no. 2, pp. 232 –236, 31 2011.

[47] F. Keshmiri and C. Craeye, "Wave propagation from sources with arbitrary polarization next to the human body," in *URSI International Symposium*, Toronto, Canada, July 2010.

[48] A. Khaleghi and I. Balasingham, "Non-line-of-sight on-body ultra wideband (1-6 GHz) channel characterisation using different antenna polarisations," *Microwaves, Antennas Propagation, IET*, vol. 3, no. 7, pp. 1019 –1027, october 2009.

[49] G. Roqueta, A. Fort, C. Craeye, and C. Oestges, "Analytical propagation models for body area networks," in *Antennas and Propagation for Body-Centric Wireless Communications, 2007 IET Seminar on*, april 2007, pp. 90 –96.

[50] ——, "Analytical propagation models for body area networks," in *Proceedings of the IET Seminar on Antennas and propagation for body-centric wireless communicatinos*, London, UK, April 2007, pp. 90–96.

[51] W. C. Chew, *Waves and fields in inhomogeneous media*. New York: IEEE Press, 1995.

[52] V. Erturk and R. Rojas, "Efficient computation of surface fields excited on a dielectric-coated circular cylinder," *Antennas and Propagation, IEEE Transactions on*, vol. 48, no. 10, pp. 1507 –1516, oct 2000.

[53] J. Sun, C.-F. Wang, L.-W. Li, and M.-S. Leong, "Further improvement for fast computation of mixed potential green's functions for cylindrically stratified media," *Antennas and Propagation, IEEE Transactions on*, vol. 52, no. 11, pp. 3026 – 3036, nov. 2004.

[54] S. Raffaelli, Z. Sipus, and P.-S. Kildal, “Analysis and measurements of conformal patch array antennas on multilayer circular cylinder,” *Antennas and Propagation, IEEE Transactions on*, vol. 53, no. 3, pp. 1105 – 1113, march 2005.

[55] C. M. Bender and S. A. Orszag, *Advanced Mathematical Methods for Scientists and Engineers. Asymptotic Methods and Perturbation Theory*. Springer-Verlag, 1999.

[56] C. F. du Toit, “A procedure for determining the largest computable order of bessel functions of the second kind and hankel functions,” *IEEE Transactions on Antennas and Propagation*, vol. 41, no. 12, pp. 1741 – 1742, December 1993.

[57] C. C. Johnson and A. W. Guy, “Nonionizing electromagnetic wave effects in biological materials and sytems,” *Proceedings of the IEEE*, vol. 60, no. 6, pp. 692–718, June 1972.

[58] D. K. Cheng, *Field and Wave Electromagnetics, Second Edition*. Reading, Massachusetts: Adisson-Wesley Publishing Company, 1992.

[59] A. Fort, C. Desset, J. Ryckaert, P. DeDoncker, L. Van Biesen, and S. Donnay, “Ultra wide-band body area channel model,” in *International Conference on Communications (ICC) Proceedings*, vol. 4, Seoul, Korea, May 2005, pp. 2840–2844.

[60] International Telecommunications Union - Radiocommunications (ITU-R), “Radio regulations, section 5.138 and 5.150,” Available at http://www.itu.int/home.

[61] IEEE, “IEEE 802.15.4, wireless medium access control (MAC) and physical layer (PHY) specifications for low-rate wireless personal area networks (LR-WPANs),” October 2003.

[62] “The bluetooth standard version 1b,” Available at http://www.bluetooth.com.

[63] Skycross, http://www.skycross.com.

[64] W. G. Scanlon, N. E. Evans, and M. Rollins, "Antenna-body interaction effects in a 418 MHz radio telemeter for infant use," in *18th Annual International Conference of the IEEE Engineering in Medicine and Biology Society*, 1996, pp. 278–279.

[65] A. Fort, "Body area communications:chanel characterization and ultra-wideband system-level approach for low power," Ph.D. dissertation, Vrije Universiteit Brussel, November 2007.

[66] C.-T. Tai, *Dyadic Green's Functions in Electromagnetic Theory*, 2nd ed. New York: IEEE Press, 1994.

[67] G. Keiser, *Optical Fiber Communication*. New York: McGraw Hill, 1983.

[68] A. Gupta and T. Abhayapala, "Body area networks: Radio channel modelling and propagation characteristics," in *Communications Theory Workshop, 2008. AusCTW 2008. Australian*, 30 2008-feb. 1 2008, pp. 58 –63.

[69] L.-W. Li, H.-G. Wee, and M.-S. Leong, "Dyadic Green's functions inside/outside a dielectric elliptical cylinder: theory and application," *IEEE Transactions on Antennas and Propagation*, vol. 51, no. 3, pp. 564 – 574, march 2003.

[70] CST Microwave Studio 2011. [Online]. Available: www.CST.com

[71] P. M. Morse and H. Feshbach, *Methods of theoretical physics*. New York: McGraw-Hill, 1953.

[72] R. F. Harrington, *Time-Harmonic Electromagnetic Fields*. New York: McGraw-Hill, 1961.

[73] C. A. Balanis, *Advanced Engineering Electromagnetics*. New York: John Wiley & Sons, 1989.

[74] R. F. Harrington, *Field Computations by Moment Methods*. New York: IEEE Press, 1993.

[75] B. Derat, A. Cozza, and J.-C. Bolomey, "Influence of source - phantom multiple interactions on the field transmitted in a flat phantom," in *Electromagnetic Compatibility, 2007. EMC Zurich 2007. 18th International Zurich Symposium on*, sept. 2007, pp. 139 –142.

[76] C. Craeye, B. A. Garcia, E. G. Munoz, and R. Sarkis, "An open-source code for the calculation of the effects of mutual coupling in arrays of wires and for the ASM-MBF method," *International Journal of Antennas and Propagation*, 2010.

[77] R. Sarkis and C. Craeye, "Simulation of large circular antenna arrays using the array scanning method," in *Antennas and Propagation (EuCAP), 2010 Proceedings of the Fourth European Conference on*, april 2010, pp. 1 –4.

[78] 4NEC2 antenna modeler and optimizer. [Online]. Available: http://home.ict.nl/~arivoors/

[79] S. J. Orfanidis, *Electromagnetic Waves and Antennas*. http://www.ece.rutgers.edu/ orfanidi/ewa/, 2008.

[80] P. Hall, Y. Hao, Y. Nechayev, A. Alomalny, C. Constantinou, C. Parini, M. Kamarudin, T. Salim, D. Hee, R. Dubrovka, A. Owadally, W. Song, A. Serra, P. Nepa, M. Gallo, and M. Bozzetti, "Antennas and propagation for on-body communication systems," *Antennas and Propagation Magazine, IEEE*, vol. 49, no. 3, pp. 41 –58, june 2007.

[81] A. Sabbah, N. Dib, and M. Al-Nimr, "Evaluation of specific absorption rate and temperature elevation in a multi-layered human head model exposed to radio frequency radiation using the finite-difference time domain method," *Microwaves, Antennas Propagation, IET*, vol. 5, no. 9, pp. 1073 –1080, 27 2011.

[82] P. J. Dimbylow, "Fine resolution calculations of SAR in the human body for frequencies up to 3 GHz," *Physics in Medicine and Biology*, vol. 47, no. 16, pp. 2835 –2846, 2002.

[83] D. Poljak, *Human Exposure to Electromagnetic Fields*. Southampton, U.K.: WIT press, 2004.

[84] J. Kim and Y. Rahmat-Samii, "Implanted antennas inside a human body: simulations, designs, and characterizations," *Microwave Theory and Techniques, IEEE Transactions on*, vol. 52, no. 8, pp. 1934 – 1943, aug. 2004.

[85] D. Sullivan, O. Gandhi, and A. Taflove, "Use of the finite-difference time-domain method for calculating EM absorption in man models,"

Biomedical Engineering, IEEE Transactions on, vol. 35, no. 3, pp. 179 –186, march 1988.

[86] S.-G. Zhu, K.-M. Chen, and H.-R. Chuang, “Interaction of the near-zone fields of a slot on a conducting sphere with a spherical model of man,” *Microwave Theory and Techniques, IEEE Transactions on*, vol. 32, no. 8, pp. 784 – 795, aug 1984.

[87] K. Nikita, G. Stamatakos, N. Uzunoglu, and A. Karafotias, “Analysis of the interaction between a layered spherical human head model and a finite-length dipole,” *Microwave Theory and Techniques, IEEE Transactions on*, vol. 48, no. 11, pp. 2003 – 2013, nov 2000.

[88] J. A. Stratton, *Electromagnetic Theory*. New York: McGraw-Hill, 1941.

[89] A. Boriskin and A. Nosich, “Whispering-gallery and luneburg-lens effects in a beam-fed circularly layered dielectric cylinder,” *IEEE Transactions on Antennas and Propagation*, vol. 50, no. 9, pp. 1245 – 1249, sep 2002.

[90] A. Lakhtakia, M. Iskander, C. Durney, and H. Massoudi, “Near-field absorption in prolate spheroidal models of humans exposed to a small loop antenna of arbitrary orientation,” *Microwave Theory and Techniques, IEEE Transactions on*, vol. 29, no. 6, pp. 588 – 594, jun 1981.

[91] W.-T. Chen and H.-R. Chuang, “Numerical computation of the EM coupling between a circular loop antenna and a full-scale human-body model,” *Microwave Theory and Techniques, IEEE Transactions on*, vol. 46, no. 10, pp. 1516 –1520, oct 1998.

[92] T.-K. Wu, “Electromagnetic fields and power deposition in body-of-revolution models of man,” *Microwave Theory and Techniques, IEEE Transactions on*, vol. 27, no. 3, pp. 279 – 283, mar 1979.

[93] R. F. Harrington, “Matrix methods for field problems,” *Proceedings of the IEEE*, vol. 55, no. 2, pp. 136–149, feb. 1967.

[94] A. Sani, Y. Zhao, Y. Hao, A. Alomainy, and C. Parini, “An efficient FDTD algorithm based on the equivalence principle for analyzing on-body antenna performance,” *IEEE Transactions on Antennas and Propagation*, vol. 57, no. 4, pp. 1006 – 1014, apr 2009.

[95] P. Hall, Y. Hao, Y. Nechayev, A. Alomalny, C. Constantinou, C. Parini, M. Kamarudin, T. Salim, D. Hee, R. Dubrovka, A. Owadally, W. Song, A. Serra, P. Nepa, M. Gallo, and M. Bozzetti, "Antennas and propagation for on-body communication systems," *Antennas and Propagation Magazine, IEEE*, vol. 49, no. 3, pp. 41 –58, june 2007.

[96] P. S. Hall, "Antennas and propagation for body centric communications," in *Proceedings of the IET Seminar on Antennas and propagation for body-centric wireless communicatinos*, London, UK, April 2007, pp. 1–4.

[97] Z. Hu, M. Gallo, Q. Bai, Y. Nechayev, P. Hall, and M. Bozzettit, "Measurements and simulations for on-body antenna design and propagation studies," in *Antennas and Propagation, 2007. EuCAP 2007. The Second European Conference on*, nov. 2007, pp. 1 –7.

[98] B. Sanz-Izquierdo, F. Huang, and J. Batchelor, "Covert dual-band wearable button antenna," *Electronics Letters*, vol. 42, no. 12, pp. 668 – 670, june 2006.

[99] L. Aberbour and C. Craeye, "On the radiation resistance of planar monopole antennas," *IEEE Transactions on Antennas and Propagation*, vol. 57, no. 4, pp. 1035 –1042, april 2009.

[100] N. Haga, K. Saito, M. Takahashi, and K. Ito, "Characteristics of cavity slot antenna for body-area networks," *IEEE Transactions on Antennas and Propagation*, vol. 57, no. 4, pp. 837 –843, april 2009.

[101] N. Haga, M. Takahashi, K. Saito, and K. Ito, "A cavity-backed slot antenna for on-body ban devices," in *Antenna Technology: Small Antennas and Novel Metamaterials, 2008. iWAT 2008. International Workshop on*, march 2008, pp. 510 –513.

[102] W. Xia, K. Saito, M. Takahashi, and K. Ito, "Performances of an implanted cavity slot antenna embedded in the human arm," *IEEE Transactions on Antennas and Propagation*, vol. 57, no. 4, pp. 894 –899, april 2009.

[103] H. Usui, M. Takahashi, and K. Ito, "Radiation characteristics of an implanted cavity slot antenna into the human body," in *Antennas and Prop-*

agation Society International Symposium 2006, IEEE, july 2006, pp. 1095 –1098.

[104] S. van Roy, C. Oestges, F. Horlin, and P. De Doncker, "A comprehensive channel model for uwb multisensor multiantenna body area networks," *IEEE Transactions on Antennas and Propagation*, vol. 58, no. 1, pp. 163 –170, jan. 2010.

[105] G. A. Conway, W. G. Scanlon, and D. Linton, "Low-profile microstrip patch antenna for over-body surface communication at 2.45 GHz," in *International Workshop on Antenna Technology: Small and Smart Antennas Metamaterials and Applications (IWAT)*, March 2007, pp. 392–396.

[106] A. Wunsch and S.-P. Hu, "A closed-form expression for the driving-point impedance of the small inverted L antenna," *IEEE Transactions on Antennas and Propagation*, vol. 44, no. 2, pp. 236 –242, feb 1996.

[107] Z. Chen and M. Chia, "Broadband planar inverted-L antennas," *Microwaves, Antennas and Propagation, IEE Proceedings -*, vol. 148, no. 5, pp. 339 –342, oct 2001.

[108] L. Aberbour and C. Craeye, "A model for the radiation resistance of a bent plantar monopole antenna," in *Antennas and Propagation, 2006. EuCAP 2006. First European Conference on*, nov. 2006, pp. 1 –4.

[109] EMPIRE XCcel. [Online]. Available: www.empire.de

[110] J. L. B. Walker, D. P. Myer, and F. H. Raab, *Classic Works in RF Engineering*. New York: Artech House, 2006.

[111] D. Ma and W. X. Zhang, "Analytic propagation model for wireless body-area networks," *IEEE Transactions on Antennas and Propagation*, vol. 59, no. 12, pp. 4749 –4756, dec. 2011.

[112] J. Wu, S. Khamas, and G. Cook, "An efficient asymptotic extraction approach for the Green's functions of conformal antennas in multilayered cylindrical media," *IEEE Transactions on Antennas and Propagation*, vol. 58, no. 11, pp. 3737 –3742, nov. 2010.

[113] W. C. Chew, J.-M. Jin, E. Michielssen, and J. M. Song, *Fast and Efficient Algorithms in Computational Electromagnetics*. Norwood, MA: Artech House, 2001.